Wave-scattering by periodic media

Thesis by
Agustin G. Fernandez-Lado

In Partial Fulfillment of the Requirements for the
Degree of
Doctor of Philosophy

CALIFORNIA INSTITUTE OF TECHNOLOGY
Pasadena, California

2020
Defended August 23rd 2019

Agustin G. Fernandez-Lado
ORCID: 0000-0002-8141-3792

ACKNOWLEDGEMENTS

I would like to express my gratitude to my advisor for introducing me to this problem and giving me the opportunity to work at a prestigious institution like Caltech. Many of the ideas presented in this thesis emerged from interesting discussions with Carlos Perez-Arancibia. Emmanuel Garza provided the integration library which is the backbone of the three-dimensional solvers developed here. Finally, Mathieu Desbrun, Houman Owhadi and Peter Schröder provided great suggestions and a lot of encouragement in my final time at Caltech. To all of you, many thanks.

To my beautiful wife, Soledad.

“So much behind us, still far to go...”

ABSTRACT

This thesis presents a full-spectrum, well-conditioned, Green-function methodology for evaluation of scattering by general periodic structures, which remains applicable on a set of challenging singular configurations, usually called Rayleigh-Wood (RW) anomalies, where most existing methods break down. After reviewing a variety of existing fast-converging numerical procedures commonly used to compute the classical quasi-periodic Green-function, the present work explores the difficulties they present around RW-anomalies and introduces the concept of hybrid "spatial/spectral" representations. Such expressions allow both the modification of existing methods to obtain convergence at RW-anomalies as well as the application of a slight generalization of the Woodbury-Sherman-Morrison formulae together with a limiting procedure to bypass the singularities. Although, for definiteness, the overall approach is applied to the scalar (acoustic) wave-scattering problem in the frequency domain, the approach can be extended in a straightforward manner to the harmonic Maxwell's and elasticity equations. Ultimately, the thorough understanding of RW-anomalies this thesis provides yields fast and highly-accurate solvers, which are demonstrated with a variety of simulations of wave-scattering phenomena by arrays of particles, crossed impenetrable and penetrable diffraction gratings, and other related structures. In particular, the methods developed in this thesis can be used to "upgrade" classical approaches, resulting in algorithms that are applicable throughout the spectrum, and it provides new methods for cases where previous approaches are either costly or fail altogether. In particular, it is suggested that the proposed shifted Green function approach may provide the only viable alternative for treatment of three-dimensional high-frequency configurations. A variety of computational examples are presented which demonstrate the flexibility of the overall approach, including, in particular, a problem of diffraction by a double-helix structure, for which numerical simulations did not previously exist, and for which the scattering pattern presented in this thesis closely resembles those obtained in crystallography experiments for DNA molecules.

PUBLISHED CONTENT AND CONTRIBUTIONS

[BF17] Oscar P Bruno and Agustin G Fernandez-Lado. “Rapidly convergent quasi-periodic Green functions for scattering by arrays of cylinders—including Wood anomalies”. In: *Proc. R. Soc. A* 473.2199 (2017), p. 20160802. DOI: 10.1098/rspa.2016.0802. URL: https://doi.org/10.1098/rspa.2016.0802.

A.G.F.L. participated in the conception of the project, solved and analyzed equations, developed numerical software, prepared data, and helped write the manuscript.

TABLE OF CONTENTS

LIST OF ILLUSTRATIONS

Number *Page*

LIST OF TABLES

Chapter 1

INTRODUCTION

The study of waves and wave-scattering phenomena impacts upon many fields in the physical sciences and dates back to the seminal work of many illustrious scientists, founders of modern science. The present state of technology in our era was enabled mostly through the utilization of different manifestations of waves, most notably electromagnetic waves to transmit information throughout the globe and space, and elementary particles in their quantum-mechanical wave-like interpretation, like the electron, to process data in modern computers. An understanding of wave phenomena will continue to play critical roles in years to come, in promising fields of science and technology such as photonics and quantum computing, among many others.

With the widespread accessibility of high-performance computational resources in recent decades, computer simulations have become an essential tool in wave simulation, complementing both theory and experiment. In this context, the goal of this thesis is to introduce fast numerical methods to simulate certain wave-phenomena in a regime which has remained challenging in the field of applied and computational mathematics; one where the propagation domain presents an invariance by a certain set of discrete translations, i.e., it has a periodic structure.

The remainder of this introductory chapter summarizes the early history of the field of wave-scattering, with an emphasis in periodic problems, as well as the state of the art in this area. Additionally, some notation is introduced and the mathematical problem underlying this thesis is stated.

1.1 Early history

The pioneering experiments of Francesco Maria Grimaldi [Gri65], Robert Boyle [BJ38] and Robert Hooke [Hoo65] provided support to the first scientific explanations of the oscillatory nature of light. This important work was greatly advanced by Christian Huygens [Huy90], who introduced the famous principle which states that, "Every point of the ‘aether’ upon which the luminous disturbance falls may be regarded as the center of a new disturbance propagated in the form of spherical waves; these secondary waves combine in such a manner that their envelope determines the wave-

front at any later time." Using this premise Huygens obtained theoretical derivations of the experimental laws of reflection and refraction (commonly known as Snell's or Snell-Descartes' laws).

The authoritative figure of Isaac Newton, who advocated instead the corpuscular theory of light [New72], caused the wave-theory to be ignored for over a century. Eventually, however, a rapid sequence of decisive developments in the early XIX century led to the widespread acceptance of the wave theory. In 1801, Thomas Young enunciated the principle of interference and explained the colors of thin films [You02], but as this analysis was largely qualitative, these ideas did not gain general recognition. Supporters of the corpuscular theory, like Simon de Laplace and Jean-Baptiste Biot, proposed the subject of diffraction for the prize question set by the Paris Academy for 1818 with the belief that the corpuscular theory would result triumphant. However, even with a large opposition, the prize was awarded to Augustine Jean Fresnel, whose treatment was based on Huygens' and Young's wave theory; in this work he could not only explain the "rectilinear propagation" of light (the main objection to the theory made by Newton) but also calculated diffraction effects caused by edges, apertures and screens [Fre68]. Based on Fresnel's ideas, Siméon Denis Poisson predicted the appearance of a bright spot in the center of the shadow produced by the illumination of a small disc, a result which he considered ridiculous and would disprove the wave-theory; however, this prediction was experimentally verified by Dominique François Arago [Ara19], who was appointed by the Paris Academy to report on Fresnel's investigations. The dispute between the two theories was settled in great part (at least for the following sixty years) through a set of experiments performed by Foucault, Fizeau and Breguet [Fou50; FB50] in 1850. The measurements showed that light propagates slower in media denser than air disproving the corpuscular theory (which predicted the opposite) and giving support to the wave-theory (which predicted correctly this behavior). In the following decades, a rigorous mathematical foundation for the wave theory was settled by Hermann von Helmholtz, George Airy [Air38], George Green [Gre38], Franz Neumann [Neu38], George Stokes [Sto49], Gustav Kirchhoff [Kir83] and, later, Lord Rayleigh [Ray07] and Arnold Sommerfeld [Som09].

Concurrently to the vast expansion of the field of optics, several discoveries in electricity and magnetism took place in the 19th century, most famously by Michael Faraday [Far39] and André-Marie Ampère [Amp26]. The culmination of all these advances took place in the first unification of the laws of physics with the work

of James Clark Maxwell [Max81]. Measurements by Rudolph Kohlrausch and Wilhelm Weber [KW93] showed that electromagnetic waves propagate at the same speed as light. These observations led Maxwell to conjecture that light has its origin in perturbations of the electromagnetic field, a prediction that was later verified through experimentation in 1888 by Heinrich Hertz [Her88]. Posterior work by Marconi [Mar09] and Braun [Bra09] initiated the era of wireless communications, showing the enormous practical consequences of Maxwell's electromagnetic theory.

Diffraction gratings

A diffraction grating can be defined as any repetitive array of diffracting elements, either apertures or obstacles, which have the effect of producing periodic changes in the phase or amplitude of an incoming oscillatory radiation. The discovery of the working principle and first prototypes of diffraction gratings are attributed to David Rittenhouse in 1785 [Rit86] though these investigations attracted little attention at the time. During the following decades, Joseph von Fraunhofer would rediscover independently this principle and perfect the manufacturing process [Fra24] of this and many other devices, setting his home Bavaria as the European epicenter of the optical industry at the time. Subsequent developments in the following hundred years, most famously by Henry A. Rowland, Albert A. Michelson and Robert W. Wood [Har49], improved the fabrication techniques yielding devices of very high-quality at the beginning of the XX century.

Many disciplines in the sciences have benefited from studies of diffraction patterns produced by periodic structures. The first spectrographs used multiple diffraction gratings (as the one introduced by Rittenhouse and Fraunhoffer) to split the incoming radiation of interest into its many spectrum components; this analysis enabled a large number of applications ranging from the determination of the chemical structure of distant stars to the study of the detailed structure of the hydrogen atom. X-ray crystallography was also greatly influenced by the study of wave-phenomena in periodic media as, in this case, the grating structure is provided by atoms in a crystal which are typically separated by distances of the order of an Ångström—a magnitude comparable to the wavelength of X-rays. Max von Laue theorized that if a beam of X-rays illuminates a crystal then a diffraction pattern would be produced and, therefore, certain properties of the crystal could be deduced. The first observations of this phenomena were made by Walter Friedrich, Paul Knipping and von Laue [FKL13], granting the latter the 1914 Physics Nobel Prize.

One of the first applications of modern quantum mechanics (as established in the Schrödinger formalism) was suggested by Felix Bloch to study the conduction of electrons in crystalline solids through the introduction of the important concept of the electronic bandgap [Blo29]. According to this theory, materials present two types of energetic states that an electron can assume: the valence band, in which an electron is tied to the nucleus of an atom, and the conduction band, in which the electrons have enough energy to move freely in the material. The bandgap can be roughly described as the distance between the largest energy state of the valence band and the lowest energy state of the conduction band; if there is no gap then no energy is necessary to excite an electron to move (and therefore conduct electricity) while if the gap is large then the material acts as an insulator (a very large amount of energy would be necessary for an electron to leave its orbit). Semiconductors are then the materials which require a small additional amount of input energy to be able to control the state of an electron at will. The existence of such a gap is a consequence of the periodic structure of the electric potential produced by the atoms in the crystal and can be regarded as one of the most important implications of quantum-mechanics (and therefore, of wave-phenomena) in our present highly-technological society.

The first rigorous mathematical treatment of scattering by periodic media is attributed to Lord Rayleigh who, in his famous *Theory of sound* [Ray96] considered the scalar problem of scattering by a periodic surface of the form $(x, f(x))$, $x \in \mathbb{R}$, where f is an L-periodic smooth function. Thus, for an incoming plane wave with wavenumber k which illuminates the grating under an angle of incidence θ, Rayleigh modeled the scattering process by means of the scalar problem

$$\begin{cases} \Delta u(x,y) + k^2 u(x,y) = 0, & y > f(x) \\ u = -\mathrm{e}^{\mathrm{i}k\sin(\theta)x - \mathrm{i}k\cos(\theta)y}, & y = f(x) \\ u \text{ propagates outward.} \end{cases} \tag{1.1}$$

With a simple separation of variables argument he showed that in the region $y > \max\{f(x)\}$ (above the *grooves*) the solution of (1.1) can be expressed in the simple form

$$u(x,y) = \sum_{n\in\mathbb{Z}} A_n e^{i\alpha_n x + i\beta_n y}, \tag{1.2}$$

where

$$\alpha_n = k\sin(\theta) + \frac{2\pi}{L}n, \quad \beta_n = \sqrt{k^2 - \alpha_n^2},\ \mathrm{Im}(\beta_n) \geq 0. \tag{1.3}$$

Equation (1.2) reveals the nature of the reflected field produced by a periodic structure of an incoming plane-wave: it is the superposition of infinitely many waves of which finitely many are non-decaying *propagating* modes (whenever β_n is a real number) while the remaining decay exponentially fast as $y \to +\infty$ (are evanescent) whenever β_n is a purely complex number. Expressions like (1.2), usually called *Rayleigh expansions*, appear throughout this work, and play major roles in the methodology proposed. An interesting situation arises whenever a scattering configuration (in this case k, θ and L) is selected so that there exists at least one integer n which satisfies $\beta_n = 0$; in that case, one of the modes in (1.2) travels parallel to the periodic surface $y = f(x)$. Moreover, as one (or more) of these three parameters varies around this singular configuration we see that the corresponding mode $e^{i\alpha_n x + i\beta_n y}$ changes abruptly in its nature, from being propagating to evanescent (or vice versa). Lord Rayleigh attributed to this pass-off configurations [Ray93] a set of observations carried out previously in 1902 by Robert W. Wood, who had noted that [Woo02]

> "[...] On mounting the grating on the table of a spectrometer I was astounded to find that under certain conditions the drop from maximum illumination to minimum, a drop certainly of from 10 to 1, occurred within a range of wave-lengths not greater than the distance between the sodium lines (...) A change of wavelength of 1/1000 [of a micron] is then sufficient to cause the illumination in the spectrum to change from a maximum to a minimum."

These particular configurations, discussed by Wood and Rayleigh, and their extensions to other setups, which are the central topic around which this thesis revolves, have received in the computational physics literature the name *Wood anomalies*. It has been pointed out recently by David Maystre [May12], based on work in the 1940s by Fano [Fan41], that the original experiments of Wood cannot be explained solely in terms of Rayleigh expansions and suggests a distinction for the anomalies observed in the scattering patterns of diffraction gratings and a renaming for what has been called up to this date *Wood anomalies*. Thus, in this thesis we will refer to the singular pass-off configurations as Rayleigh-Wood (RW) anomalies.

Recent progress and current challenges

Wave-scattering by periodic media, including RW anomalous configurations, continue to attract the attention of many researchers in the fields of optics [Dar+18;

Kim+15; Mar+16; MS16; Mau+14; May12; NPT18; Sav+13; TJE19] and computational electromagnetism [BD14; BM18a; BF17; Bru+16; Bru+17; LB16; Cho18; LKB15; Per+18; NPT18; Den+17a]. Classical boundary integral equations methods [PC90; Ste+06; Vey+91] have relied on the quasi-periodic Green function (denoted throughout this work as G_κ^q), which is defined in terms of a slowly converging infinite series (equation (2.1)). In order to obtain efficient scattering solvers, several alternative representations, with better convergence properties, have been introduced for the evaluation of G_κ^q. These employ either Kummer or Shanks transformations, lattice sums, Laplace-type integrals and, most notably, the Ewald summation method [Lin10; Lin98]. In the last decade, the novel windowed-Green function (WGF) method was introduced and applied to the periodic problem [BD14; Bru+16; Mon08] obtaining super-algebraic convergent solvers away from RW-anomalies. With the exception of the Ewald method, the convergence properties of these methodologies deteriorate significantly around RW-anomalies which are pervasive in the most challenging three dimensional case (see Figure 2.1).

A subsequent development to the WGF methodology introduced a novel quasi-periodic "shifted" Green function [BD14; Bru+17] which, like the "classical" (unshifted) quasi-periodic Green function, is also defined in terms of an infinite series but whose general term has a faster -algebraic- decay rate obtained with the introduction of additional spatial poles. This improvement yields a Green-function which, unlike G_κ^q, is well-defined at RW-anomalies. Since it introduces new spatial singularities, this technique was first applied to problems where the domain was a half-space whose boundary could be parametrized by the graph of a periodic function. The contribution [BF17] introduced a slightly different use of the shifted Green function from its original inception to allow for its application to more general domains.

In a nutshell, numerical methods which discretize boundary integral equations basically operate by forming a finite linear system of equations and solving it by either direct inversion or an iterative algorithm. As RW-anomalies are approached in the periodic problem, two sources of pollution in the numerical error of the solution emerge: the most drastic of them corresponds to (1) Poor approximations of G_κ^q, while a more subtle one is related to (2) Ill-conditioning in the system of equations. Whereas both the WGF and Laplace-type integral methods suffer from the first problem (Figures 1.1 and 1.2), the shifted Green function and Ewald methods do not (see Figure 5.3). In this context, the main contributions of this thesis include

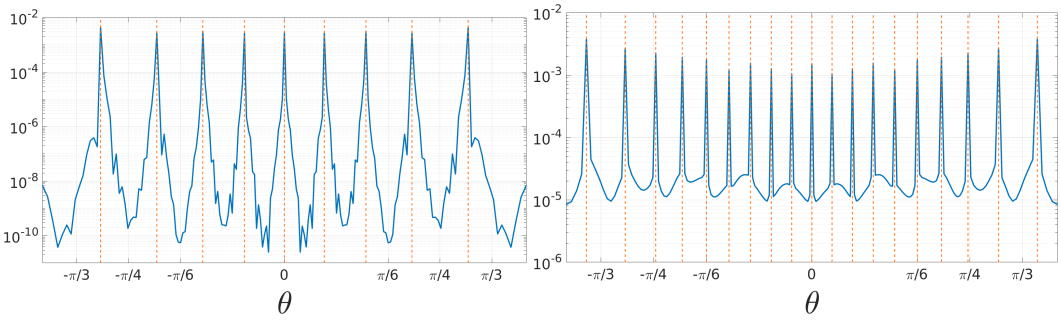

Figure 1.1: Error in a WGF simulation of wave-scattering of an incoming plane wave with incidence angle θ by a two-dimensional periodic array of circular cylinders of period 5λ (left, depicted in Figure 5.1) and 10λ (right). Here and throughout this thesis λ denotes the radiation wavelength. The vertical lines indicate the incidence angles which give rise to RW-anomalies for this configuration (see equation (2.6)). Errors were estimated via the energy balance criterion (Appendix A). Clearly, uncontrolled errors arise at and around RW anomalies for the non-RW capable version of the WGF approach.

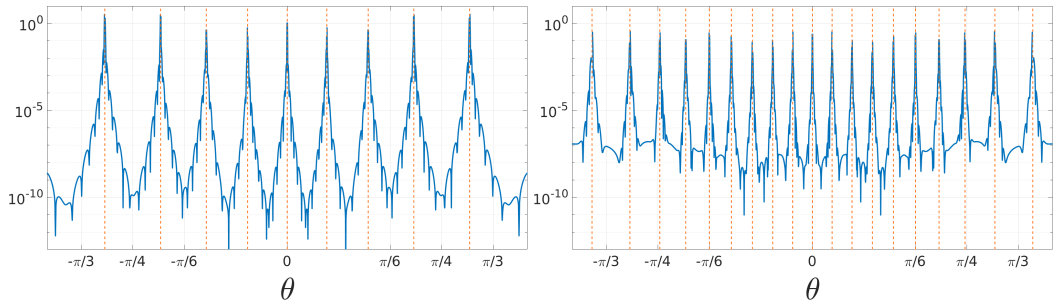

Figure 1.2: Same experiment as in Figure 1.1 but the simulation is obtained by means of the Laplace-type integral method (Section 2.1). Clearly, uncontrolled errors arise at and around RW anomalies for the non-RW capable version of the Laplace-type integral approach.

(a) a theoretical understanding of these difficulties, and (b) computational algorithms which, exploiting the new theory, enable solution of previously intractable problems.

Through the introduction of the concept of hybrid "spatial/spectral" representations, this work shows that if a representation of G_κ^q is used which displays explicitly terms that cause the divergence of G_κ^q as RW anomalies are approached, then high-accuracies can be obtained in the evaluation of G_κ^q in very close proximity (to machine precision) of the singular configuration—thus addressing the evaluation difficulty mentioned in point (1) above. Use of such representations, in turn, provides an insight into the ill-conditioning of the resulting linear systems around

RW-anomalies mentioned in point (2) above, and they allow us to introduce a regularization technique, which we refer to as the "Woodbury-Sherman-Morrison (WSM) methodology", that resolves the difficulty and can be used to produce solutions at RW-anomalies using quasi-periodic Green function methods. These two elements are the building blocks of this thesis which, ultimately, strives to obtain fast, robust and highly-accurate solvers to simulate wave-scattering phenomena by periodic media in general geometries irrespectively of the occurrence of RW-anomalies.

A major difficulty still remains in the high-frequency/large-periods regime since, as briefly described in Chapter 3, classical methods break down due to instabilities and cancellation errors (see, also, [KNR11; KR09]). As explored in that chapter and demonstrated in a two-dimensional case in [BM18a], the shifted Green function, in contrast, does not present these difficulties, providing a promising direction for this challenging case. However, since additional acceleration techniques are required to treat such large configurations (in view of the large number of discretization points they require), the resolution of this challenge is out of the scope of this thesis and is left for future work.

The following section presents notations and establishes the PDE problem this thesis intends to solve. Chapter 2 then introduces the most important mathematical object of this dissertation, the classical quasi-periodic Green function, and gives several alternative representations for its evaluation. The details of the numerical implementations needed in the solvers used in this thesis are described in Chapter 3 while the framework put forth in this work is explained in Chapter 4. Finally, Chapter 5 contains a variety of numerical results demonstrating the applicability of the overall methodology.

1.2 Preliminaries and notation

Periodic structures

This thesis considers frequency-domain problems of wave scattering by periodic penetrable and impenetrable diffraction gratings in two- and three-dimensional space, including arrays of particles, layers of corrugated surfaces and combinations thereof. In all cases the propagation domain $\Omega \subseteq \mathbb{R}^d$ ($d = 2, 3$) is infinite and translationally invariant with respect to a certain periodicity lattice Λ. In detail, calling

$$\Lambda = \left\{ \sum_{i=1}^{d_\Lambda} m_i \boldsymbol{v_i} : m_i \in \mathbb{Z} \right\}, \tag{1.4}$$

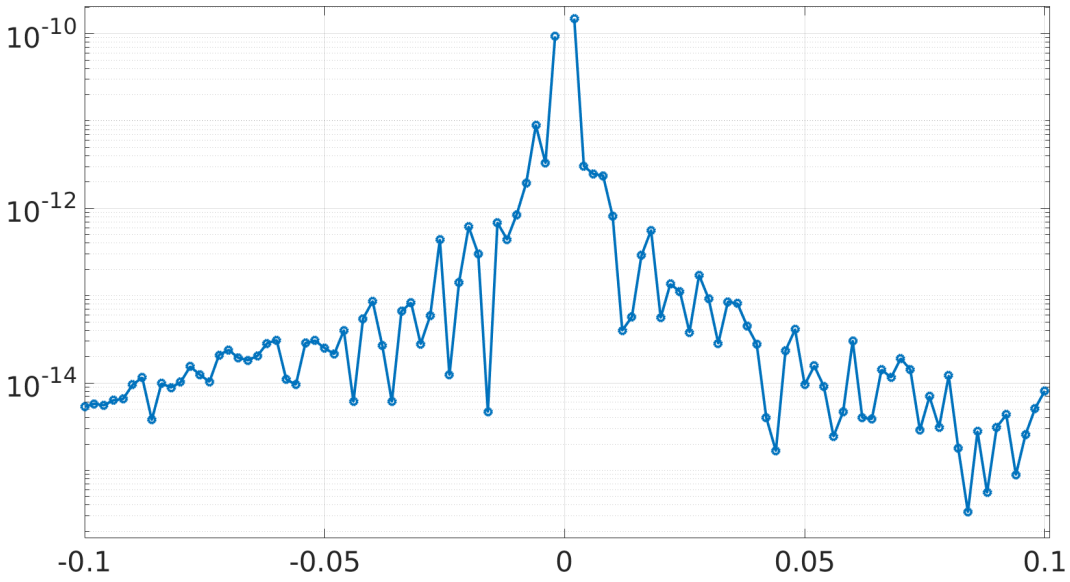

Figure 1.3: Same experiment as Figure 1.1 but the simulation is obtained by means of the Ewald method (Section 2.2). We restrict the attention to the case where the period equals 5λ and the plane wave impinges on the structure with angles very close to normal incidence (the central anomalous configuration in Figures 1.1 and 1.2). In these numerical examples, the angle θ equals δ^5, sampling incidence directions which differ from normal incidence in angles of the order of 10^{-5} to 10^{-14}. The errors is unbounded around $\theta = \delta^5 = 0$, at which point the method fails.

a given d_Λ-dimensional periodicity lattice ($1 \leq d_\Lambda < d$), Ω satisfies the translation-invariance property

$$\Omega + \boldsymbol{R} = \Omega \quad \text{for all} \quad \boldsymbol{R} \in \Lambda. \tag{1.5}$$

The directions $\boldsymbol{v_i}$, $i = 1, \ldots, d_\Lambda$ in (1.4) are commonly called the primitive (or periodicity) vectors of the lattice. Without loss of generality, throughout this work it is assumed that $\boldsymbol{v_1}$ is parallel to the x_1-axis, and that the lattice is contained in the subspace generated by the vectors $x_1, \ldots, x_{d_\Lambda}$ (so that the periodicity lattice is contained in the line $\{(x_1, 0)\}$ in two dimensions, and either in the line $\{(x_1, 0, 0)\}$ or the plane $\{(x_1, x_2, 0)\}$ in three dimensions).

Remark 1. *In what follows, for $\boldsymbol{x} \in \mathbb{R}^d$ we let $\boldsymbol{x}^\perp$ denote the projection of $\boldsymbol{x}$ into the subspace orthogonal to the set Λ, and we call $\boldsymbol{x}^\parallel = \boldsymbol{x} - \boldsymbol{x}^\perp$. Thus, for $\boldsymbol{x} = (x_1, x_2, x_3)$ we have e.g. $\boldsymbol{x}^\perp = (0, x_2, x_3)$ for $d = 3$ and $d_\lambda = 1$, while $\boldsymbol{x}^\perp = (0, 0, x_3)$ for $d = 3$ and $d_\lambda = 2$.*

Clearly, the projection $\boldsymbol{x}^{\parallel} = \boldsymbol{x} - \boldsymbol{x}^{\perp}$ *can be expressed in the form*

$$\boldsymbol{x}^{\parallel} = \sum_{i=1}^{d_\Lambda} a_i \boldsymbol{v_i}, \quad a_i \in \mathbb{R}. \tag{1.6}$$

and so, letting $\boldsymbol{x}^{\sharp} = \sum_{i=1}^{d_\Lambda} b_i \boldsymbol{v_i} + \boldsymbol{x}^{\perp}$ *where the coefficients* $b_i = a_i - \lfloor a_i \rfloor$ *belong to the interval* $[0, 1)$*, any point* $\boldsymbol{x} \in \mathbb{R}^d$ *is a translation of* $\boldsymbol{x}^{\sharp}$ *by the lattice* Λ*. In what follows, for any set* $S \subseteq \mathbb{R}^d$ *we will let* $S^{\sharp}$ *denote the set*

$$S^{\sharp} = \left\{ \boldsymbol{x}^{\sharp} : \boldsymbol{x} \in S \right\}. \tag{1.7}$$

We say that a set $S \subseteq \mathbb{R}^d$ *is transversely bounded (resp. transversely unbounded) if the corresponding set* $S^{\sharp}$ *is bounded (resp. unbounded).*

Scattering problems

For a given incident field u^{inc}, we seek to evaluate the associated acoustic fields under sound-soft and sound-hard conditions. In the sound-soft case, for example, the acoustic field u is a weak solution of the scalar Helmholtz equation

$$\Delta u + k^2 n^2(\boldsymbol{x}) u = 0 \quad \text{in } \Omega, \tag{1.8}$$

with wavenumber $k > 0$, while in the sound-hard case, u satisfies

$$\nabla \cdot \left(\frac{1}{n^2(\boldsymbol{x})} \nabla u \right) + k^2 u = 0 \quad \text{in } \Omega. \tag{1.9}$$

Here the refractive-index function $n(\boldsymbol{x}) > 0$ is a Λ-periodic function of $\boldsymbol{x}$ throughout Ω, that is $n(\boldsymbol{x} + \boldsymbol{R}) = n(\boldsymbol{x})$ for all $\boldsymbol{x} \in \Omega$ and all $\boldsymbol{R} \in \Lambda$, and locally constant, with a finite set of values. The domain Ω is decomposed as a finite union

$$\Omega = \bigcup_{j=0}^{r+1} \Omega_j, \tag{1.10}$$

of the sets $\Omega_0, \Omega_1, \ldots, \Omega_r, \Omega_{r+1}$, on each one of which the refractive index is constant (see Figure 1.4). In detail, throughout this thesis it is assumed that

1. All except at most two of the sets Ω_j are transversely bounded. The set Ω_0 is required to be transversely unbounded, and Ω_{r+1} is either transversely unbounded or empty.

2. For $d_\lambda = d - 1$, Ω_0 contains a set of the form $\{x_d > M\}$ for some $M > 0$. For $d = 3$ and $d_\lambda = 1$, Ω_0 contains a set of the form $\{|\boldsymbol{x}^{\perp}| > M\}$. If $\Omega_{r+1} \neq \emptyset$ (which is not possible for $d = 3$ and $d_\lambda = 1$), then Ω_{r+1} contains the set $\{x_d < -M\}$ for some $M > 0$.

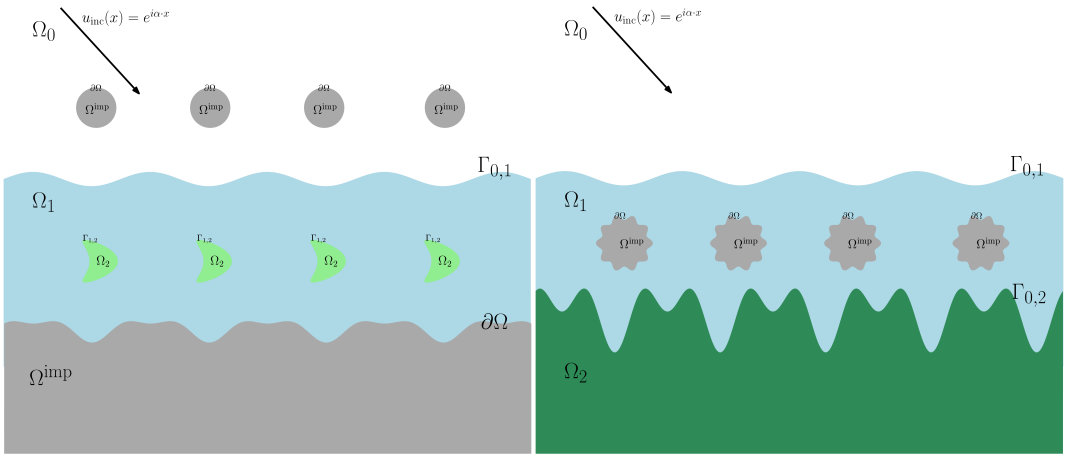

Figure 1.4: Incoming plane waves impinging on two periodic structures of the types considered in this thesis. In both cases the refractive index assumes three different values and the dark-gray regions indicate the domain Ω^{imp} which waves cannot penetrate. The left figure includes only one transversally unbounded propagation region (Ω_0), while the right figure contains two transversally unbounded regions (Ω_0 and Ω_2). Thus, these examples demonstrate cases where Ω_{r+1} is empty and non-empty, respectively.

3. There are at most two and at least one transversely-unbounded constant-refractivity sets. One of these sets, denoted by Ω_0, is assumed to contain the incident field. The set denoted by Ω_{r+1} ($r \geq 0$), on the other hand, equals either the second transversely-unbounded constant-refractivity set or, if Ω_0 is the only such set, then $\Omega_{r+1} = \emptyset$.

Thus, equations (1.8) and (1.9) become

$$\Delta u + k^2 n_j^2 u = 0 \quad \text{in } \Omega_j \quad \text{for } 0 \leq j \leq r+1. \tag{1.11}$$

Note that Ω may or may not equal the totality of $\mathbb{R}^d$. In the case $\Omega = \mathbb{R}^d$ each portion of space is occupied by a penetrable material. In the case $\Omega \neq \mathbb{R}^d$, in turn, the complement Ω^{imp} of the closure of Ω,

$$\Omega^{\text{imp}} = \mathbb{R}^d \setminus \Omega = \mathbb{R}^d \setminus \left(\bigcup_{j=0}^{r+1} \Omega_j \right)$$

is assumed to be occupied by either sound-soft or sound-hard impenetrable media, or a combination of the two. Thus Ω^{imp} is given by the union

$$\Omega^{\text{imp}} = \Omega_D^{\text{imp}} \cup \Omega_N^{\text{imp}}$$

of the disjoint sets Ω_D^{imp} (with boundary Γ_D^{imp}) and Ω_N^{imp} (with boundary Γ_N^{imp}) occupied by sound-soft and sound-hard materials, respectively:

$$\Gamma^{\mathrm{imp}} = \Gamma_D^{\mathrm{imp}} \cup \Gamma_N^{\mathrm{imp}}.$$

For simplicity, throughout this contribution it is assumed that Γ_D^{imp} and Γ_N^{imp} are disjoint, but the general non-disjoint case can also be considered within this context (cf. [A+17]).

We assume that the structure is illuminated by a plane wave u^{inc} defined in the transversely-unbounded domain Ω_0, where

$$u^{\mathrm{inc}}(\boldsymbol{x}) = \mathrm{e}^{\mathrm{i}\boldsymbol{\alpha}\cdot\boldsymbol{x} - \mathrm{i}\boldsymbol{\beta}\cdot\boldsymbol{x}}, \quad \boldsymbol{x} \in \Omega_0. \tag{1.12}$$

Here $\boldsymbol{\alpha}$ and $\boldsymbol{\beta}$ are parallel and perpendicular to the lattice Λ, respectively, and verify $|\boldsymbol{\alpha}|^2 + |\boldsymbol{\beta}|^2 = n_0^2 k^2$; the scattered field u^{s} is thus defined by the relations

$$u^{\mathrm{s}}(\boldsymbol{x}) = \begin{cases} u(\boldsymbol{x}) - u^{\mathrm{inc}}(\boldsymbol{x}), & \boldsymbol{x} \in \Omega_0 \\ u(\boldsymbol{x}), & \boldsymbol{x} \in \Omega_j,\ j \geq 1 \end{cases} \tag{1.13}$$

and we clearly have

$$\Delta u^{\mathrm{s}} + k^2 n_j^2 u^{\mathrm{s}} = 0 \quad \text{in } \Omega_j \quad \text{for } 0 \leq j \leq r+1. \tag{1.14}$$

For each pair j, ℓ of indices, $j < \ell$, we denote by $\Gamma_{j\ell}$ the boundary between Ω_j and Ω_ℓ, and we let $\Gamma_{j\ell} = \emptyset$ for $j \geq \ell$. For $\boldsymbol{x} \in \Gamma_{j\ell}$ ($j < \ell$), $\nu = \nu(\boldsymbol{x})$ denotes the unit normal vector to $\Gamma_{j\ell}$ which points into the "plus side" Ω_j of $\Gamma_{j\ell}$. (Note that, even for $j < \ell$, $\Gamma_{j\ell}$ is empty whenever Ω_j and Ω_ℓ do not share a common boundary.) For $\boldsymbol{x} \in \Gamma^{\mathrm{imp}}$, in turn, $\nu = \nu(\boldsymbol{x})$ denotes the normal to Γ^{imp} which points into the interior of Ω (or into the exterior of Ω^{imp}). Additionally we define the set of all points at transmission boundaries (resp. all points at impenetrable boundaries) by $\Gamma^{\mathrm{trans}} = \bigcup_{j<\ell} \Gamma_{j\ell}$ (resp. $\Gamma^{\mathrm{imp}} = \partial\Omega$), and we call $\Gamma = \Gamma^{\mathrm{trans}} \cup \Gamma^{\mathrm{imp}}$ the set of all points at interface boundaries. The impenetrable boundary Γ^{imp} may additionally be decomposed into its sound-hard and sound-soft portions: $\Gamma^{\mathrm{imp}} = \Gamma_s^{\mathrm{imp}} \cup \Gamma_h^{\mathrm{imp}}$. For $\boldsymbol{x} \in \Gamma$ we define the boundary values of a function u and its normal derivative at $\boldsymbol{x}$ from the + and − sides of an interface by

$$u_\pm(\boldsymbol{x}) = \lim_{\delta \to 0^+} \big[u(\boldsymbol{x} \pm \delta\nu(\boldsymbol{x}))\big] \quad \text{and} \quad \frac{\partial u_\pm}{\partial \nu}(\boldsymbol{x}) = \lim_{\delta \to 0^+} \big[\nabla u(\boldsymbol{x} \pm \delta\nu(\boldsymbol{x})) \cdot \nu(\boldsymbol{x})\big]. \tag{1.15}$$

The PDE problem under consideration is fully determined by equation (1.11) together with the boundary conditions

$$u = 0 \quad \text{for} \quad \boldsymbol{x} \in \Gamma_s^{\text{imp}} \quad \text{and} \quad \frac{\partial u}{\partial \nu} = 0 \quad \text{for} \quad \boldsymbol{x} \in \Gamma_h^{\text{imp}}, \tag{1.16}$$

together with the transmission conditions

$$u_+ - u_- = 0 \quad \text{and} \quad \frac{\partial u_+}{\partial \nu} - \frac{1}{C_{j\ell}^2}\frac{\partial u_-}{\partial \nu} = 0, \quad \boldsymbol{x} \in \Gamma_{j\ell} \tag{1.17}$$

and the conditions of radiation at infinity. (The latter concept, together with the related reciprocal lattice Λ^* and the associated Rayleigh expansion, are described in what follows.) In these equations we have set

$$C_{j\ell} = \begin{cases} 1 & \text{in the sound-soft case, and} \\ \frac{n_\ell}{n_j} & \text{in the sound-hard case.} \end{cases}$$

The reciprocal lattice

$$\Lambda^* = \left\{ \sum_{j=1}^{d_\Lambda} m_j \boldsymbol{w_j} : m_j \in \mathbb{Z} \right\} \tag{1.18}$$

plays an important role in the context of periodic lattice sums we consider—which can be represented either as series with support over the lattice Λ or, on account of the Poisson summation formula [Sim15], over the reciprocal lattice Λ^*. The reciprocal basis vectors $\boldsymbol{w_j}$, $j = 1, \ldots, d_\Lambda$, are defined as the vectors which span the same vector subspace as the set $\{\boldsymbol{v_i} : i = 1, \ldots, d_\Lambda\}$, and which verify the relations

$$\boldsymbol{v_i} \cdot \boldsymbol{w_j} = 2\pi\delta_i^j. \tag{1.19}$$

Following [Lin10], using the multi-index $\boldsymbol{m} = (m_1, \ldots, m_{d_\Lambda}) \in \mathbb{Z}^{d_\Lambda}$, elements of Λ and Λ^* will be denoted by

$$\boldsymbol{R_m} = \sum_{i=1}^{d_\Lambda} m_i \boldsymbol{v_i} \quad \text{and} \quad \boldsymbol{K_m} = \sum_{i=1}^{d_\Lambda} m_i \boldsymbol{w_i}, \tag{1.20}$$

respectively.

We say that a function u defined on Ω is $\boldsymbol{\alpha}$-quasi-periodic with respect to Λ provided

$$u(\boldsymbol{x} + \boldsymbol{R_m}) = \mathrm{e}^{\mathrm{i}\alpha\cdot\boldsymbol{R_m}} u(\boldsymbol{x}) \quad \text{for all} \quad \boldsymbol{m} \in \mathbb{Z}^{d_\Lambda}. \tag{1.21}$$

Clearly, the incident field (1.12) is an $\boldsymbol{\alpha}$-quasi-periodic function and, as is well known [PC90], so is the scattered field u^s. On any set of the form

$$V_{m_1}^{m_2} = \{\boldsymbol{x} \in \mathbb{R}^d : m_1 < |\boldsymbol{x}^\perp| < m_2\} \tag{1.22}$$

that satisfies

$$V_{m_1}^{m_2} \subseteq \Omega_j \quad \text{for some} \quad j, \tag{1.23}$$

the solution u^{s} in (1.14) (like any quasi-periodic solution of the Helmholtz equation) may be expressed as an $\boldsymbol{\alpha}$-quasi-periodic *Rayleigh-series* expansion of the form

$$u^{\mathrm{s}}(\boldsymbol{x}) = \sum_{\boldsymbol{m}\in\mathbb{Z}^{d_\Lambda}} A_{\boldsymbol{m}}^{+} \mathrm{e}^{\mathrm{i}\boldsymbol{\alpha}_{\boldsymbol{m}}\cdot\boldsymbol{x}+\mathrm{i}\beta_{\boldsymbol{m}}(n_j k)x_d} + A_{\boldsymbol{m}}^{-} \mathrm{e}^{\mathrm{i}\boldsymbol{\alpha}_{\boldsymbol{m}}\cdot\boldsymbol{x}-\mathrm{i}\beta_{\boldsymbol{m}}(n_j k)x_d}, \quad d_\Lambda = d-1 \tag{1.24}$$

and

$$u^{\mathrm{s}}(\boldsymbol{x}) = \sum_{\boldsymbol{m}\in\mathbb{Z}^{d_\Lambda}} \mathrm{e}^{\mathrm{i}\boldsymbol{\alpha}_{\boldsymbol{m}}\cdot\boldsymbol{x}} U_{\boldsymbol{m}}(x_2, x_3) \quad d_\Lambda = 1, d = 3, \tag{1.25}$$

where $U_{\boldsymbol{m}}(x_2, x_3)$ satisfies the Helmholtz equation with wavenumber $\beta_{\boldsymbol{m}}(n_j k)$ in two-dimensional space

$$\Delta U_{\boldsymbol{m}}(x_2, x_3) + \beta_{\boldsymbol{m}}(n_j k)^2 U_{\boldsymbol{m}}(x_2, x_3) = 0. \tag{1.26}$$

In (1.24) and (1.25) we have set

$$\boldsymbol{\alpha}_{\boldsymbol{m}} = \boldsymbol{\alpha} + \boldsymbol{K}_{\boldsymbol{m}}, \quad \beta_{\boldsymbol{m}} = \beta_{\boldsymbol{m}}(\kappa) = \sqrt{\kappa^2 - |\boldsymbol{\alpha}_{\boldsymbol{m}}|^2} \quad \text{and} \quad \mathrm{Im}(\beta_{\boldsymbol{m}}) \geq 0. \tag{1.27}$$

Remark 2. *Throughout this work we will consider problems where the propagation domain Ω extends to infinity both along the periodic lattice direction as well as along orthogonal directions to the lattice (see points 1–3 in 1.2). Note that in the case $d_\Lambda = d-1$, the modes $\mathrm{e}^{\mathrm{i}\boldsymbol{\alpha}_{\boldsymbol{m}}\cdot\boldsymbol{x}+\mathrm{i}\beta_{\boldsymbol{m}}x_d}$ and $\mathrm{e}^{\mathrm{i}\boldsymbol{\alpha}_{\boldsymbol{m}}\cdot\boldsymbol{x}-\mathrm{i}\beta_{\boldsymbol{m}}x_d}$ represent outgoing waves in the half-spaces $x_d > M$ and $x_d < -M$ respectively. Similarly, the cylindrical waves $\mathrm{e}^{\mathrm{i}\boldsymbol{\alpha}_{\boldsymbol{m}}\cdot\boldsymbol{x}} H_0^{(1)}\left(\beta_{\boldsymbol{m}}\sqrt{x_2^2+x_3^2}\right)$ represent outgoing waves in the case $d_\Lambda = 1$, $d = 3$. A quasi-periodic solution of the Helmholtz equation* (1.11) *is called radiating if the relevant associated Rayleigh expansion, either* (1.24) *or* (1.25)*, only contains outgoing modes in any set $V_{m_1}^{m_2}$ satisfying* (1.23)*. Thus the scattered field u^{s}, which has been assumed to be radiating, i.e., it only contains outgoing modes and remains bounded as $|\boldsymbol{x}^{\perp}| \to \infty$, is given by a Rayleigh expansion of the form*

$$\begin{aligned} u^{\mathrm{s}}(\boldsymbol{x}) &= \sum_{\boldsymbol{m}\in\mathbb{Z}^{d_\Lambda}} A_{\boldsymbol{m}}^{+} \mathrm{e}^{\mathrm{i}\boldsymbol{\alpha}_{\boldsymbol{m}}\cdot\boldsymbol{x}+\mathrm{i}\beta_{\boldsymbol{m}}(n_j k)x^{\perp}}, \quad x_d > M \quad \textit{and} \\ u^{\mathrm{s}}(\boldsymbol{x}) &= \sum_{\boldsymbol{m}\in\mathbb{Z}^{d_\Lambda}} A_{\boldsymbol{m}}^{-} \mathrm{e}^{\mathrm{i}\boldsymbol{\alpha}_{\boldsymbol{m}}\cdot\boldsymbol{x}-\mathrm{i}\beta_{\boldsymbol{m}}(n_j k)x^{\perp}}, \quad x_d < -M \end{aligned} \tag{1.28}$$

if $d_\Lambda = d-1$ and

$$u^{\mathrm{s}}(\boldsymbol{x}) = \sum_{\boldsymbol{m}\in\mathbb{Z}^{d_\Lambda}} \mathrm{e}^{\mathrm{i}\boldsymbol{\alpha}_{\boldsymbol{m}}\cdot\boldsymbol{x}} U_{\boldsymbol{m}}(x_2, x_3) \tag{1.29}$$

if $d_\Lambda = 1$, $d = 3$, where $U_{\boldsymbol{m}}(x_2, x_3)$ satisfies (1.26) *and the two-dimensional Sommerfeld radiation condition [CK12, Eqn. 3.85].*

We will obtain $\boldsymbol{\alpha}$-quasi-periodic solutions of equation (1.11) by relying on integral equations and $\boldsymbol{\alpha}$-quasi-periodic Green functions. The classical $\boldsymbol{\alpha}$-quasi-periodic Green function is introduced in the following section, which additionally describes the difficulties that arise at Rayleigh-Wood anomalies. Section 4.2 then presents a new strategy leading to Green-function solutions even at and around Wood anomalies.

Chapter 2

QUASI-PERIODIC GREEN FUNCTIONS AND THEIR REPRESENTATIONS

Given $\boldsymbol{\alpha} \in \mathbb{R}^d$ and $\kappa > 0$ the quasi-periodic Green function G_κ^q is given by the conditionally-convergent sum

$$G_\kappa^q(\boldsymbol{x}) = \sum_{\boldsymbol{m}\in\mathbb{Z}^{d_\Lambda}} \mathrm{e}^{\mathrm{i}\alpha\cdot\boldsymbol{R}_{\boldsymbol{m}}} G_\kappa(\boldsymbol{x}-\boldsymbol{R}_{\boldsymbol{m}}), \tag{2.1}$$

where

$$G_\kappa(\boldsymbol{x}) = \begin{cases} \frac{\mathrm{i}}{4}H_0^{(1)}(\kappa|\boldsymbol{x}|) & \text{for } d=2, \\ \frac{1}{4\pi}\frac{\mathrm{e}^{\mathrm{i}\kappa|\boldsymbol{x}|}}{|\boldsymbol{x}|} & \text{for } d=3 \end{cases} \tag{2.2}$$

denotes the free-space Green function for the Helmholtz equation with wavenumber κ in d-dimensional space.

The quasi-periodic Green function can be interpreted as the field generated by an infinite number of radiating point sources distributed periodically and acting coherently through a suitable phase factor. A direct application of the Poisson summation formula [Sim15] to (2.1) yields the corresponding spectral representations for the quasi-periodic Green function:

$$G_\kappa^q(\boldsymbol{x}) = \frac{1}{\mathcal{A}}\frac{\mathrm{i}}{2}\sum_{\boldsymbol{m}\in\mathbb{Z}^{d_\Lambda}} \frac{\mathrm{e}^{\mathrm{i}\boldsymbol{\alpha}_{\boldsymbol{m}}\cdot\boldsymbol{x}}\mathrm{e}^{\mathrm{i}\beta_{\boldsymbol{m}}|x_d|}}{\beta_{\boldsymbol{m}}}, \quad d=2,3 \quad \text{and} \quad d_\lambda = d-1 \tag{2.3}$$

$$G_\kappa^q(\boldsymbol{x}) = \frac{1}{\mathcal{A}}\frac{\mathrm{i}}{4}\sum_{\boldsymbol{m}\in\mathbb{Z}^{d_\Lambda}} \mathrm{e}^{\mathrm{i}\boldsymbol{\alpha}_{\boldsymbol{m}}\cdot\boldsymbol{x}} H_0^{(1)}\left(\beta_{\boldsymbol{m}}\sqrt{x_2^2+x_3^2}\right), \quad d=3, d_\lambda = 1. \tag{2.4}$$

Here $\mathcal{A}$ denotes the area of the unit cell,

$$\mathcal{A} = \begin{cases} |\boldsymbol{v_1}| & \text{if } d_\lambda = 1 \\ |\boldsymbol{v_1}\times\boldsymbol{v_2}| & \text{if } d_\lambda = 2 \end{cases} \tag{2.5}$$

and the parameters $\boldsymbol{\alpha}_{\boldsymbol{m}}$ and $\beta_{\boldsymbol{m}}$ are defined in (1.27). The spectral representations (2.3)– (2.4) manifest the singular character of the quasi-periodic Green function at configurations for which the scalar $\beta_{\boldsymbol{m}}$ vanishes for some value or (finite number of) values of the index $\boldsymbol{m}$: as such singular configurations are approached, singularities of type $\beta_{\boldsymbol{m}}^{-1}$ and $\log(\beta_{\boldsymbol{m}})$ arise for $d = d_\Lambda + 1$ and $d = d_\Lambda + 2$, respectively. A triple $(\kappa, \boldsymbol{\alpha}, \Lambda)$ for which $\beta_{\boldsymbol{m}}$ vanishes for some value of $\boldsymbol{m}$ is said to be a

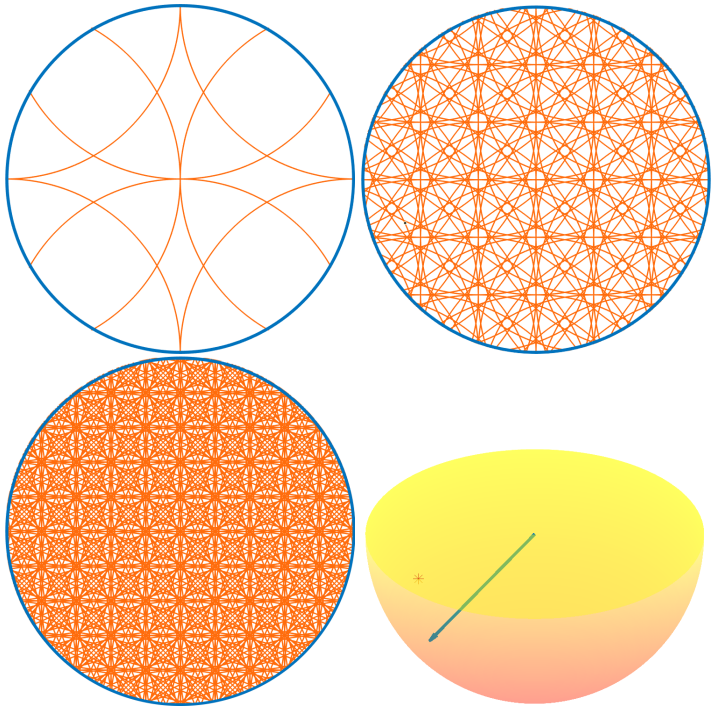

Figure 2.1: Density of RW-anomalies for a bi-periodic array ($d_\Lambda = 2$) in three-dimensional space ($d = 3$) where $\boldsymbol{v_1} = (L, 0, 0)$, $\boldsymbol{v_2} = (0, L, 0)$ with $L = 1\lambda$ (top-left), $L = 3\lambda$ (top-right) and $L = 5\lambda$ (bottom-left). Each point in the lines inside the circles corresponds to an incoming direction of a plane wave (which impacts directly in the possible value of $\boldsymbol{\alpha}$) giving rise to an RW anomalous configuration. (In the present $d = 3$ case each plane-wave incoming direction represents a point in the lower hemisphere in the bottom-right image. The two-dimensional figures, which are presented to facilitate visualization, are obtained by projecting these points into a circle of radius 1 in the plane via the map $(x, y, z) \to (x, y, 0)$.)

Rayleigh-Wood (RW) anomaly triple; clearly, at RW anomalies the (finite) set

$$\mathcal{W} = \mathcal{W}(\kappa, \boldsymbol{\alpha}, \Lambda) = \left\{\boldsymbol{m} \in \mathbb{Z}^{d_\Lambda} : \kappa^2 - |\boldsymbol{\alpha} + \boldsymbol{K_m}|^2 = 0\right\} = \left\{\boldsymbol{m} \in \mathbb{Z}^{d_\Lambda} : \beta_{\boldsymbol{m}} = 0\right\} \tag{2.6}$$

is non-empty.

The spectral representations (2.3) and (2.4) provide an exceptional computational tool whenever the following conditions are satisfied: 1) The triple $(\kappa, \boldsymbol{\alpha}, \Lambda)$ is not a RW anomaly; and 2) The magnitude $|\boldsymbol{x}^\perp|$ of the projection $\boldsymbol{x}^\perp$ is relatively large compared to the period—since, in such cases, the series (2.3) and (2.4) converge exponentially fast to the corresponding quasi-periodic Green functions (see Section 3.1 for a more detailed analysis). For small values of $|\boldsymbol{x}^\perp|$, however, the convergence rates deteriorates. To compute the quasi-periodic Green functions

in the latter regime alternative representations must be used which, like the one displayed in equation (2.1), make explicit the spatial Green-function singularities. The representation (2.1) is only conditionally convergent, however, and therefore finite truncations of it yield poorly convergent approximations. For example, a straightforward truncation in the $d_\Lambda = 1$ case converges with an error that decays like the inverse of the square root of the numbers of terms used.

A number of methodologies have been developed which, for configurations away from RW-anomalies, can be used to evaluate the quasi-periodic Green function efficiently and accurately—including lattice sums [Den+17b; Lin10; Lin98], Laplace-type integral representation [BH09; BH10; KNR11; KR09; Vey+91], the Ewald summation method [Are+13; CWJ07; Ewa21; Lin10; ND57] and, recently, the Windowed Green function and the shifted Green function methods [BD14; Bru+16; Bru+17]. Except for the shift-based Green function approach, however, all of these methodologies do fail at RW-anomalies since the classical quasi-periodic Green function is not even defined in that case. Sections 2.1, 2.2 and 2.3 describe the Laplace-type integral, Ewald and shifted Green function approaches respectively, which can all be (separately) used as base elements for the strategy proposed in Chapter 4 for the RW anomaly.

2.1 Laplace-type integral method ($d_\Lambda = 1$)

In the case $d_\Lambda = 1$, Laplace transform methods can be used to express the quasi-periodic Green functions as a sum of a single free-space Green function and certain Laplace-type integrals. (Laplace-type Integral methods have been successfully extended to bi-periodic arrays, $d_\Lambda = 2$, for Cartesian lattices [Lin10]—for which the generating vectors $\boldsymbol{v_1}$ and $\boldsymbol{v_2}$ are orthogonal—but we do not consider such extensions in this work.) A full description of the $d_\Lambda = 1$ methods can be found in [KNR11; KR09; Lin10; Lin98; Vey+91].

Assuming $\boldsymbol{v_1} = L\hat{\boldsymbol{x}_1}$ (L is the period of the lattice) the classical quasi-periodic Green function (2.1) in the case $d_\Lambda = 1$ is given by

$$G^q_\kappa(\boldsymbol{x}) = \sum_{m\le -1} \mathrm{e}^{\mathrm{i}\alpha\cdot\hat{\boldsymbol{x}_1}Lm} G(\boldsymbol{x} - mL\hat{\boldsymbol{x}_1}) + G_\kappa(\boldsymbol{x}) + \sum_{m\ge 1} \mathrm{e}^{\mathrm{i}\alpha\cdot\hat{\boldsymbol{x}_1}Lm} G(\boldsymbol{x} - mL\hat{\boldsymbol{x}_1}). \quad (2.7)$$

Expressing G_κ in terms of its Laplace transform [Bat54, Eq. 5.14.9] and [Erd+54, Eq. 4.15.19] we obtain

$$G_\kappa(\boldsymbol{x}) = \frac{\mathrm{e}^{\mathrm{i}\kappa|x_1|}}{2\pi} \int_0^\infty \mathrm{e}^{-\kappa|x_1|u} \frac{f_d\left(\kappa|\boldsymbol{x}^\perp|\sqrt{u^2 - 2\mathrm{i}u}\right)}{\left(u^2 - 2\mathrm{i}u\right)^{(3-d)/2}} du, \quad (2.8)$$

where

$$f_d(t) = \cos(t) \quad \text{for } d = 2 \quad \text{and} \quad f_d(t) = \frac{\kappa}{2} J_0(t) \quad \text{for } d = 3, \tag{2.9}$$

and where J_0 denotes the zero-th order Bessel function. For evaluation points $\boldsymbol{x}$ within the unit cell ($|x_1| \leq L$), substitution of (2.8) into the last sum in (2.7) yields

$$\frac{\mathrm{e}^{-\mathrm{i}\kappa x_1}}{2\pi} \int_0^\infty \mathrm{e}^{\kappa x_1 u} \left(\sum_{m=1}^{\infty} \mathrm{e}^{-(\kappa u - \mathrm{i}(\alpha \cdot \hat{\boldsymbol{x}_1} + \kappa))mL} \right) \frac{f_d\left(\kappa |\boldsymbol{x}^\perp| \sqrt{u^2 - 2\mathrm{i}u}\right)}{\left(u^2 - 2\mathrm{i}u\right)^{(3-d)/2}} du, \tag{2.10}$$

or, equivalently,

$$\frac{\mathrm{e}^{-\mathrm{i}\kappa x_1}}{2\pi} \int_0^\infty \frac{\mathrm{e}^{-\kappa(L-x_1)u}}{\mathrm{e}^{-\mathrm{i}(\alpha \cdot \hat{\boldsymbol{x}_1} + \kappa)L} - \mathrm{e}^{-\kappa L u}} \frac{f_d\left(\kappa |\boldsymbol{x}^\perp| \sqrt{u^2 - 2\mathrm{i}u}\right)}{\left(u^2 - 2\mathrm{i}u\right)^{(3-d)/2}} du. \tag{2.11}$$

Using a similar derivation for the first series in (2.7) the Laplace-type integral representation

$$G_\kappa^q(\boldsymbol{x}) = G_\kappa(\boldsymbol{x}) + \frac{\mathrm{e}^{-\mathrm{i}\kappa \boldsymbol{x} \cdot \hat{\boldsymbol{e}}}}{2\pi} I^+(\boldsymbol{x}) + \frac{\mathrm{e}^{\mathrm{i}\kappa \boldsymbol{x} \cdot \hat{\boldsymbol{e}}}}{2\pi} I^-(\boldsymbol{x}) \tag{2.12}$$

results, where

$$I^\pm(\boldsymbol{x}) = \int_0^\infty \frac{\mathrm{e}^{-\kappa(L \pm x_1)u}}{\mathrm{e}^{-\mathrm{i}(\kappa \mp \alpha \cdot \hat{\boldsymbol{x}_1})L} - \mathrm{e}^{-\kappa L u}} \frac{f_d\left(\kappa |\boldsymbol{x}^\perp| \sqrt{u^2 - 2\mathrm{i}u}\right)}{\left(u^2 - 2\mathrm{i}u\right)^{(3-d)/2}} du. \tag{2.13}$$

The generalized Gauss-Laguerre quadrature rule [Pre+07] is well suited for evaluation of the integrals $I^\pm$. In contrast to the spectral representations, formula (2.12) makes explicit the spatial singularity around the origin of the quasi-periodic Green function but it does not present in a similarly explicit form the singularity at RW anomalies—which is explicit in (2.3) and (2.4). The Laplace-type integral representation (2.12), which was used in [BH09; BH10] to produce efficient periodic scattering solvers for challenging configurations, is also a key component in the analysis performed in [KNR11; KR09] for the periodic problem at high frequencies. The strategies presented in those references cannot be applied at RW anomalies, however.

As detailed in what follows, each of the integrals $I^\pm$ can be re-expressed as the sum of two terms, one of which explicitly captures the RW-anomaly singularities in (2.3) and (2.4), while the other, which is given by a rapidly convergent integral, remains bounded near RW anomalies.

To see this we first note that, except at RW-anomalies the denominator $\mathrm{e}^{-\mathrm{i}(\kappa\mp\boldsymbol{\alpha}\cdot\hat{\boldsymbol{x}}_1)L} - \mathrm{e}^{-\kappa L u}$ in (2.13) does not vanishes in the integration domain. Indeed, the zeroes of the denominator are the purely imaginary numbers $\mathrm{i}u_m^{\pm}$, where

$$\kappa u_m^{\pm} = \kappa \mp \boldsymbol{\alpha_m} \cdot \hat{\boldsymbol{x}}_1, \tag{2.14}$$

Clearly these zeroes can only be real if $\kappa u_m^{\pm}$ vanishes, or, equivalently, if the RW-anomaly condition $|\boldsymbol{\alpha_m}| = \kappa$ is satisfied. In particular, at RW-anomalies, at least one of the integrals $I^{\pm}$ diverges.

In order to explicitly extract the singular term we multiply and divide the integrand in (2.13) by $u - \mathrm{i}u_m^{\pm}$ and we obtain

$$I^{\pm}(\boldsymbol{x}) = \int_0^{\infty} \frac{\mathrm{e}^{-\kappa(L\pm x_1)u}}{u - \mathrm{i}u_m^{\pm}} \frac{1}{u^{(3-d)/2}} g_d(u) du, \tag{2.15}$$

where we have set

$$g_d(u) = \frac{u - \mathrm{i}u_m^{\pm}}{\mathrm{e}^{-\mathrm{i}(\alpha\cdot\hat{\boldsymbol{x}}_1\mp\kappa)L} - \mathrm{e}^{-\kappa L u}} \frac{f_d\left(\kappa|\boldsymbol{x}^{\perp}|\sqrt{u^2 - 2\mathrm{i}u}\right)}{(u - 2\mathrm{i})^{(3-d)/2}}.$$

As a function of the real variable u, g_d is an infinitely differentiable function around the origin (since in either case, $d = 2$ and $d = 3$, the Taylor series of the analytic function f_d around zero only contains even powers). Adding and subtracting $g_d(\mathrm{i}u_m^{\pm})$ from $g_d(u)$ in (2.15) we obtain

$$I^{\pm}(\boldsymbol{x}) = \int_0^{\infty} \frac{\mathrm{e}^{-\kappa(L\pm x_1)u}}{u^{(3-d)/2}} \frac{g_d(u) - g_d(\mathrm{i}u_m^{\pm})}{u - \mathrm{i}u_m^{\pm}} du + g_d(\mathrm{i}u_m^{\pm}) \int_0^{\infty} \frac{\mathrm{e}^{-\kappa(L\pm x_1)u}}{u - \mathrm{i}u_m^{\pm}} \frac{du}{u^{(3-d)/2}}. \tag{2.16}$$

Clearly, the integrand in the first term of the right hand side of equation (2.16) is regular and can be evaluated by means of the Gauss-Laguerre quadrature rule. The last integral on the right-hand side, in turn, can be expressed in terms of special functions. Indeed, in the case $d = 2$ using the relation [DLM17, Eq. 7.7.2]

$$\mathrm{e}^{-z^2}\mathrm{erfc}\,(-\mathrm{i}z) = \frac{z}{\pi\mathrm{i}} \int_{-\infty}^{\infty} \frac{\mathrm{e}^{-t^2}}{t^2 - z^2} dt, \quad \mathrm{Im}(z) > 0 \tag{2.17}$$

and the change of variables $u = t^2$ we obtain

$$\int_0^{\infty} \frac{\mathrm{e}^{-\kappa(L\pm x_1)u}}{u - \mathrm{i}u_m^{\pm}} \frac{du}{\sqrt{u}} = \pi \mathrm{e}^{\mathrm{i}\pi/4} \mathrm{e}^{-\mathrm{i}\kappa u_m^{\pm}(L\pm x_1)} \frac{\mathrm{erfc}\left(\mathrm{e}^{-\mathrm{i}\pi/4}\sqrt{\kappa u_m^{\pm}(L \pm x_1)}\right)}{\sqrt{u_m^{\pm}}}, \tag{2.18}$$

where erfc denotes the analytic extension of the complementary error function

$$\operatorname{erfc}(z) = \frac{2}{\sqrt{\pi}} \int_z^\infty \mathrm{e}^{-t^2} dt \tag{2.19}$$

to the complex plane. For the case $d = 3$, in turn, we have

$$\int_0^\infty \frac{\mathrm{e}^{-\kappa(L\pm x_1)u}}{u - \mathrm{i}u_m^\pm} du = \mathrm{e}^{-\mathrm{i}\kappa u_m^\pm (L\pm x_1)} E_1\left(-\mathrm{i}\kappa u_m^\pm (L \pm x_1)\right) \tag{2.20}$$

where E_1 denotes the analytic extension of the exponential integral

$$E_1(z) = \int_z^\infty \frac{\mathrm{e}^{-t}}{t} dt,$$

to the maximal analyticity domain $\mathbb{C} \setminus (-\infty, 0]$ (that is also commonly used as the principal branch of the logarithm function). The factor $g_d(\mathrm{i}u_m)$ that multiplies the last integral on the right-hand side of equation (2.16) (in either case, $d = 2$ or $d = 3$) in turn, is given by

$$g_d(\mathrm{i}u_m) = \frac{\mathrm{e}^{\mathrm{i}\kappa L u_m^\pm}}{\kappa L} \frac{f_d\left(\kappa|\boldsymbol{x}^\perp|\sqrt{2u_m - u_m^2}\right)}{(\mathrm{i}(u_m - 2))^{(3-d)/2}}, \tag{2.21}$$

as it can be checked easily. In view of equations (2.18), (2.20) and (2.21) together with the relation $\beta_m(\kappa) = \kappa\sqrt{2u_m - u_m^2}$ (that results from (1.27) and (2.14)) it follows that the second term on the right hand side of (2.16) equals

$$\pi \frac{\mathrm{i}}{L} \mathrm{e}^{\mp \mathrm{i}\kappa u_m^\pm x_1} \operatorname{erfc}\left(\mathrm{e}^{-\mathrm{i}\pi/4}\sqrt{\kappa u_m^\pm (L \pm x_1)}\right) \frac{\cos\left(\beta_m(\kappa)|\boldsymbol{x}^\perp|\right)}{\beta_m(\kappa)} \tag{2.22}$$

for $d = 2$ and

$$\frac{1}{2L} \mathrm{e}^{\mp \mathrm{i}\kappa u_m^\pm x_1} J_0\left(\beta_m(\kappa)|\boldsymbol{x}^\perp|\right) E_1\left(-\mathrm{i}\frac{\beta_m(\kappa)^2}{\kappa + \sqrt{\kappa^2 - \beta_m(\kappa)^2}}(L \pm x_1)\right) \tag{2.23}$$

if $d = 3$. In either the case $d = 2$ or $d = 3$, substituting the last integral in equation (2.16) by the corresponding expression (2.22) or (2.23), and then replacing the ensuing formulae for $I^\pm$ into (2.12), yields an expression for the quasi-periodic Green function G_κ^q in terms of special functions and integrals that do not suffer from singularity at RW-anomalies. The $1/\beta_m$ Green-function singularity in the case $d = 2$

is explicitly displayed in (2.22), while the corresponding logarithmic singularity in the case $d = 3$ can be made explicit by using the relation [DLM17, Eq. 6.6.2]

$$E_1(z) = -C - \log(z) - \sum_{k=1}^{\infty} \frac{(-z)^k}{k\,k!}. \tag{2.24}$$

The special-function values required to evaluate the expressions (2.22) and (2.23) can generally be obtained without difficulty by means of well known algorithms, as indicated in Chapter 3. As discussed in that chapter, however, the necessary integrals (namely, the first integral expression on the right-hand side in (2.16) for $d = 2$ and $d = 3$), while regular at RW-anomalies, still present significant challenges in the high-frequency regimes.

2.2 Ewald summation method ($d_\Lambda = 1, 2$)

The Ewald summation method was originally introduced [Ewa21] as a technique to evaluate the electrostatic potential energy in crystals; its derivation in the context of the Helmholtz equation and, generally, wave-propagation phenomena is quite intricate, but a detailed description can be found in Appendix B. The representations that result after the application of this procedure expresses G_κ^q as a sum of two infinite series G_Λ^q and $G_{\Lambda^*}^q$,

$$G_\kappa^q = G_\Lambda^q + G_{\Lambda^*}^q, \tag{2.25}$$

indexed by elements in the lattices Λ and Λ^*, and whose general terms decay as $\exp(-\eta^2 |\boldsymbol{R}_{\boldsymbol{n}}|^2)$ and $\exp(-|\boldsymbol{K}_{\boldsymbol{n}}|^2/4\eta^2)$ respectively. The constant $\eta > 0$, which arises as a splitting parameter of an integral representation of the free-space Green function, is carefully chosen in order to maximize the convergence rate of the two series as well as to ensure the stability of the method (see [KM00; LBA08; SM07]).

In what follows we present explicit expressions for G_Λ^q and $G_{\Lambda^*}^q$ for various values of d and d_Λ; a derivation of these expressions, which can be found in [Lin10], is presented in Appendix B for easy reference. To display these expressions we call $\rho_{\boldsymbol{n}}$ the Euclidean distance between an observation point $\boldsymbol{x}$ and a lattice point $\boldsymbol{R}_{\boldsymbol{n}}$, and we denote by $E_j = E_j(z)$ the exponential integral with complex argument z:

$$E_j(z) = \int_z^\infty \frac{\mathrm{e}^{-t}}{t^j} dt. \tag{2.26}$$

Then, for $d = 2$ and $d_\Lambda \leq d$, G_Λ^q is given by

$$G_\Lambda^q(\boldsymbol{x}) = \frac{1}{4\pi} \sum_{\boldsymbol{m} \in \mathbb{Z}^{d_\Lambda}} \mathrm{e}^{\mathrm{i}\boldsymbol{\alpha}\cdot\boldsymbol{R}_{\boldsymbol{m}}} \sum_{j=0}^{\infty} \frac{1}{j!} \left(\frac{\kappa}{2\eta}\right)^{2j} E_{j+1}\left(\eta^2 \rho_{\boldsymbol{m}}^2\right), \tag{2.27}$$

while for $d = 3$ and $d_\Lambda \le d$,

$$G^q_\Lambda(\boldsymbol{x}) = \frac{1}{8\pi} \sum_{\boldsymbol{m}\in\mathbb{Z}^{d_\Lambda}} \frac{\mathrm{e}^{\mathrm{i}\boldsymbol{\alpha}\cdot\boldsymbol{R}_{\boldsymbol{m}}}}{\rho_{\boldsymbol{m}}} \left[\mathrm{e}^{\mathrm{i}k\rho_{\boldsymbol{m}}}\mathrm{erfc}\left(\eta\rho_{\boldsymbol{m}} + \mathrm{i}\frac{\kappa}{2\eta}\right) + \mathrm{e}^{-\mathrm{i}k\rho_{\boldsymbol{m}}}\mathrm{erfc}\left(\eta\rho_{\boldsymbol{m}} - \mathrm{i}\frac{\kappa}{2\eta}\right)\right]. \tag{2.28}$$

The corresponding expressions for $G^q_{\Lambda^*}$ are as follows. For $d = 2, 3$ and $d_\Lambda = d - 1$ $G^q_{\Lambda^*}$ is given by

$$G^q_{\Lambda^*}(\boldsymbol{x}) = \frac{\mathrm{i}}{4\mathcal{A}} \sum_{\boldsymbol{m}\in\mathbb{Z}^{d_\Lambda}} \frac{\mathrm{e}^{\mathrm{i}\boldsymbol{\alpha}_{\boldsymbol{m}}\cdot\boldsymbol{x}}}{\beta_{\boldsymbol{m}}} \left[\mathrm{e}^{\mathrm{i}\beta_{\boldsymbol{m}}x_d}\mathrm{erfc}\left(-\eta x_d - \mathrm{i}\frac{\beta_{\boldsymbol{m}}}{2\eta}\right) + \mathrm{e}^{-\mathrm{i}\beta_{\boldsymbol{m}}x_d}\mathrm{erfc}\left(\eta x_d - \mathrm{i}\frac{\beta_{\boldsymbol{m}}}{2\eta}\right)\right]. \tag{2.29}$$

while for $d = 3$ and $d_\Lambda = d - 2 = 1$

$$G^q_{\Lambda^*}(\boldsymbol{x}) = \frac{1}{4\pi\mathcal{A}} \sum_{\boldsymbol{m}\in\mathbb{Z}^{d_\Lambda}} \mathrm{e}^{i\boldsymbol{\alpha}_{\boldsymbol{m}}\cdot\boldsymbol{x}} \sum_{j=0}^{\infty} \frac{1}{j!} \left(\mathrm{i}\eta\sqrt{x_2^2 + x_3^2}\right)^{2j} E_{j+1}\left(-\frac{\beta_{\boldsymbol{m}}^2}{4\eta^2}\right). \tag{2.30}$$

Note that G_Λ depends only on the spatial dimension d irrespectively of the dimension d_Λ of the lattice, whereas G_{Λ^*} depends only on the complementary dimension $d - d_\Lambda$ but not directly on d.

2.3 Shifted Green function ($d_\Lambda = 1, 2$)

The conditionally convergent sum (2.1) owes its poor convergence rate to the slow decay of the free-space Green function at infinity. As detailed in [BD14] and [Bru+17], use of a certain half-space shifted Green function produces quasi-periodic Green functions with a user-prescribed algebraic decay, convergent at any configuration, including RW-anomalies. In brief, given a shift-parameter $h > 0$ and a unit-vector $\hat{\boldsymbol{v}}$, the half-space shifted Green function of order $j \ge 0$ is given by

$$G_{\kappa,j}(\boldsymbol{x}) = \sum_{\ell=0}^{j} (-1)^\ell \binom{j}{\ell} G_\kappa(\boldsymbol{x} + \ell h\hat{\boldsymbol{v}}). \tag{2.31}$$

It can be shown that [BD14; Bru+17] given $M > 0$, there exists a constant $C(h, M)$ such that for $|\boldsymbol{x}\cdot\hat{\boldsymbol{v}}| \le M$ we have

$$|G_{\kappa,j}(\boldsymbol{x})| \le C(h, M)|\boldsymbol{x}^{\parallel}|^{-(j+1)/2} \tag{2.32}$$

if j is an even positive integer and

$$|G_{\kappa,j}(\boldsymbol{x})| \le C(h, M)|\boldsymbol{x}^{\parallel}|^{-(j/2+1)} \tag{2.33}$$

if j is an odd positive integer. In these estimations $\boldsymbol{x}^{\parallel}$ is the projection of the point $\boldsymbol{x}$ into the plane orthogonal to $\hat{\boldsymbol{\nu}}$. The shifted quasi-periodic Green function, in turn, is given by

$$G^q_{\kappa,j}(\boldsymbol{x}) = \sum_{\boldsymbol{m}\in\mathbb{Z}^{d_\Lambda}} \mathrm{e}^{\mathrm{i}\boldsymbol{\alpha}\cdot\boldsymbol{R_m}} G_{\kappa,j}(\boldsymbol{x}-\boldsymbol{R_m}), \tag{2.34}$$

where the unit-vector $\hat{\boldsymbol{\nu}}$ used to define $G_{\kappa,j}$ is taken orthogonal to the plane that contains the lattice Λ. It is clear from (2.31) that the classical quasi-periodic Green function can be written in terms of $G^q_{\kappa,j}$ as

$$G^q_\kappa(\boldsymbol{x}) = G^q_{\kappa,j}(\boldsymbol{x}) - \sum_{\ell=1}^{j}(-1)^\ell \binom{j}{\ell} G^q(\boldsymbol{x}+\ell h\hat{\boldsymbol{\nu}}). \tag{2.35}$$

If the triple $(\kappa, \boldsymbol{\alpha}, \Lambda)$ is not an anomalous configuration and for points for which the quasi-periodic Green functions in the finite sum in equation (2.35) can be expressed by their corresponding spectral representations it follows that (cf. [BF17, Eqs. 4.5, 4.6])

$$G^q_\kappa(\boldsymbol{x}) = G^q_j(\boldsymbol{x}) - \frac{\mathrm{i}}{4\mathcal{A}} \sum_{m\in\mathbb{Z}} \sum_{\ell=1}^{j}(-1)^\ell \binom{j}{\ell} \mathrm{e}^{\mathrm{i}\alpha_m x_1} H_0^{(1)}\left(\beta_m(\kappa)|\boldsymbol{x}^{\perp}+\ell h\hat{\boldsymbol{\nu}}|\right) \tag{2.36}$$

if $d_\lambda = 1$, $d = 3$ and

$$G^q_\kappa(\boldsymbol{x}) = G^q_j(\boldsymbol{x}) - \frac{\mathrm{i}}{2\mathcal{A}} \sum_{\boldsymbol{m}\in\mathbb{Z}^{d_\lambda}} \sum_{\ell=1}^{j}(-1)^\ell \binom{j}{\ell} \frac{\mathrm{e}^{\mathrm{i}\boldsymbol{\alpha_m}\cdot\boldsymbol{x}+\mathrm{i}\beta_{\boldsymbol{m}}|x_d+\ell h|}}{\beta_{\boldsymbol{m}}} \tag{2.37}$$

if $d_\lambda = d-1$. Equations (2.36) and (2.37), only valid for non-anomalous configurations, express the quasi-periodic Green function G^q_κ as a sum of two quantities, the first one contains the spatial singularities ($\boldsymbol{x}\in\Lambda$), while the second one contains the singular terms which arise as a RW-anomaly is approached. Both (2.36) and (2.37) thus yield jointly spatial-spectral fast-convergent representations of G^q_κ that exhibit explicitly all spatial and spectral singular terms. On the basis of (2.37), the contribution [BF17] introduced the use of the Woodbury-Sherman-Morrison formulae as a means to overcome the difficulties around RW-anomalies for problems of scattering by arrays of particles in two-dimensional space. The present contribution extends that work to enable applicability of the overall methodology to arbitrary periodic domains—by utilizing either the shifted Green function in the form (2.35) or, alternatively, either a modified version of the Laplace-type integral representation (2.12) (for $d_\Lambda = 1$, $d = 2, 3$) or, finally, a modified version of the Ewald-summation expression (2.25).

Chapter 3

NUMERICAL IMPLEMENTATIONS

This chapter describes high-order methods for the discretization of the integral equation (4.4), which lead to fast and highly-accurate numerical solvers for simulation of wave-scattering by periodic media.

Section 3.1 summarizes succinctly the various strategies used in this contribution for the evaluation of the special functions with complex argument that are required as part of the spectral, Laplace-type integral and Ewald representations. That section also presents a description of the main difficulties presented by those evaluations in the last two cases, and it compares the performance and stability of the Laplace-type integral and Ewald methods along with the one based on use of the shifted Green function for a variety of configurations. (The spectral representation, while useful as a component of other methods, cannot be used by itself as part of a quasi-periodic solver, in view of its inability to resolve the spatial Green-function singularity.) The comparisons show that the Ewald representation provides the best convergence properties for small periods in the case $d_\Lambda = d - 1$, but becomes unstable in higher-frequency regimes and in the case $d_\lambda = 1, d = 3$ for which the shifted Green-function becomes computationally advantageous[1]. Thus, the numerical software produced for this thesis utilize the Ewald method and the shifted Green function method for those cases accordingly, obtaining fast and highly-accurate solvers.

All numerical boundary integral equations methods need the evaluation of certain convolution-type integrals whose kernel present weak (integrable) singularities of order $O(\log(r))$ and $O(1/r)$ $(r \to 0)$ for $d = 2$ and $d = 3$ respectively. Section (3.2) describes the numerical techniques used in this work to compute such weakly-singular integrals.

3.1 Evaluation of quasi-periodic Green functions

Spectral series

As mentioned in Chapter 2, the spectral representations (2.3)–(2.4) give rise to exceptional performance unless either $|\boldsymbol{x}^\perp|$ is small or the scattering configuration

[1] All times in Section (3.1) were measured in a single core of an Intel i5-8250U processor in a personal computer.

$(\kappa, \boldsymbol{\alpha}, \Lambda)$ is an RW-anomaly. More specifically, since the $\boldsymbol{m}$-th term of the spectral series has an asymptotic behavior of order $\mathrm{e}^{-2\pi/L\|\boldsymbol{m}\|_\infty|\boldsymbol{x}^\perp|}$ as $\|\boldsymbol{m}\|_\infty \to \infty$ (L is the period if $d_\Lambda = 1$ or the largest period if $d_\Lambda = 2$), a truncation of the spectral series with $\|\boldsymbol{m}\|_\infty < N$ yields an error of order

$$O\left(\frac{\mathrm{e}^{-N2\pi|\boldsymbol{x}^\perp|/L}}{1-\mathrm{e}^{-2\pi|\boldsymbol{x}^\perp|/L}}\right). \tag{3.1}$$

The exponential decay of the terms of the spectral series (2.3) and (2.4) only manifests itself for values of $\boldsymbol{m}$ satisfying $\kappa^2 < |\boldsymbol{\alpha}_{\boldsymbol{m}}|^2$. Since these terms decay slowly for the propagating-mode indexes $\boldsymbol{m}$ satisfying $\kappa^2 \geq |\boldsymbol{\alpha}_{\boldsymbol{m}}|^2$, if any accuracy is to be expected, the truncation parameter N must be sufficiently large so as to include, in the corresponding truncation, all propagating-mode terms. Thus, to achieve an ϵ-accuracy the truncation parameter N must satisfy

$$N \gtrsim \frac{\kappa L}{2\pi} + O\left(\frac{L}{2\pi|\boldsymbol{x}^\perp|}\log\left(\frac{1}{\epsilon(1-\mathrm{e}^{-2\pi|\boldsymbol{x}^\perp|/L})}\right)\right). \tag{3.2}$$

It can be clearly seen from this estimate the advantages and difficulties of using truncations of the spectral series to compute G_κ^q for large and small values of $|\boldsymbol{x}^\perp|$ respectively; in this contribution we have utilized the spectral series whenever $|\boldsymbol{x}^\perp| > L$, and, depending on the characteristics of each problem, we have employed one of the three alternative representations discussed in Chapter 2 in other cases. (As can be appreciated from the results in Chapter 5, the first two methods are efficient for acoustically small-medium configurations; as explained in what follows and exemplified in Tables 3.2, 3.4, for larger periods these techniques present stability issues due to the exponential growth of special functions evaluated in the complex plane resulting in loss of accuracy. The shifted Green-function approach, in contrast, does not suffer from these difficulties and it proves advantageous in a higher-frequency regime as illustrated in Table 3.8.)

Ewald and Laplace-type integral methods: Special functions and instability sources

In what follows we summarize the algorithms we use for the evaluation of the special functions that are required in the implementations of the Ewald and Laplace-type integral representation methods, and we review certain sources of instability that arise as special functions are incorporated in the corresponding implementations. All of the special-function methods utilized in this thesis can be found in the ACM Transactions of Mathematical Software (ACM TOMS).

Period \ N	16	32	64	128
2.5λ	0.15E-5	0.12E-8	0.49E-13	0.48E-14
4.5λ	0.21E-4	0.17E-7	0.68E-12	0.93E-14
8.5λ	0.18E-3	0.11E-6	0.31E-11	0.14E-12
Avg. computing time (s)	7.51-3	1.31E-2	2.31E-2	4.31E-2

Table 3.1: Accuracy and performance of the Laplace-type Integral method, away from RW-anomalies, for a periodic array with $d_\Lambda = 1$, $d = 3$ at a non-anomalous configuration. In this example, $\boldsymbol{\alpha} = (0, 0, 0)$. The displayed values correspond to the maximum relative error when the integrals $I^\pm$ in (2.12) are evaluated by means of the Gauss-Laguerre quadrature rule with N nodes sampled at 100 points of the form $\boldsymbol{x}_i = ((i/100 - 0.5)L, \sqrt{2}L/4, \sqrt{2}L/4)$, $i = 0 \ldots 99$ where L denotes the period (in all these cases, $|\boldsymbol{x}^\perp| = L/2$). The reference value is obtained by means of the spectral representation (2.4) truncated with as many terms as specified in (3.2) to obtain machine precision.

As mentioned in Chapter 2 and demonstrated in Table 3.1, the integrals (2.13) associated with the Laplace-type integral representation method embodied in equation (2.12) can be efficiently evaluated by means of Gaussian quadrature rules. In this contribution the weights and nodes for the Gauss-Laguerre rule are obtained applying TOMS Algorithm 655 [EK87]. In the case $d_\Lambda = 1$, $d = 3$, it is additionally necessary to compute the Bessel function J_0 with complex argument (see equation (2.9)); this task is tackled by exploiting Algorithm 912 [Kod11]. Since the magnitudes of the cosine and the Bessel function of the first kind grow exponentially fast as the absolute value of the argument's imaginary part increases, the direct integration strategy typically results in loss of accuracy under two commonly occurring situations, namely, whenever we have either 1) large values of the product of the wavenumber and the period, or 2) large values of the quotient of the magnitude $|\boldsymbol{x}^\perp|$ of the orthogonal projection and the period (see Table 3.2). Extensions of our methods to high-frequency approaches like those presented in [KNR11] and [KR09], which would enable applicability of those approaches to RW anomalous configurations, will be left for future work.

The Ewald representation (2.28) and (2.29), in turn, requires the evaluation of the exponential integrals $E_j(z)$ (equation (2.26)) for real values of z, as well as the complementary error function erfc (equation (2.19)) for complex values of z. The exponential integrals E_j, on one hand, can be computed by means of the

Period \ N	128	256	512
16.5λ	0.22E-11	0.30E-11	0.51E-11
32.5λ	0.16E-7	0.18E-7	0.21E-7
64.5λ	0.76E-1	0.13E+0	0.60E-1

Period \ N	128	256	512
16.5λ	0.61E-7	0.49E-7	0.65E-7
32.5λ	0.16E+1	0.29E+1	0.27E+1
64.5λ	0.33E+16	0.12E+16	0.13E+16

Table 3.2: Same experiment as in Table 3.1 with larger periods, a larger number of quadrature nodes and for two values of $|\boldsymbol{x}^{\perp}|$: $0.5L$ (top) and $0.75L$ (bottom). The large magnitude of the Bessel function of the first kind produces a loss of accuracy in the Laplace-type integral method as the magnitude of the period increases.

recursion [DLM17, p. 8.19.12]

$$E_{j+1}(z) = \frac{\mathrm{e}^{-z} - zE_j(z)}{j}$$

or directly through the relation [DLM17, p. 8.19.7]

$$E_j(z) = \frac{1}{(j-1)!}\left[(-z)^{j-1}E_1(z) + \mathrm{e}^{-z}\sum_{n=1}^{j-2}(j-2-n)!(-z)^n\right]. \tag{3.3}$$

Our algorithms utilize the latter approach, which provides a more stable evaluation algorithm than the alternative recursive method. (The necessary polynomial coefficients in (3.3) can be pre-computed for all necessary values of j and then utilized to evaluate the needed polynomials by means of Horner's scheme.) In either case it is necessary to separately evaluate the function $E_1(z)$ (for real arguments z), and for this we utilize Algorithm 715 [Cod93]. The evaluation of the necessary values of the erfc functions in the Ewald representations, on the other hand, are reduced, on the basis of the relation

$$\mathrm{erfc}(z) = \mathrm{e}^{-z^2}w(\mathrm{i}z), \quad z \in \mathbb{C} \tag{3.4}$$

to evaluation of the function w, where $w(z)$ is the closely related *Faddeeva* function [DLM17, p. 7.2.3]

$$w(z) = \mathrm{e}^{-z^2}\left(1 + \frac{2\mathrm{i}}{\sqrt{\pi}}\int_0^z e^{t^2}dt\right) \tag{3.5}$$

which is then computed, for the argument iz, by means of Algorithm 916 [ZA11]. (Other related techniques include [AQ11; Wei94], which also rely on the relation (3.4) and first compute $w(iz)$ to obtain the values of erfc(z).) The substitution (3.4) in the case $d_\Lambda = 2$, $d = 3$, for instance, reveals the exponential decaying rate of the Ewald method but, also, the exponential growth for higher-frequencies. Indeed, the $\boldsymbol{m}$-th term in (2.28) equals

$$\mathrm{e}^{\kappa^2/4\eta^2}\mathrm{e}^{-\eta^2\rho_{\boldsymbol{m}}^2}\left[w\left(-\frac{\kappa}{2\eta}+i\eta\rho_{\boldsymbol{m}}\right)+w\left(\frac{\kappa}{2\eta}+i\eta\rho_{\boldsymbol{m}}\right)\right] \tag{3.6}$$

while for (2.29) the corresponding $\boldsymbol{m}$-th term equals

$$\mathrm{e}^{\kappa^2/4\eta^2}\mathrm{e}^{\eta^2 x_d^2}\mathrm{e}^{-|\alpha_{\boldsymbol{m}}|^2/4\eta^2}\left[w\left(\frac{\beta_{\boldsymbol{m}}(\kappa)}{2\eta}-i\eta|x_d|\right)+w\left(\frac{\beta_{\boldsymbol{m}}(\kappa)}{2\eta}+i\eta|x_d|\right)\right]. \tag{3.7}$$

Increasing the user-prescribed parameter $\eta > 0$ improves the convergence rate of the term (2.28) (which is exponentially fast, of the order of $\mathrm{e}^{-\eta^2\rho_{\boldsymbol{m}}^2}$) but it negatively affects the convergence of (2.29) (which is also exponentially fast, but of order $\mathrm{e}^{-\beta_{\boldsymbol{m}}^2/4\eta^2}$). Similarly, decreasing η improves the convergence of the exponential rate of the second terms but it reduces the convergence rate of the first one. Choosing η of order $O(\sqrt{2\pi}/L)$ (where L is the largest period of the bi-dimensional array) the two series will have the same asymptotic convergence rate as $\|\boldsymbol{m}\|_\infty \to \infty$. Doing so, however, causes an exponential growth of the term $\mathrm{e}^{\kappa^2/4\eta^2}$ which is present in both (3.6) and (3.7) as κ or the period grow. Since the sum of (2.28) and (2.29) equals the quasi-periodic Green function, which is a bounded quantity when evaluated away from the lattice points $\boldsymbol{R}_{\boldsymbol{m}}$, cancellation of the two exponentially large quantities must take place, which produces large cancellation errors and consequent instability of the method at high-frequencies or large periods. Such exponential growth can (and usually is) prevented by restricting the term $\kappa/2\eta$ to be less than a maximum threshold; this, however, gives a lower-bound for the parameter η in terms of the wavenumber κ and therefore the term $\mathrm{e}^{\eta^2 x_d^2}$ will grow exponentially fast if the magnitude of the orthogonal projection x_d is moderately large (see Table 3.4). Similar analyses have been conducted in [Are+13; CWJ07; KM00; LBA08] for the cases $d = 2$ and $d_\Lambda = 1$, $d = 3$, demonstrating the aforementioned cancellation errors and the associated *high-frequency breakdown* of the Ewald method. This situation is highly-problematic in the $d_\Lambda = 1$, $d = 3$ case as illustrated in Table 3.5 and analyzed in great detail in [CWJ07]. In that reference the high-accuracy achieved by the Ewald method is demonstrated for configurations where the period equals 0.05λ and 0.5λ and the evaluation points are such that $|\boldsymbol{x}^\perp|$ is a tenth of the period.

Period \ N	2	4	8	16
$4\lambda \times \left(1 + 10^{-2}\right)$	0.99E0	2.56E-4	4.93E-12	5.66E-16
$4\lambda \times \left(1 + 10^{-4}\right)$	1.81E0	6.91E-5	4.80E-12	9.62E-15
$4\lambda \times \left(1 + 10^{-6}\right)$	1.09E0	1.15E-5	8.92E-13	4.24E-16
$4\lambda \times \left(1 + 10^{-8}\right)$	1.38E0	2.71E-5	2.11E-12	1.15E-15
$4\lambda \times \left(1 + 10^{-10}\right)$	1.37E0	2.66E-5	2.07E-12	1.90E-15
$4\lambda \times \left(1 + 10^{-12}\right)$	1.37E0	2.64E-5	2.06E-12	2.90E-16
$4\lambda \times \left(1 + 10^{-14}\right)$	1.37E0	2.64E-5	2.06E-12	1.12E-15
Avg. computing time (s)	2.12E-4	2.39E-4	3.14E-4	5.97E-4

Table 3.3: Accuracy and performance of the Ewald method for a bi-periodic array ($d_\Lambda = 2, d = 3$) as an RW-anomaly is approached. In this configuration, $\boldsymbol{\alpha} = (0, 0, 0)$. The displayed values in this table correspond to the maximum relative error of finite truncations of (2.28) and (2.29) of the form $\|\boldsymbol{m}\|_\infty \leq N$ to compute G_κ^q sampled at 100^2 evaluation points $\boldsymbol{x}_{ij} = (iL/100, jL/100, d/2)$, $i, j = 0 \ldots 99$ in a single period (in all these cases, $|\boldsymbol{x}^\perp| = L/2$). The reference value is computed by means of the spectral series with a very large number of terms to achieve machine-precision (see (3.1)). The times reported correspond to a single evaluation of G_κ^q using the Ewald's method. Clearly, unlike the Laplace-type integral method, the performance of the Ewald method is unaffected by proximity to RW-anomalies. However, the Ewald expressions are undefined at RW configurations.

For a modestly large period (5.5λ), in turn, the errors that contribution presents are only of the order of 10^{-4}-10^{-5}. In fact the errors can be much larger than one, as $|\boldsymbol{x}^\perp|$ slightly increases, in sharp contrast of the errors that the Ewald method can produce in the case $d_\Lambda = d - 1$ for such small periods (Table 3.5). Thus, for the simulation of linear arrays in three-dimensional space the Ewald method, although fast when compared with the Laplace-type integral method, has an erratic behavior making it unsuitable as the basis for a robust and full-spectrum solver.

However, for linear and bi-periodic arrays in two and three-dimensional space respectively and for the problems of low-frequency and small period considered in this thesis the Ewald method provides a very fast computational tool as can be appreciated in Table 3.3; finite truncations of the form $\|\boldsymbol{m}\| \leq N$ of (2.27), (2.28) and (2.29) converge very rapidly amortizing the additional cost associated with the evaluation of special functions even around RW-anomalies.

The shifted Green-function based approach is the simplest of the three methods described in this thesis as it does not require the evaluation of special functions; only finite truncations of the sums over the direct and the reciprocal lattices inherent in

Period \ k/η	0.1	0.25	0.5	1	2	
2.5λ	NaN	0.32E+13	0.77E+3	0.12E-3	0.36E-14	0.33E-14
4.5λ	NaN	0.31E+12	0.14E-1	0.58E-14	0.58E-14	NaN
8.5λ	NaN	0.13E+10	0.57E-14	0.57E-14	NaN	NaN
16.5λ	NaN	0.14E+1	0.40E-14	0.29E-14	NaN	NaN
32.5λ	NaN	0.52E-14	0.48E-14	NaN	NaN	NaN
64.5λ	NaN	0.41E-14	NaN	NaN	NaN	NaN

Period \ k/η	0.01	0.1	0.25	0.5	1	2
2.5λ	NaN	0.34E+13	0.67E+01	0.37E-12	0.33E-14	0.33E-14
4.5λ	NaN	0.17E+12	0.79E-08	0.26E-14	0.26E-14	NaN
8.5λ	NaN	0.42E+06	0.30E-14	0.21E-14	NaN	NaN
16.5λ	NaN	0.12E-13	0.19E-14	NaN	NaN	NaN
32.5λ	NaN	0.29E-14	NaN	NaN	NaN	NaN
64.5λ	NaN	NaN	NaN	NaN	NaN	NaN

Table 3.4: Same experiment as Table 3.3 increasing the period (but taken to avoid an RW-anomaly), varying the values of the splitting parameter η and the value of $|\boldsymbol{x}^{\perp}|$: $0.5L$ (top) and $0.75L$ (bottom). In all cases the sums (2.28) and (2.29) are truncated with $\|\boldsymbol{m}\|_{\infty} < 100$. For various choices of the splitting parameter the Ewald method behaves in an erratic manner and is not able to produce meaningful results for the largest period.

		k/η		
Period (L)	$\lvert\boldsymbol{x}^{\perp}\rvert/L$	$4/5\pi$	π	$4/3\pi$
1.5λ	0.1	0.18E-09	0.30E-07	0.18E-05
	0.5	0.21E-01	0.41E-03	0.33E-05
2.5λ	0.1	0.17E-09	0.67E-08	0.23E-05
	0.5	0.25E+04	0.49E+02	0.76E+00
4.5λ	0.1	0.96E-07	0.29E-07	0.20E-05
	0.5	0.53E+09	0.12E+08	0.21E+06

Table 3.5: Relative errors for the evaluation of G_{κ}^{q} in the $d_{\lambda} = 1$, $d = 3$ case obtained by means of the Ewald method at points for two values of $|\boldsymbol{x}^{\perp}|$. A number of different splitting parameters η are chosen but the method does not yield meaningful results as the magnitude of the orthogonal projection increases.

the two terms in (2.37) are needed. The sum over the direct lattice (and therefore, the complete procedure) inherits the algebraic decay (2.32)–(2.33) of the shifted Green function. Thus either a small or large number of terms is needed in these truncations to achieve an accurate approximation of G_κ^q depending on whether the period is large or small compared to the wavelength (cf. Tables 3.7 and 3.8, respectively). The slow convergence in the small-period case is specially problematic for bi-periodic arrays in three-dimensional space as the computation of the finite truncations have a quadratic cost (the sum must be performed over two directions). However, even for small periods, for arrays with a single direction of periodicity ($d_\Lambda = 1$) the algebraic decay does not pose a major difficulty—which is especially important in the three-dimensional case where the Ewald method is highly unstable and the Laplace-type integral technique is orders of magnitude slower than the shifted Green function method (Tables 3.6 and 3.9). Furthermore, the number of terms needed for the shifted Green function to achieve a given desired accuracy decreases as the period is increased (it is inversely proportional to $L^{-(\frac{j}{2}-1)}$ for j even, with a slightly more negative exponent for j odd); see [BD14; Bru+17] and Table 3.8. Since, additionally, as the computation of the quantities involved are not exponentially large or small, no instabilities as the ones in the Ewald or Laplace-type integral methods occur, making the shifted Green-function based method highly suitable for large-period configurations even in the case $d = 3$, $d_\Lambda = 2$. This regime presents an additional computational challenge, that of dealing with scattering obstacles which are acoustically large and which require a large number of discretization points to resolve the wavelength. In this case, acceleration techniques to reduce the natural operation count of order $O(N_{\text{dis}}^2)$ arising in boundary integral equation methods (where N_{dis} is the number of discretization points) are needed. The contribution [BM18a] already established the applicability of the shifted Green-function together with such acceleration techniques for problems with large periods in two-dimensional space for rough surfaces, even at and around RW-anomalies. The applicability of the method used in that reference to the framework this thesis presents is out of scope and will be left for future work.

3.2 Evaluation of weakly-singular integrals

This section describes numerical methods for evaluation of weakly-singular integrals, necessary for the solvers presented in this thesis. As mentioned in Chapter 4, only smooth surfaces are considered but the general framework which is the subject of this work remains valid for non-smooth domains, provided the associated

Period \ N	64	128	256	512
$4\lambda \times (1 + 10^{-2})$	0.44E-05	0.53E-06	0.66E-07	0.82E-08
$4\lambda \times (1 + 10^{-4})$	0.17E-04	0.39E-05	0.88E-06	0.18E-06
$4\lambda \times (1 + 10^{-6})$	0.79E-05	0.19E-05	0.49E-06	0.12E-06
$4\lambda \times (1 + 10^{-8})$	0.49E-05	0.12E-05	0.30E-06	0.76E-07
$4\lambda \times (1 + 10^{-10})$	0.35E-05	0.87E-06	0.22E-06	0.55E-07
$4\lambda \times (1 + 10^{-12})$	0.28E-05	0.68E-06	0.17E-06	0.43E-07
$4\lambda \times (1 + 10^{-14})$	0.23E-05	0.56E-06	0.14E-06	0.35E-07
Avg. computing time (s)	4.29E-04	5.02E-04	6.51E-04	9.46E-04
Period \ N	64	128	256	512
$4\lambda \times (1 + 10^{-2})$	0.86E-08	0.20E-09	0.82E-11	0.37E-11
$4\lambda \times (1 + 10^{-4})$	0.16E-07	0.76E-09	0.40E-10	0.14E-11
$4\lambda \times (1 + 10^{-6})$	0.73E-08	0.36E-09	0.20E-10	0.73E-11
$4\lambda \times (1 + 10^{-8})$	0.45E-08	0.22E-09	0.13E-10	0.26E-11
$4\lambda \times (1 + 10^{-10})$	0.33E-08	0.16E-09	0.92E-11	0.16E-11
$4\lambda \times (1 + 10^{-12})$	0.25E-08	0.13E-09	0.72E-11	0.53E-12
$4\lambda \times (1 + 10^{-14})$	0.21E-08	0.10E-09	0.59E-11	0.42E-12
Avg. computing time (s)	8.54E-04	9.72E-04	1.24E-03	1.73E-03

Table 3.6: Accuracy and performance of the shifted Green-function (2.37) based method for a linear array in three-dimensional space ($d_\Lambda = 1$, $d = 3$) as an RW-anomaly is approached. In the experiment, G_κ^q is computed for several evaluation points such that, in all cases, $|\boldsymbol{x}^\perp|$ equals half of a period. Highly accurate results are obtained, in contrast with the Ewald method (cf. Table 3.5), in short computing times compared with the also accurate Laplace-type integral method (cf. Table 3.1).

weakly-singular integrals are evaluated accurately. A simple procedure to discretize integral equations, which is the one used to produce the results in this dissertation, is based on use of a set of discretization (also called collocation) points $\boldsymbol{x}_i$ over the domains of the integral operators (namely, the scattering boundaries). These operators are evaluated using the approximate values of the unknown density $\boldsymbol{\Phi}$ at the points $\boldsymbol{x}_i$. Such procedure yields a finite system of equations whose unknowns are approximate values of $\boldsymbol{\Phi}(\boldsymbol{x}_i)$. In the following subsections we make these ideas precise for the two- and three-dimensional cases.

Two-dimensional case

We consider for definiteness the numerical approximation of the single layer operator (4.1) where $\gamma^\sharp$ is a smooth closed curve which can be parametrized by a C^∞

Period \ N	100	200	400	800
$4\lambda \times (1 + 10^{-2})$	2.65E-7	7.83E-8	2.14E-8	4.62E-9
$4\lambda \times (1 + 10^{-4})$	1.74E-6	2.73E-7	4.42E-8	9.14E-9
$4\lambda \times (1 + 10^{-6})$	1.35E-5	2.46E-6	4.38E-7	9.59E-8
$4\lambda \times (1 + 10^{-8})$	9.54E-7	2.19E-7	6.96E-8	1.78E-8
$4\lambda \times (1 + 10^{-10})$	2.47E-7	6.37E-8	2.47E-8	7.94E-9
$4\lambda \times (1 + 10^{-12})$	7.31E-8	2.05E-8	7.60E-9	2.53E-9
$4\lambda \times (1 + 10^{-14})$	2.27E-8	6.51E-9	2.36E-9	7.87E-10
Avg. computing time (s)	2.04E-2	7.21E-2	2.77E-1	1.09E0

Period \ N	100	200	400	800
$4\lambda \times (1 + 10^{-2})$	4.99E-11	1.40E-10	2.76E-10	4.62E-9
$4\lambda \times (1 + 10^{-4})$	1.04E-10	1.64E-10	4.15E-10	9.14E-9
$4\lambda \times (1 + 10^{-6})$	6.37E-10	2.54E-10	4.27E-10	9.59E-8
$4\lambda \times (1 + 10^{-8})$	2.41E-11	2.58E-11	6.24E-11	1.78E-8
$4\lambda \times (1 + 10^{-10})$	6.69E-12	6.66E-12	1.30E-11	7.94E-9
$4\lambda \times (1 + 10^{-12})$	1.65E-12	2.14E-12	5.12E-12	2.53E-9
$4\lambda \times (1 + 10^{-14})$	6.39E-12	1.18E-12	9.00E-13	7.87E-10
Avg. computing time (s)	3.59E-2	1.24E-1	4.75E-1	2.15E0

Table 3.7: Accuracy and performance of the shifted Green-function (2.37) based method for a bi-periodic array as an RW-anomaly is approached. The same numerical experiment as the one carried out for Table 3.3 was conducted considering evaluation points such that $|\boldsymbol{x}^{\perp}|$ equals half of a period. The algorithm parameters are $j = 4$ (top) and $j = 8$ (bottom), $h = 0.25\lambda^{-1}$ and we truncate the sum (2.34) in the form $\|\boldsymbol{m}\|_{\infty} \leq N$. The sum over the reciprocal lattice in (2.37) is truncated with as many terms as taken for the spectral sum used to compute the reference value (fewer terms could be used, but use of the larger number of terms induces only a marginal additional computing cost). Although accurate, the shifted Green function method is significantly more expensive than the Ewald method for the type of small-period configurations considered in this table (cf. Table 3.3).

Period \ N	2	4	8
2.5λ	0.23E+3	0.23E+3	0.23E+3
4.5λ	0.38E+1	0.38E+1	0.49E-1
8.5λ	0.16E+0	0.52E-2	0.13E-6
16.5λ	0.90E-6	0.45E-9	0.18E-10
32.5λ	0.13E-9	0.38E-10	0.73E-10
64.5λ	0.15E-10	0.19E-10	0.29E-10
Max. computing time (s)	1.30E-2	1.32E-2	1.35-2

Period \ N	4	8	16
2.5λ	0.25E+2	0.25E+2	0.40E+0
4.5λ	0.22E+1	0.75E-1	0.27E-3
8.5λ	0.12E+0	0.36E-3	0.15E-4
16.5λ	0.12E-4	0.63E-6	0.66E-7
32.5λ	0.11E-5	0.24E-7	0.31E-8
64.5λ	0.12E-7	0.43E-9	0.56E-10
Max. computing time (s)	6.58E-3	6.68E-3	7.02E-3

Table 3.8: Same experiment as in Table 3.7 but with large periods showing the accuracy of the shifted Green-function method with $j = 4$ (top) and $j = 8$ (bottom). The algebraic decay rate of the shifted Green function produces convergence even when a very small number of periods (N in the table) in the spatial sum in (2.37) are included. The corresponding spectral sum in that equation is truncated according to (3.2) to reach machine-precision; thus, the computational cost increases as the period grows. The reported time corresponds to the maximum computing time measured when the period equals 64.5λ (cf. Table 3.4). Note that, in particular, for the large-period configurations considered in this table, for which, as demonstrated in Table 3.4, the Ewald method breaks down, the shifted Green-function method produces accurate results in short computing time. The large errors observed for the smaller periods can be significantly reduced by increasing the value of N (cf. Table 3.7), albeit at added computing cost.

Period (L) \ N	2	4	8
2.5λ	0.47E-02	0.39E-03	0.37E-04
4.5λ	0.14E-02	0.11E-03	0.94E-05
8.5λ	0.41E-03	0.27E-04	0.21E-05
16.5λ	0.29E-03	0.18E-04	0.13E-05
32.5λ	0.10E-03	0.55E-05	0.33E-06
64.5λ	0.80E-04	0.35E-05	0.18E-06
Max. computing time (s)	3.64E-04	3.73E-04	3.98E-04
Period (L) \ N	8	16	32
2.5λ	0.42E-02	0.72E-04	0.12E-05
4.5λ	0.36E-03	0.53E-05	0.87E-07
8.5λ	0.29E-04	0.36E-06	0.53E-08
16.5λ	0.55E-05	0.63E-07	0.88E-09
32.5λ	0.65E-06	0.58E-08	0.58E-10
64.5λ	0.22E-06	0.13E-08	0.15E-10
Max. computing time (s)	7.28E-04	7.43E-04	7.77E-04

Table 3.9: Same experiment as in Table 3.6 but with large periods showing the accuracy of the shifted Green-function method with $j = 4$ (top) and $j = 8$ (bottom) for the $d_\Lambda = 1$, $d = 3$ case. The points where G_κ^q is evaluated at satisfy $|\boldsymbol{x}^\perp| = L/2$. The algebraic decay rate of the shifted Green function produces convergence even when a very small number of periods (N in the table) in the spatial sum in (2.37) are included. The corresponding spectral sum in that equation is truncated according to (3.2) to reach machine-precision; thus, the computational cost increases as the period grows. The reported time corresponds to the maximum computing time required when the period equals 64.5λ. Note that, in particular, for the configurations considered in this table, for which, as demonstrated in Tables 3.2 and 3.5, the Ewald and Laplace-type intergal methods break down even for modestly large-periods, the shifted Green-function method produces accurate results in short computing time.

2π-periodic function $C(t), t \in [0, 2\pi]$. This example encapsulates the main ideas needed to 1) tackle the evaluation of weakly-singular integrals and 2) obtain linear-systems which discretize boundary integral equations; the analysis can be easily extended to consider double layer potentials and other periodic surfaces whose intersection with the unit cell is not a closed curve. As is well known, the free-space Green function (2.2) for two-dimensional space can be expressed in the form

$$G_\kappa(\boldsymbol{x} - \boldsymbol{y}) = -\frac{1}{2\pi} \log\left(\frac{|\boldsymbol{x} - \boldsymbol{y}|}{2}\right) J_0(\kappa|\boldsymbol{x} - \boldsymbol{y}|) + \mathcal{G}_\kappa(\boldsymbol{x} - \boldsymbol{y}),$$

where $\mathcal{G}_\kappa$ is an analytic function of both spatial variables $\boldsymbol{x}$ and $\boldsymbol{y}$. Letting $\boldsymbol{x} = C(t)$, $\boldsymbol{y} = C(\tau)$, $t, \tau \in [0, 2\pi]$, $\mathcal{S}_\kappa^q[\psi](\boldsymbol{x})$ can be written in the form

$$\int_0^{2\pi} \left[\log\left(\frac{|C(t) - C(\tau)|^2}{4}\right) \tilde{K}_s(t, \tau) + \tilde{K}_r(t, \tau)\right] \psi(C(\tau))|\dot{C}(\tau)| d\tau, \tag{3.8}$$

where $\tilde{K}_s$ and $\tilde{K}_r$ are C^∞ functions (and even analytic if the parametrization C is analytic). As is well-known, the rapid convergence of Fourier series of smooth (or analytic) functions together with the exactness of the trapezoidal rule with $2N_i$ points for trigonometric polynomials of order N_i form the basis of spectral methods; utilization of this quadrature rule to evaluate the regular term of (3.8) yields super-algebraic (resp. exponential) convergence for smooth (resp. analytic) densities ψ and curves C. The logarithmic singularity in (3.8) can be treated by re-expressing the integrand in the form

$$\int_0^{2\pi} \left[\log\left(4\sin^2\left(\frac{t - \tau}{2}\right)\right) K_s(t, \tau) + K_r(t, \tau)\right] \psi(C(\tau))|\dot{C}(\tau)| d\tau, \tag{3.9}$$

where the kernels K_s and K_r are slight modifications of $\tilde{K}_s$ and $\tilde{K}_r$ in (3.8). The introduction of the sin function in the argument of the logarithm makes it possible to utilize the relation [Kre14, Eq. 12.16]

$$\frac{1}{2\pi} \int_0^{2\pi} \log\left(4\sin^2\left(\frac{s}{2}\right)\right) \mathrm{e}^{\mathrm{i}ms} ds = \begin{cases} 0 & m = 0 \\ -\frac{1}{|m|} & m \neq 0 \end{cases}$$

which yields a quadrature rule [CK12, Eq 3.93–3.95] of the form

$$\begin{aligned} &\int_0^{2\pi} \left[\log\left(4\sin^2\left(\frac{t - \tau}{2}\right)\right) K_s(t, \tau) + K_r(t, \tau)\right] d\tau \sim \\ &\sum_{j=0}^{2N_i - 1} \left[R^{N_i}(t) K_s(t, t_j) + \frac{\pi}{N_i} K_r(t, t_j)\right] |\dot{C}(t_j)| \psi(C(t_j)) \end{aligned} \tag{3.10}$$

for logarithmic-type integrals on the basis of the trapezoidal rule nodes $t_j = j\pi/N_i, j = 0 \ldots 2N_i - 1$. This rule converges with super-algebraic order (or exponential order if the domain boundary is analytic). In (3.10) we have used the quadrature weights

$$R_j^{N_i}(t) = -\frac{2\pi}{N_i} \sum_{m=1}^{\frac{1}{m}} \cos m(t - t_j) - \frac{\pi}{N_i^2} \cos N_i(t - t_j). \tag{3.11}$$

The integration nodes $\boldsymbol{x}_i = C(t_i)$ provide the natural choice for collocation in the context of the present Nyström technique. The overall method results in an $N_i \times N_i$ linear system equations which can either be solved by forming and inverting the associated dense matrix, or by means of an iterative linear algebra solver. As can be appreciated from the two-dimensional examples considered in Chapter 5, the overall strategy yields a fast and highly-accurate algorithm.

Three-dimensional case

The evaluation of the weakly-singular integrals over surfaces in three-dimensional space has been an active research area in computational physics. A novel technique put forth in [BG18], which is the backbone of the three-dimensional solvers used in this thesis, is based on use of a partition of a given scattering surface $\mathcal{S}$ into a finite number of non-overlapping patches $\mathcal{P}_i$, each diffeomorphic to the square $[-1, 1]^2$ in the $u - v$ parameter space. In other words, under this scheme each patch is parametrized by a mapping $\boldsymbol{x}_i = \boldsymbol{x}_i(u, v) : [-1, 1]^2 \to \mathcal{P}_i$ (see Figure 3.1). Utilization of Chebyshev points in the square $[-1, 1]^2$ yields 1) spectrally accurate integration rules for smooth functions defined over each patch $\mathcal{P}_i$; 2) straightforward expansion of smooth functions defined in the patch $\mathcal{P}_i$ in terms of Chebyshev polynomials (whose coefficients can be obtained at a cost of $O(N \log N)$ operations); and 3) intrinsic spectral differentiation rules of smooth functions defined in the manifold which are of interest in electromagnetic problems (such as the surface divergence and the surface curl).

The singular integration arising from the corresponding free-space Green function (2.2), whose singularity is of order $1/|\boldsymbol{x} - \boldsymbol{y}|$, in turn, can also be pre-computed on the basis of the aforementioned Chebyshev expansions. Indeed, for a point $\boldsymbol{x}$ lying in the surface or close to it, a weakly-singular (or nearly-singular) integral of the form

$$I(\boldsymbol{x}) = \int_S \frac{H(\boldsymbol{x}, \boldsymbol{y})}{|\boldsymbol{x} - \boldsymbol{y}|} \psi(\boldsymbol{y}) dS(\boldsymbol{y})$$

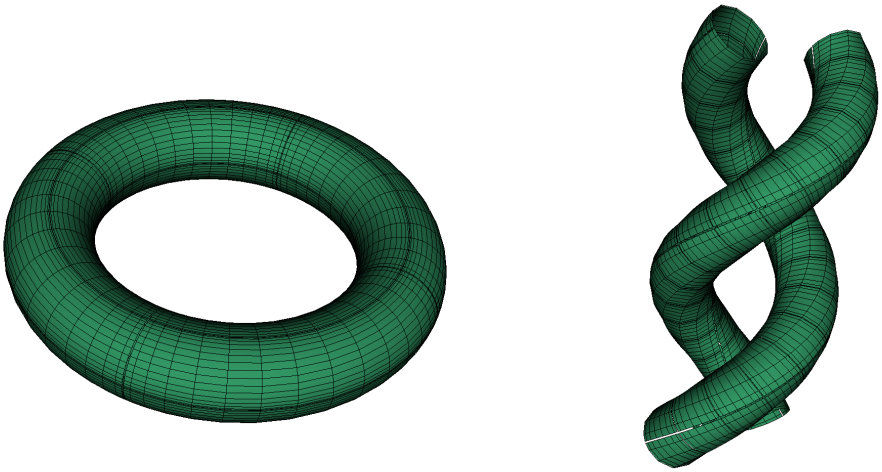

Figure 3.1: Non-overlapping patches on toroidal (left) and "double-helix" (right) scattering surfaces. Each patch shown is obtained by evaluating the respective parametrizations at the set of Chebyshev points adequately translated and scaled from the unit square $[-1, 1]^2$.

can be decomposed as a sum of integrals over each one of the patches in the aforementioned partition of the surface $\mathcal{S}$. Use of the accompanying local parametrizations $\boldsymbol{x}_i$ then yields

$$I(\boldsymbol{x}) = \sum_i \int_{-1}^{1} \int_{-1}^{1} \frac{\tilde{H}_i(u,v)}{|\boldsymbol{x} - \boldsymbol{x}_i(u,v)|} J_i(u,v)\tilde{\psi}_i(u,v)dudv, \tag{3.12}$$

where $J_i(u, v)$ denotes the surface element of $\mathcal{P}_i$ at the point $\boldsymbol{x}_i(u, v)$. Approximating the densities $\tilde{\psi}_i(u, v)$ by truncations of their associated Chebyshev series, each integral in the sum on the right-hand side of (3.12) can be approximated with spectral accuracy by the expression

$$\sum_{n=1}^{N_u} \sum_{m=1}^{N_v} \tilde{\psi}^i_{n,m} \int_{-1}^{1} \int_{-1}^{1} \frac{\tilde{H}_i(u,v)}{|\boldsymbol{x} - \boldsymbol{x}_i(u,v)|} J_i(u,v)T_n(u)T_m(v)dud, \tag{3.13}$$

where $\tilde{\psi}^i_{n,m}$ are the coefficients of the expansion in Chebyshev polynomials of $\tilde{\psi}^i$ and T_j denotes the one-dimensional j-th Chebyshev polynomial. The resulting integrals in (3.13) are now independent of the density and can be obtained as a result of a precomputation which is obtained, in brief, by discretizing the singular integral with a weighted-grid which accumulates discretization nodes around the closest point in $\mathcal{P}_i$ to the evaluation point $\boldsymbol{x}$ by considering one-dimensional change of variables

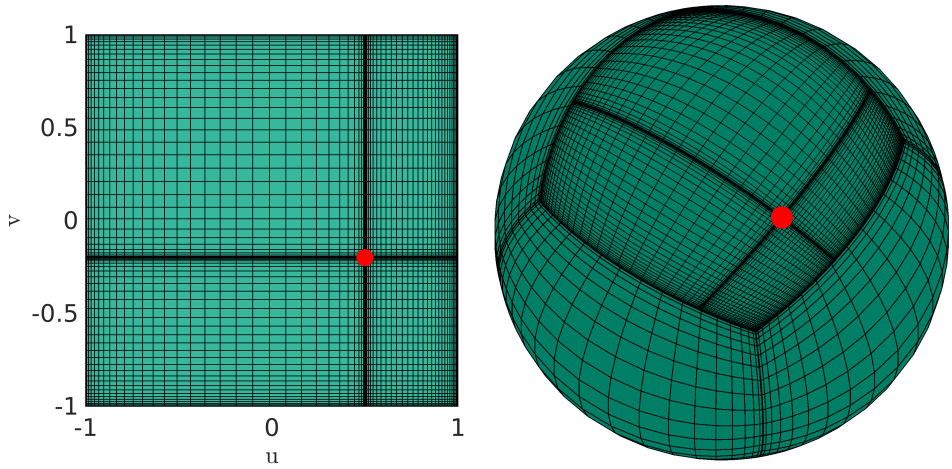

Figure 3.2: Refinement around a singular target point (red dot) for a sphere. Figures reproduced from [BG18], with the authors' permission.

in the integration variables u and v so that the resulting Jacobian vanishes along with some of its derivatives (to a user-prescribed order) cancelling out the weakly-singular integral (see Figure 3.2). This procedure yields high-order, algebraic, convergence dictated by the order of the aforementioned change of variables. A detailed description of this algorithm and its convergence properties can be found in [BG18]. The highly-accurate results in Chapter 5 show the effectiveness of the overall integration technique when used in conjunction with the methods described in Section 3.1 for the evaluation of the quasi-periodic Green function.

Chapter 4

INTEGRAL EQUATION METHODS FOR WAVE-PROPAGATION PROBLEMS IN PERIODIC MEDIA

4.1 BIE formulations

For simplicity, in this contribution attention is restricted to integral solvers for scalar Helmholtz problems in periodic structures with smooth boundaries, but any integral equation methodology (with application to, e.g., open and/or non-smooth surfaces, Maxwell or Elasticity equations, etc.) can be used in conjunction with any of the quasi-periodic Green function methods presented in this paper. All of the examples considered in the present contribution originate from representations of the scattered field u^s in terms of the single- and double-layer potentials

$$\begin{aligned} \mathcal{S}_\kappa^q[\psi](\boldsymbol{x}) &= \int_{\gamma^\#} G_\kappa^q(\boldsymbol{x}-\boldsymbol{y})\psi(\boldsymbol{y})dS(\boldsymbol{y}) \quad \text{and} \\ \mathcal{D}_\kappa^q[\phi](\boldsymbol{x}) &= \int_{\gamma^\#} \frac{\partial G_\kappa^q}{\partial \nu(\boldsymbol{y})}(\boldsymbol{x}-\boldsymbol{y})\phi(\boldsymbol{y})dS(\boldsymbol{y}), \end{aligned} \tag{4.1}$$

for a Λ-periodic surface γ (see Remark 1) which equals either $\Gamma_{j\ell}$ for some $j < \ell$, or relevant portions of $\Gamma_{\mathcal{D}}^{\text{imp}}$, or $\Gamma_{\mathcal{N}}^{\text{imp}}$, respectively. (For example, the integral that represents the field in the domain Ω_0 in Figure 1.4 (left) includes single- and double-layer operators defined on the upper (circular) portions of Γ^{imp}, but it does not include integrals over the component of Γ^{imp} closer to the bottom of the figure.)

As is known, both potentials in (4.1) are solutions of the Helmholtz equation with wavenumber κ for $\boldsymbol{x} \notin \gamma$. We thus assume that the unknown scattered field has been expressed in terms of a boundary integral representation of the form

$$u^s(\boldsymbol{x}) = \mathcal{T}[\boldsymbol{\Phi}](\boldsymbol{x}), \tag{4.2}$$

where

$$\mathcal{T}[\boldsymbol{\Phi}](\boldsymbol{x}) = \mathcal{T}_j[\boldsymbol{\Phi}](\boldsymbol{x}) \quad \text{for} \quad \boldsymbol{x} \in \Omega_j, \tag{4.3}$$

with $\mathcal{T}_j[\boldsymbol{\Phi}](\boldsymbol{x})$ given, for $\boldsymbol{x} \in \Omega_j$, by linear combinations of integral expressions of the form (4.1) involving Green functions corresponding to the domain Ω_j, as suggested above, and as illustrated further below in this section, and where $\boldsymbol{\Phi}$ is either a scalar density, or a vector containing such densities. This procedure reduces

the scattering problem under consideration to a system of integral equations of the form

$$(J+T)[\boldsymbol{\Phi}] = \boldsymbol{F} \tag{4.4}$$

over appropriately chosen Banach spaces X of functions (typically Sobolev spaces [MM00] or Hölder spaces [CK13]), where $T : X \to X$ is a compact operator, and where J either vanishes (in first-kind Fredholm equations) or is an invertible bounded operator (in second-kind Fredholm equations).

Thus, for example, in the case of an impenetrable scattering structure for which $\Omega = \Omega_0$ is a volume having as boundary a periodic surface Γ^{imp}, the fields $u^s = \mathcal{S}^q_{n_0 k}[\varphi]$ and $u^s = \mathcal{D}^q_{n_0 k}[\varphi]$ with $\gamma = \Gamma^{\text{imp}}$ are solutions of the sound-hard or sound-soft scattering problems respectively (with boundary conditions given in (1.16)), provided the density φ satisfies the corresponding boundary integral equations

$$-\frac{1}{2}\varphi(\boldsymbol{x}) + \int\limits_{(\Gamma^{\text{imp}})^{\#}} \frac{\partial G^q_\kappa}{\partial \nu(\boldsymbol{x})}(\boldsymbol{x}-\boldsymbol{y})\varphi(\boldsymbol{y})dS(\boldsymbol{y}) = -\frac{\partial u^{\text{inc}}}{\partial \nu(\boldsymbol{x})}, \quad x \in (\Gamma^{\text{imp}})^{\sharp}, \quad \text{or} \tag{4.5}$$

$$\frac{1}{2}\varphi(\boldsymbol{x}) + \int\limits_{(\Gamma^{\text{imp}})^{\#}} \frac{\partial G^q_\kappa}{\partial \nu(\boldsymbol{y})}(\boldsymbol{x}-\boldsymbol{y})\varphi(\boldsymbol{y})dS(\boldsymbol{y}) = -u^{\text{inc}}(\boldsymbol{x}), \quad x \in (\Gamma^{\text{imp}})^{\sharp}. \tag{4.6}$$

In cases in which periodic arrays of impenetrable scattering particles are included, combined-field formulations are necessary to eliminate internal resonances [CK13]. In these two cases, the boundary potential $\mathcal{T}$ in equation (4.2) is either $\mathcal{S}^q_{n_0 k}$ or $\mathcal{D}^q_{n_0 k}$ whereas J in equation (4.4) are minus or plus a half of the identity operator of the underlying space X and T is either the normal derivative of the single layer potential or the values of the double layer potential at the surface $(\Gamma^{\text{imp}})^{\sharp}$.

In addition to the impenetrable cases mentioned above, a specially well studied case concerns situations in which the refractive index $n(\boldsymbol{x})$ assumes only two values, n_0 and n_1, and there is no impenetrable region (i.e., $\Omega = \mathbb{R}^d$). In such cases the scattered field admits the representation

$$u^{\text{s}}(\boldsymbol{x}) = \begin{cases} \mathcal{D}^q_{n_0 k}\left[\varphi - u^{\text{inc}}\right](\boldsymbol{x}) - \mathcal{S}^q_{n_0 k}\left[\frac{1}{C^2_{01}}\psi - \frac{\partial u^{\text{inc}}}{\partial \nu}\right](\boldsymbol{x}), & \boldsymbol{x} \in \Omega_0 \\ -\mathcal{D}^q_{n_1 k}[\varphi](\boldsymbol{x}) + \mathcal{S}^q_{n_1 k}[\psi](\boldsymbol{x}), & \boldsymbol{x} \in \Omega_1 \end{cases} \tag{4.7}$$

in terms of single- and double-layer potentials, where the densities φ and ψ satisfy the system of integral equations

$$\left(\begin{bmatrix} \text{Id} & 0 \\ 0 & \frac{1+C^{-2}_{01}}{2}\text{Id} \end{bmatrix} - \begin{bmatrix} D^q_0 - D^q_1 & -(C^{-2}_{01}S^q_0 - S^q_1) \\ N^q_0 - N^q_1 & -(C^{-2}_{01}K^q_0 - K^q_1) \end{bmatrix}\right)\begin{bmatrix} \varphi \\ \psi \end{bmatrix} = \begin{bmatrix} u^{\text{inc}} \\ \frac{\partial u^{\text{inc}}}{\partial \nu} \end{bmatrix}, \quad \boldsymbol{x} \in \Gamma^{\sharp}_{01}. \tag{4.8}$$

Here the operators S_j^q, D_j^q are defined as the restriction to the boundary curve $\gamma^\#$ of the single- and double-layer potentials (4.1) with $\gamma = \Gamma_{01}$ and $\kappa = n_j k$ ($j = 0, 1$). The operator N_j^q and K_j^q, in turn, denote the normal derivatives on $\gamma^\#$ of the double-layer potential with and the adjoint of D_j^q (in the sense of [CK13]), respectively, once again, using $\kappa = n_j k$. A comprehensive discussion of the properties and character of these operators can be found in [CK13]. Clearly, in the present case $\mathcal{T}$ in equation (4.2) can be identified with the right-hand side of (4.7), and the quantities and J and T in equation (4.4) equal the first and second square-bracketed terms in (4.8).

As in the three prototypical cases embodied by equations (4.5) through (4.8), for general periodic structures of the type described in Section 1.2, the operator T in equation (4.4) equals a combination of integral operators over the various scattering surfaces Γ_s^{imp}, Γ_h^{imp} and $\Gamma_{j\ell}$ ($1 \le j < \ell \le r+1$). Each one of these operators utilizes either a quasi-periodic or a free-space Green function with an appropriate value of the wavenumber κ, or a combination of quasi-periodic Green functions for two different wavenumbers. Clearly, these integral equation systems are only meaningful provided no Wood anomalies arise in the overall scattering setup. The regularization methodology we propose, which yields integral equation formulations that are valid even at Wood anomalies, is described in the following section.

4.2 A well-conditioned system: WSM regularization

As is well-known [GV96], numerical solutions obtained from ill-conditioned linear systems by Gaussian elimination may contain inaccuracies proportional to the size of the condition number of the underlying linear algebra problem. This ill-conditioning can also increase the number of steps needed by iterative methods to reach convergence to a very small tolerance. The following analysis reveals that the system of integral equations (4.4) is ill-conditioned around RW-anomalies and therefore, even if the integral operators in that equation are approximated with very-high accuracies, its direct inversion may result in loss of accuracy around these singular configurations (Figure 1.3). In this context, the WSM regularization technique proposed in this section represents a very significant contribution of this thesis given that it yields a reformulation of equation (4.4) which does not break down as an anomalous configuration is either approached or reached.

In what follows, given a fixed triple $(k, \boldsymbol{\alpha}, \Lambda)$, which we call a *primitive* triple, we associate to each domain Ω_j a corresponding *derived* triple $(n_j k, \boldsymbol{\alpha}, \Lambda)$. Letting

$(k_w, \boldsymbol{\alpha}_w, \Lambda_w)$ denote a primitive triple for which, for at least one value of j , the corresponding j-th domain derived triple $(n_j k_w, \boldsymbol{\alpha}_w, \Lambda_w)$ is a RW-anomaly, for a given primitive triple $(k, \boldsymbol{\alpha}, \Lambda)$ in the vicinity of $(k_w, \boldsymbol{\alpha}_w, \Lambda_W)$, the Green function expressions (2.3) and (2.4) for the wavenumber $n_j k$ can be expressed in the regular/singular form

$$G^q_{n_j k}(\boldsymbol{x}) = G^{\mathrm{reg}}_{n_j k}(\boldsymbol{x}) + C(d, d_\Lambda) \sum_{\boldsymbol{m} \in \mathcal{W}_j} \mathrm{e}^{i\boldsymbol{\alpha}_{\boldsymbol{m}} \cdot \boldsymbol{x}} f(\beta_{\boldsymbol{m}}(n_j k)), \tag{4.9}$$

where the regular part $G^{\mathrm{reg}}_{n_j k}$ is well defined for $(k, \boldsymbol{\alpha}, \Lambda)$ equal to and in a vicinity of $(k_w, \boldsymbol{\alpha}_w, \Lambda_w)$, and where the second term on the right-hand side contains the singularity that arises as the RW anomaly is approached. In (4.9), the constant $C(d, d_\Lambda)$ equals the pre-factor that multiplies the infinite sums in equations (2.3)–(2.4); the function $f(t)$ is given by $f(t) = 1/t$ for $d_\Lambda = d - 1$, $d = 2, 3$, and $f(t) = 2\mathrm{i}/\pi \log(t/2)$ for $d_\Lambda = 1$, $d = 3$; and $\mathcal{W}_j = \mathcal{W}(n_j k_w, \boldsymbol{\alpha}_w, \Lambda_w)$ (see equation (2.6)).

The expression (4.9) results from the spectral representations (2.3)–(2.4) together with the relations

$$\frac{\mathrm{e}^{\mathrm{i}t}}{t} - \frac{1}{t} \to \mathrm{i} \quad \text{and} \quad H^{(1)}_0(t) - \frac{2\mathrm{i}}{\pi} \log\left(\frac{t}{2}\right) \to \frac{2\mathrm{i}}{\pi} C \quad \text{as} \quad t \to 0, \tag{4.10}$$

where C denotes the Euler-Mascheroni constant, $C = 0.5772156649...$; the finite sum in the right-hand side of (4.9) contains all the terms which give rise to the singular behavior of the quasi-periodic Green function around a RW-anomaly and thus obtain a finite quantity in the limit as the RW anomaly is approached. (Concurrent RW terms occur at an RW anomaly whenever the set $\mathcal{W}_j$ contains more than one element.)

Letting T_{reg} and T_{W} denote the (possibly matrix-valued) integral operators that are obtained by replacing the quasi-periodic Green function(s) $G^q_{n_j k}(\boldsymbol{x} - \boldsymbol{y})$ (for which the derived triple $(n_j k, \boldsymbol{\alpha}, \Lambda)$ is close to an RW-anomaly) and their normal derivatives in the definition of the operator T by the expressions arising from the first and last terms on the right-hand side of equation (4.9), equation (4.4) may be re-expressed in the form

$$(A + T_W)\boldsymbol{\Phi} = \boldsymbol{F}, \quad \text{where} \quad A = J + T_{\mathrm{reg}}. \tag{4.11}$$

The operator T_{W}, in turn, may be expressed in the form

$$T_{\mathrm{W}} = E_{\mathrm{W}} D^{-1} R_{\mathrm{W}}, \tag{4.12}$$

where R_{W} denotes the finite rank integral operator resulting from replacement of $G^q_{n_j k}$ in the definition of T by the kernel

$$\sum_{\boldsymbol{m}\in\mathcal{W}_j} \mathrm{e}^{\mathrm{i}\boldsymbol{\alpha}_{\boldsymbol{m}}\cdot(\boldsymbol{x}-\boldsymbol{y})}, \tag{4.13}$$

where, letting X_{W} denote the (finite-dimensional) image (spanned by a certain finite basis $\{\Phi_{\boldsymbol{m}} : \boldsymbol{m} \in \bigcup_j \mathcal{W}_j\}$) of R_{W}, $D : X_{\mathrm{W}} \to X_{\mathrm{W}}$ is defined over the basis elements $\Phi_{\boldsymbol{m}}$ as

$$D\,\Phi_{\boldsymbol{m}} = \frac{1}{f(\beta_{\boldsymbol{m}}(n_j k))}\Phi_{\boldsymbol{m}}, \quad \boldsymbol{m} \in \mathcal{W}_j \tag{4.14}$$

(and subsequently extended by linearity), and where E_{W} is the inclusion operator of X_{W} into X.

The definitions of the finite-dimensional space X_{W}, its basis $\{\Phi_{\boldsymbol{m}} : \boldsymbol{m} \in \bigcup_j \mathcal{W}_j\}$, and the operator D become apparent as the replacement of the corresponding $G^q_{n_j k}$ by the separable kernel (4.13) is effected. For instance, in the examples discussed in Section 4.1 we have

$$\Phi_{\boldsymbol{m}}(\boldsymbol{x}) = \partial_{\nu(\boldsymbol{x})}\left(e^{\mathrm{i}\boldsymbol{\alpha}_{\boldsymbol{m}}\cdot\boldsymbol{x}}\right), \quad \boldsymbol{x} \in \partial\Omega^\sharp, \quad \boldsymbol{m} \in \mathcal{W}_0 \tag{4.15}$$

for equation (4.5),

$$\Phi_{\boldsymbol{m}}(\boldsymbol{x}) = e^{\mathrm{i}\boldsymbol{\alpha}_{\boldsymbol{m}}\cdot\boldsymbol{x}}, \quad \boldsymbol{x} \in \partial\Omega^\sharp, \quad \boldsymbol{m} \in \mathcal{W}_0 \tag{4.16}$$

for equation (4.6) and

$$\Phi_{\boldsymbol{m}}(\boldsymbol{x}) = \begin{bmatrix} e^{\mathrm{i}\boldsymbol{\alpha}_{\boldsymbol{m}}\cdot\boldsymbol{x}} \\ \partial_{\nu(\boldsymbol{x})}\left(e^{\mathrm{i}\boldsymbol{\alpha}_{\boldsymbol{m}}\cdot\boldsymbol{x}}\right) \end{bmatrix}, \quad \boldsymbol{x} \in \Gamma_{01}, \quad \boldsymbol{m} \in \mathcal{W}_j \tag{4.17}$$

for equation (4.8). In the first two cases, the finite-rank operator R_W assumes the same form, namely

$$R_W[\varphi](\boldsymbol{x}) = C(d, d_\Lambda) \sum_{\boldsymbol{m}\in\mathcal{W}_0} I_{\boldsymbol{m}}[\varphi]\Phi_{\boldsymbol{m}}, \tag{4.18}$$

but the corresponding functionals $I_{\boldsymbol{m}}$ for equations (4.5) and (4.6) are given by

$$I_{\boldsymbol{m}}[\varphi] = \int_{(\Gamma^{\mathrm{imp}})^\sharp} e^{-\mathrm{i}\boldsymbol{\alpha}_{\boldsymbol{m}}\cdot\boldsymbol{y}}\varphi(\boldsymbol{y})dS(\boldsymbol{y}) \quad \text{and} \quad I_{\boldsymbol{m}}[\varphi] = \int_{(\Gamma^{\mathrm{imp}})^\sharp} \partial_{\nu(\boldsymbol{x})}\left(e^{-\mathrm{i}\boldsymbol{\alpha}_{\boldsymbol{m}}\cdot\boldsymbol{y}}\right)\varphi(\boldsymbol{y})dS(\boldsymbol{y}), \tag{4.19}$$

respectively. In the case of the transmission problem (equation (4.8)), in turn, we have

$$R_W[\boldsymbol{\Phi}](\boldsymbol{x}) = C(d, d_\Lambda)\left(\sum_{\boldsymbol{m}\in\mathcal{W}_0} I_{\boldsymbol{m}}[\Phi]\Phi_{\boldsymbol{m}} - \sum_{\boldsymbol{m}\in\mathcal{W}_1} J_{\boldsymbol{m}}[\Phi]\Phi_{\boldsymbol{m}}\right) \tag{4.20}$$

with $\boldsymbol{\Phi} = \begin{bmatrix} \varphi \\ \psi \end{bmatrix}$, where we have set

$$I_{\boldsymbol{m}}[\boldsymbol{\Phi}] = \int\limits_{(\Gamma_{01})^\sharp} \left[\partial_{\nu(\boldsymbol{y})}\left(e^{-\mathrm{i}\boldsymbol{\alpha}_{\boldsymbol{m}}\cdot\boldsymbol{y}}\right)\varphi(\boldsymbol{y}) - e^{-\mathrm{i}\boldsymbol{\alpha}_{\boldsymbol{m}}\cdot\boldsymbol{y}}\psi(\boldsymbol{y})\right] dS(\boldsymbol{y}) \quad \text{and} \tag{4.21}$$

$$J_{\boldsymbol{m}}[\boldsymbol{\Phi}] = \int\limits_{(\Gamma_{01})^\sharp} \left[\partial_{\nu(\boldsymbol{y})}\left(e^{-\mathrm{i}\boldsymbol{\alpha}_{\boldsymbol{m}}\cdot\boldsymbol{y}}\right)\varphi(\boldsymbol{y}) - \frac{1}{C_{01}^2}e^{-\mathrm{i}\boldsymbol{\alpha}_{\boldsymbol{m}}\cdot\boldsymbol{y}}\psi(\boldsymbol{y})\right] dS(\boldsymbol{y}). \tag{4.22}$$

Substitution of (4.12) in (4.11) shows that the original integral equation (4.4) can be expressed in the form

$$(A + E_{\mathrm{W}}D^{-1}R_{\mathrm{W}})\boldsymbol{\Phi} = \boldsymbol{F}. \tag{4.23}$$

The inverse of the operator on the left-hand side can be obtained on the basis of the Woodbury formula

$$(A + E_{\mathrm{W}}D^{-1}R_{\mathrm{W}})^{-1} = A^{-1} - A^{-1}E_{\mathrm{W}}(D + R_{\mathrm{W}}A^{-1}E_{\mathrm{W}})^{-1}R_{\mathrm{W}}A^{-1} \tag{4.24}$$

(see (Remark 3)) provided the operators A and $(D + R_{\mathrm{W}}A^{-1}E_{\mathrm{W}})$ are invertible.

Equation (4.24) is a crucial formula. Assuming that the operator A^{-1} is invertible and well-conditioned:

1. it expresses the inverse operator on the left-hand side in terms of the inverse of the operator A—that only involves the quantities $G^{\mathrm{reg}}_{n_j k}$ (as defined in (4.9)), which are well-defined at and around RW-anomalies;

2. it encapsulates the ill-conditioning of (4.23) at RW-anomalies through the explicit diagonal operator D^{-1} (which blows up as the anomaly is reached) but which only manifests itself on the right hand side of (4.24), through its inverse D (which tends to zero as the anomalous configuration is approached) and

3. its right-hand expression shows that the inverse operator on the left-hand side of that equation actually has a removable singularity at the RW anomaly under consideration, and it provides a useful formula for solution of equation (4.4) at and around $(k_w, \boldsymbol{\alpha}_w, \Lambda_w)$.

The Woodbury formula (4.24) additionally requires the inversion of the operator $D + T_{\mathrm{W}} A^{-1} E_{\mathrm{W}}$. But this inversion problem can easily be translated into a finite-dimensional matrix inversion problem—since this operator is defined over the finite-dimensional space X_W.

A numerical study of the well-conditioning of the WSM methodology as well as its ability to prevent the loss of accuracy observed in Figure 1.3 is included in Section 5.1, demonstrating the value of the framework.

Remark 3. *The Woodbury formula is usually introduced in the context of fast-inversion of matrices; it commonly reads [Pre+07]*

$$(A + UCV)^{-1} = A^{-1} - A^{-1}U(C^{-1} + VA^{-1}U)^{-1}VA^{-1}, \tag{4.25}$$

where $A \in \mathbb{C}^{n\times n}$, $U \in \mathbb{C}^{n\times k}$, $C \in \mathbb{C}^{k\times k}$ and $V \in \mathbb{C}^{k\times n}$ with k usually much smaller than n (the case $k = 1$ is also known as the Sherman-Morrison formula.) But, as equation (4.25) *can be established by mere substitution and algebraic manipulation, the formula is valid for infinite-dimensional operators as well. Briefly, equation* (4.25) *holds for arbitrary operators provided 1) the operator A is invertible, 2) the domains and ranges of the operators U, C and V are such that the composition UCV is well-defined, 3) the operator C is invertible in the space in which it is defined and, finally, 4) the operator $C^{-1} + VA^{-1}U$ is invertible.*

Evaluation of scattering solutions at and around RW-anomalies

As is customary in integral equation methods, once the underlying operator equation is solved, the values of the solution of the PDE problem under consideration can be obtained by means of a post-processing step that proceeds by evaluation of the pertaining boundary potentials, such as (4.2) in the acoustic case, using as surface density the solution $\boldsymbol{\Phi}$ of the integral equation. As mentioned at the beginning of Section 4.1, all solutions of the Helmholtz equation considered in this paper utilize the quasi-periodic Green function (2.1) with various wavenumbers, and their normal derivatives, as kernels of the single and double layer potentials. However, this particular Green function ceases to exist at RW-anomalies and therefore an additional step is needed in the analysis presented in this section to produce quasi-periodic solutions of the Helmholtz at anomalous configurations.

To do this we first use equation (4.9) to produce a decomposition of the potentials in (4.2) into a regular and a singular part,

$$\mathcal{T}_{\mathrm{reg}}\left[\boldsymbol{\Phi}\right] = \mathcal{T}_{\mathrm{reg}}\left[\boldsymbol{\Phi}\right] + \mathcal{T}_{\mathrm{W}}\left[\boldsymbol{\Phi}\right], \tag{4.26}$$

analogous to the decomposition introduced previously for the operator T. For example, in the impenetrable case with either sound-hard or sound-soft boundary conditions, the scattered field is given by a single layer potential or a double layer potential, respectively (see equations (4.5) and (4.6)). After replacement of the quasi-periodic Green function by (4.9) we obtain the representation

$$u^{\mathrm{s}}(\boldsymbol{x}) = \int\limits_{(\Gamma^{\mathrm{imp}})^{\sharp}} G^{\mathrm{reg}}_{n_0 k}(\boldsymbol{x}-\boldsymbol{y})\varphi(\boldsymbol{y})dS(\boldsymbol{y}) + C(d,d_\Lambda)\sum_{\boldsymbol{m}\in\mathcal{W}_0} e^{\mathrm{i}\boldsymbol{\alpha}_{\boldsymbol{m}}\cdot\boldsymbol{x}} f\left(\beta_{\boldsymbol{m}}(n_0 k)\right) I_{\boldsymbol{m}}[\varphi] \tag{4.27}$$

for the single layer case and

$$u^{\mathrm{s}}(\boldsymbol{x}) = \int\limits_{(\Gamma^{\mathrm{imp}})^{\sharp}} \frac{\partial G^{\mathrm{reg}}_{n_0 k}}{\partial \nu(\boldsymbol{y})}(\boldsymbol{x}-\boldsymbol{y})\varphi(\boldsymbol{y})dS(\boldsymbol{y}) + C(d,d_\Lambda)\sum_{\boldsymbol{m}\in\mathcal{W}_0} e^{\mathrm{i}\boldsymbol{\alpha}_{\boldsymbol{m}}\cdot\boldsymbol{x}} f\left(\beta_{\boldsymbol{m}}(n_0 k)\right) I_{\boldsymbol{m}}[\varphi], \tag{4.28}$$

for the double layer case, where the functionals $I_{\boldsymbol{m}}$ are given by equation (4.19) and $\boldsymbol{x}\in\Omega_0$. For the transmission case, in turn, the scattered field is a linear combination of single and double layer potentials (see equation (4.7)) and after replacement of the quasi-periodic Green functions by (4.9) we obtain

$$\begin{aligned} u^{\mathrm{s}}(\boldsymbol{x}) = \int\limits_{\Gamma_{01}^{\sharp}} \frac{\partial G^{\mathrm{reg}}_{n_0 k}}{\partial \nu(\boldsymbol{y})}(\boldsymbol{x}-\boldsymbol{y})\varphi(\boldsymbol{y})dS(\boldsymbol{y}) - \frac{1}{C_{01}^2}\int\limits_{\Gamma_{01}^{\sharp}} G^{\mathrm{reg}}_{n_0 k}(\boldsymbol{x}-\boldsymbol{y})\psi(\boldsymbol{y})dS(\boldsymbol{y}) + \\ C(d,d_\Lambda)\sum_{\boldsymbol{m}\in\mathcal{W}_0} e^{\mathrm{i}\boldsymbol{\alpha}_{\boldsymbol{m}}\cdot\boldsymbol{x}} f\left(\beta_{\boldsymbol{m}}(n_0 k)\right) J_{\boldsymbol{m}}[\varphi], \quad \boldsymbol{x}\in\Omega_0, \end{aligned} \tag{4.29}$$

$$\begin{aligned} u^{\mathrm{s}}(\boldsymbol{x}) = -\int\limits_{\Gamma_{01}^{\sharp}} \frac{\partial G^{\mathrm{reg}}_{n_1 k}}{\partial \nu(\boldsymbol{y})}(\boldsymbol{x}-\boldsymbol{y})\varphi(\boldsymbol{y})dS(\boldsymbol{y}) + \int\limits_{\Gamma_{01}^{\sharp}} G^{\mathrm{reg}}_{n_1 k}(\boldsymbol{x}-\boldsymbol{y})\psi(\boldsymbol{y})dS(\boldsymbol{y}) - \\ C(d,d_\Lambda)\sum_{\boldsymbol{m}\in\mathcal{W}_1} e^{\mathrm{i}\boldsymbol{\alpha}_{\boldsymbol{m}}\cdot\boldsymbol{x}} f\left(\beta_{\boldsymbol{m}}(n_1 k)\right) I_{\boldsymbol{m}}[\varphi], \quad \boldsymbol{x}\in\Omega_1, \end{aligned} \tag{4.30}$$

where $I_{\boldsymbol{m}}$ and $J_{\boldsymbol{m}}$ are given by Equations (4.21) and (4.22). In these examples, either $f(\beta_{\boldsymbol{m}}(n_0 k))$ or $f(\beta_{\boldsymbol{m}}(n_1 k))$ (or both) diverges as the anomalous configuration is approached but, as shown in what follows, all the corresponding products of the diverging $f(\beta_{\boldsymbol{m}}(n_j k))$ by each of the possible functionals are convergent quantities.

Indeed, in the general case (4.2) (and in particular in these three examples), these products are no other than the coordinates of the operator $D^{-1}R_W$ expressed in the corresponding basis $\{\Phi_{\boldsymbol{m}} : \boldsymbol{m}\in\mathcal{W}_j\}$. Thus, in order to evaluate the needed products at or around an RW anomaly, it suffices to compute the quantity $D^{-1}R_{\mathrm{W}}\boldsymbol{\Phi}$, where $\boldsymbol{\Phi}$

is the solution of (4.23) obtained by means of the Woodbury formula (4.24)—either at the near anomalous configuration, or in the limit as the anomaly is reached. To do this we perform the following computation:

$$\begin{aligned} D^{-1}R_{\mathrm{W}}\boldsymbol{\Phi} &= D^{-1}R_{\mathrm{W}}\left(A^{-1} - A^{-1}E_{\mathrm{W}}(D + R_{\mathrm{W}}A^{-1}E_{\mathrm{W}})^{-1}R_{\mathrm{W}}A^{-1}\right)\boldsymbol{F} \\ &= D^{-1}R_{\mathrm{W}}A^{-1}\boldsymbol{F} - D^{-1}R_{\mathrm{W}}A^{-1}E_{\mathrm{W}}(D + R_{\mathrm{W}}A^{-1}E_{\mathrm{W}})^{-1}R_{\mathrm{W}}A^{-1}\boldsymbol{F} \\ &= \left[D^{-1}\left(D + R_{\mathrm{W}}A^{-1}E_{\mathrm{W}}\right) - D^{-1}R_{\mathrm{W}}A^{-1}E_{\mathrm{W}}\right]\left(D + R_{\mathrm{W}}A^{-1}E_{\mathrm{W}}\right)^{-1}R_{\mathrm{W}}A^{-1}\boldsymbol{F} \\ &= \left(D + R_{\mathrm{W}}A^{-1}E_{\mathrm{W}}\right)^{-1}R_{\mathrm{W}}A^{-1}\boldsymbol{F}, \end{aligned} \tag{4.31}$$

where the only slightly non-trivial step, namely, the third equality, is established by factoring out the term $(D + R_{\mathrm{W}}A^{-1}E_{\mathrm{W}})^{-1}R_{\mathrm{W}}A^{-1}\boldsymbol{F}$ from the right. Note that, as in (4.24), the inverse of the sum on the last line in (4.31) can be obtained by solving a finite-dimensional linear system of equations. Since the last line in this equation tends to a finite limit as the RW configuration is approached, the coordinates of $D^{-1}R_{\mathrm{W}}\boldsymbol{\Phi}$ can be continuously extended in the RW-anomaly limit. Thus, the spatial values of the solution of the PDE under consideration can be continuously extended to the anomalous configuration $(k_w, \boldsymbol{\alpha_w}, \Lambda_w)$ considered in the present section.

Chapter 5

NUMERICAL RESULTS

This chapter presents a variety of numerical experiments showing the applicability and performance of the methodology proposed in this thesis to obtain solutions at RW-anomalies as well as non-anomalous configurations on the basis of all three Green function evaluation techniques: the Laplace, Ewald and shifted Green function methods. The two-dimensional examples included in this work (Section 5.2) consist of arrays of penetrable and impenetrable particles whereas in the more challenging bi-periodic three-dimensional case (Section 5.3) we also consider arrays of impenetrable particles as well as bi-periodic reflective and transmissive gratings. Finally, in the case $d_\Lambda = 1$, $d = 3$, the solvers are demonstrated with the simulation of acoustical wave-scattering by impenetrable double-helical periodic structures (Section 5.4).

All simulations were obtained with a Fortran-90 implementation of the numerical solvers and the various figures were rendered with the visualization software VisIt [Chi+12] using the SILO file format. The two-dimensional simulations were executed in a single core of an Intel i5-8250U processor in a personal computer with 16 Gb of RAM memory while the solvers for the different three-dimensional examples were run in 24 cores of an Intel(R) Xeon(R) CPU E5-2670 v3 processor in a single node of a computing cluster with 120 Gb of RAM memory; in this latter case, the parallelization of the evaluation of the quasi-periodic Green function as well as the pre-computations needed for the rectangular integration technique were programmed using the OpenMP API. The linear systems in the two-dimensional case were solved by Gaussian elimination using the LAPACK implementation provided in the Intel Math Kernel Library; in the three-dimensional examples, in turn, the solutions were obtained using the CERFACS implementation of the GMRES algorithm [Fra+97] (in these cases we have reported the number of iterations required to achieve a residual tolerance of 10^{-12} .)

Throughout this chapter the overall solver error is estimated by means of the energy balance criterion described in Appendix A. In the case $d_\Lambda = d - 1$, we also perform a convergence analysis on the Rayleigh coefficient A_0^+ (present in all the cases considered in what follows): the relative error is evaluated via comparison

with the corresponding value obtained using the finest discretization with the largest truncation parameter.

Remark 4. *The necessary parameters required for the various quasi-periodic Green function evaluation methods were selected as follows. The shift parameter and numbers of shifts used for the shifted Green function (which is employed in Sections 5.1 and 5.4) are* $h = \lambda/2$ *and* $j = 8$*. The splitting parameter in the Ewald method (which is employed in Sections 5.1, 5.2 and 5.3) was selected as* $\eta = k$*. The Laplace-type integral method (which is utilized in Section 5.1) only requires a selection of the number of quadrature points; a number of 128 quadrature points was used in all cases.*

5.1 Condition number analysis around RW-anomalies

Figure 5.1 depicts the first scattering setup considered in this chapter, namely, a plane wave illuminating a two-dimensional periodic array, of period $L = 5\lambda$, of impenetrable sound-soft cylindrical obstacles. The individual sound-soft scatterers have circular cross-section with diameter equal to half a period, and the simulations carried out for this geometry contemplate angles close to normal incidence which, for the chosen period, is an RW anomalous configuration.

As stated in Chapter 1, the application of integral equation methods to periodic media normally present two main types of difficulties around RW-anomalies. The most dramatic challenge concerns inaccuracies in the evaluation of the quasi-periodic Green function—which result in an inaccurate construction of the linear system to be inverted. The second challenge relates to the ill-conditioning of the system around RW-anomalies, which might also produce a loss of accuracy even if very accurate evaluations of G_κ^q are used, such as those arising from the Ewald or shifted Green function methods (Tables 3.3 and 3.7). The first of these difficulties is illustrated in Figure 5.2, which displays the error in the energy balance criterion (Appendix A) in a case in which the quasi-periodic Green function is computed by means of the Laplace-type integral method using equations (2.12) and (2.13)—in which the singular $1/\beta_m$ term has not explicitly been extracted—and by means of equations (2.12), (2.16) and (2.22)—which include singularity extraction. Figure 5.3 displays results of two similar experiments, in both cases using singularity extraction, except that, in this case, the Ewald and shifted Green function representations are used to compute G_κ^q. These figures illustrate the benefits resulting from use of hybrid spatial/spectral representations with singularity extraction to produce

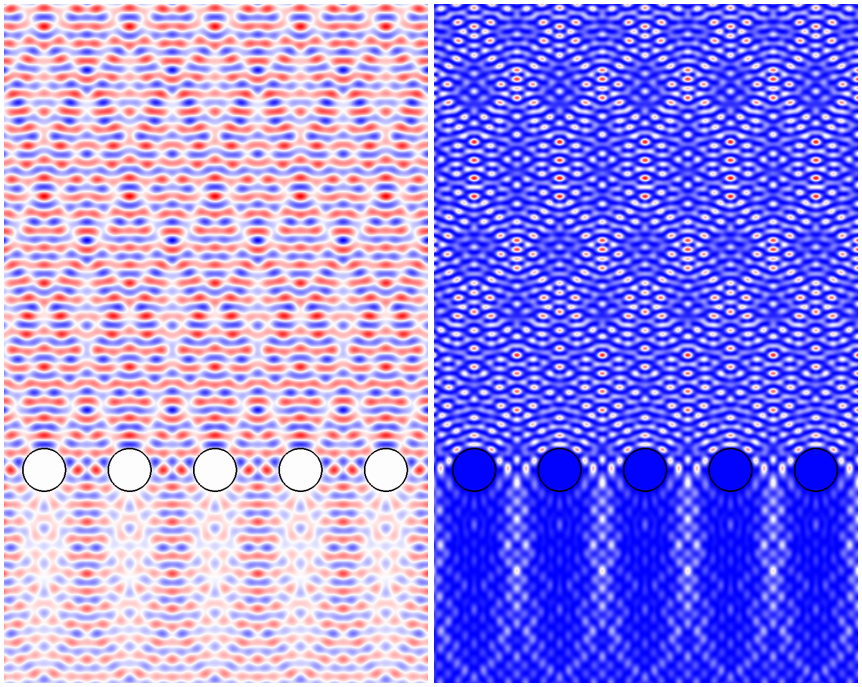

Figure 5.1: Real part (left) and intensity pattern (right) for the total field u scattered under normal incidence by a periodic array of impenetrable sound soft two-dimensional obstacles with circular cross section.

highly-accurate results around the singularity—irrespectively of the use of the WSM formalism.

Difficulties related to system ill-conditioning around RW-anomalies, in turn, only emerge as high-accuracies are sought. As explained in Chapter 4, ill conditioning arises in these cases from the diagonal operator D^{-1} in equation (4.23), which blows up as the RW singularity is approached. In the two-dimensional example considered in the present section, D^{-1} diverges with an order $O(1/\sqrt{\Delta\theta})$ as $\Delta\theta \to 0$ resulting in matrices whose condition numbers only increase up to figures of order 10^8 in double precision arithmetic (Figure 5.5). Given that these values are not exceedingly large, a severe loss of accuracy is not evidenced (only a few digits are lost). However, the WSM regularization technique produces linear systems which are well-conditioned (at least for all the runs of the solvers and all the experiments presented in this thesis, see Figure 5.5) yielding a methodology which preserves the accuracy of the underlying method to evaluate G_κ^q and which can extend the solution to the RW-anomaly itself (Figure 5.4).

In what follows we demonstrate the validity and applicability of the proposed framework for a number of relevant examples.

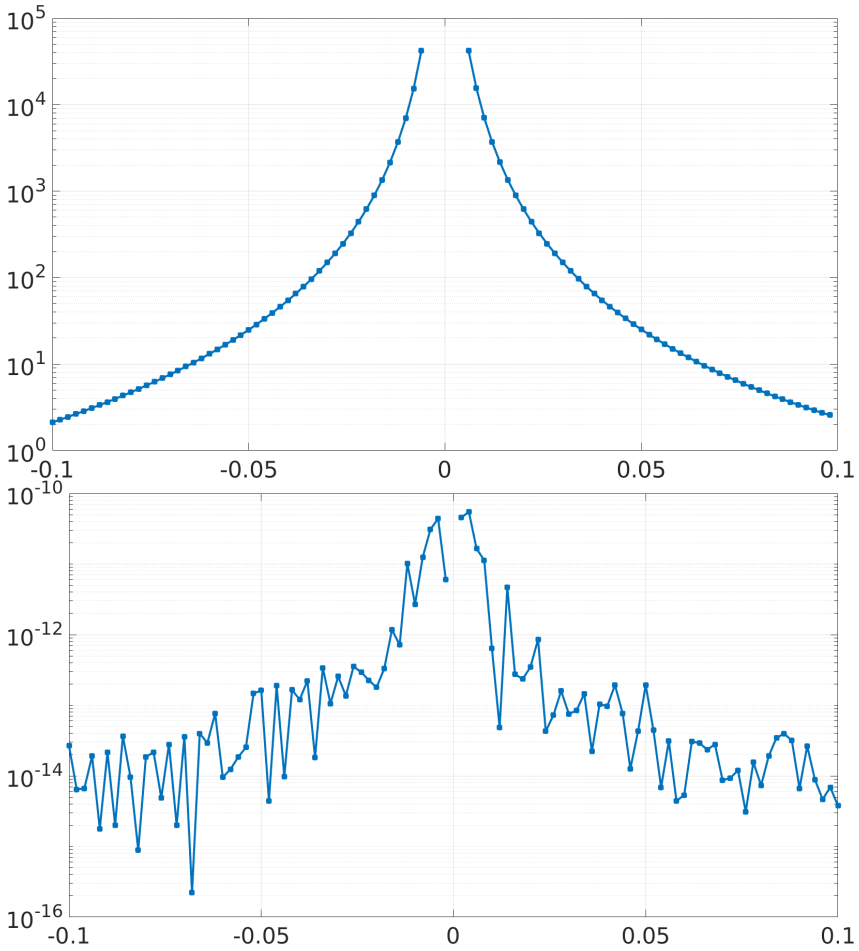

Figure 5.2: Errors estimated by the energy balance criterion, for scattering solvers based on the Laplace integral method, that compute inaccurately (top) and accurately (bottom) the quasi-periodic Green function around a RW-anomaly. The angles $\theta = \delta^5$ sample incidence directions which differ from normal incidence in angles of the order of 10^{-5} to 10^{-14}.

5.2 Two-dimensional simulations

The second two-dimensional example we consider in this thesis is the scattering by a periodic array with period equal to four exterior wavelengths (4λ) formed by three obstacles: a rotated kite-shaped particle whose boundary is parametrized by

$$C(t) = \lambda(0.65\cos(2t) - 0.65, 1.5\sin(t)) \quad t \in [0, 2\pi],$$

a tilted ellipse, with major and minor semi-axes equal to 2λ and λ respectively, and a circle of radius λ (Figure 5.6). The infinite propagation medium has refractive index $n_0 = 1$ and the particles have refractive indexes equal to $n_1 = 1.5$, $n_2 = 2.5$ and $n_3 = 3.5$, respectively, and are assumed to model sound-hard materials (the

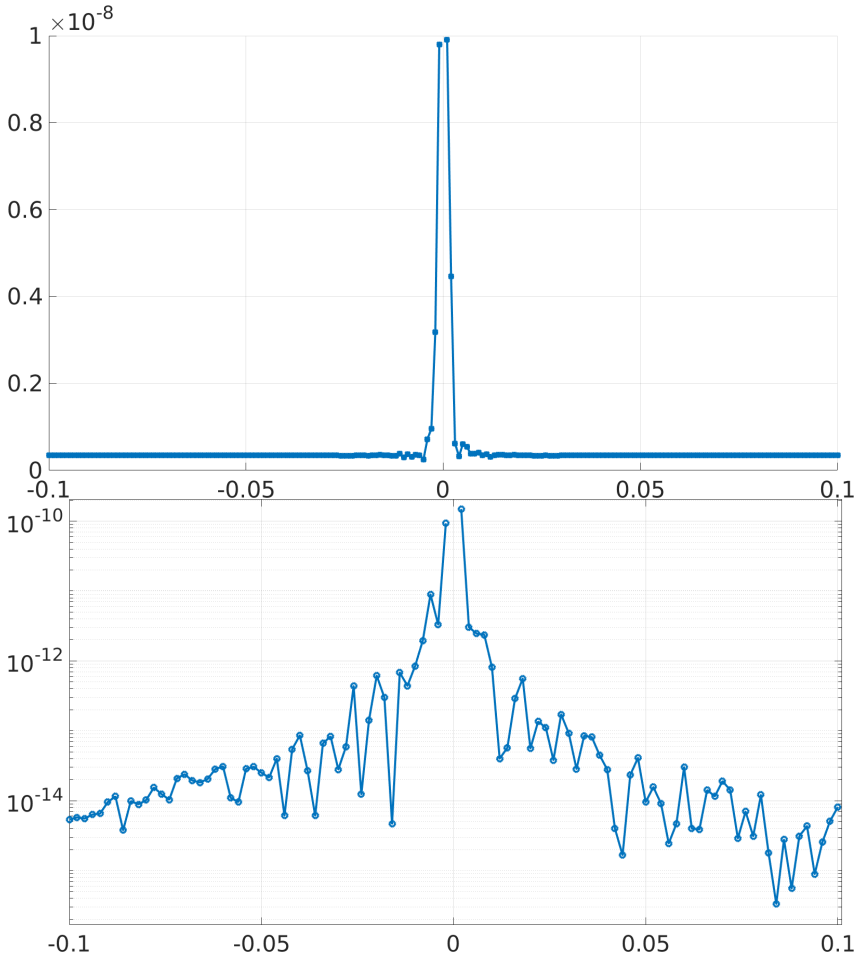

Figure 5.3: Energy balance errors for two scattering solvers that do not utilize the proposed WSM formalism around RW-anomalies, and which rely on the shifted Green function with $j = 8$ (top) and the Ewald method (bottom). The angles $\theta = \delta^5$ sample incidence directions which differ from normal incidence in angles of the order of 10^{-5} to 10^{-14}.

corresponding constants $C_{j\ell}$ in (1.17) are thus $1/n_\ell$, $\ell = 1, \ldots, 3$.). The structure is illuminated by a plane-wave with normal incidence giving rise to an anomalous configuration where $\beta_m = 0$ for $m = \pm 4$. Table 5.1 shows the effectiveness of the proposed framework to treat RW-anomalies achieving spectral order of convergence and fast-simulations with high-accuracies; Figure 5.6, in turn, illustrates the real part of the total field in the region where the scattering process takes place and also the diffraction pattern observed in the same area.

The final two-dimensional numerical experiments considered in this section illustrates the robustness of the overall methodology. Two arrays with periods 5λ and 10λ of impenetrable sound-soft particles are illuminated with a whole range of

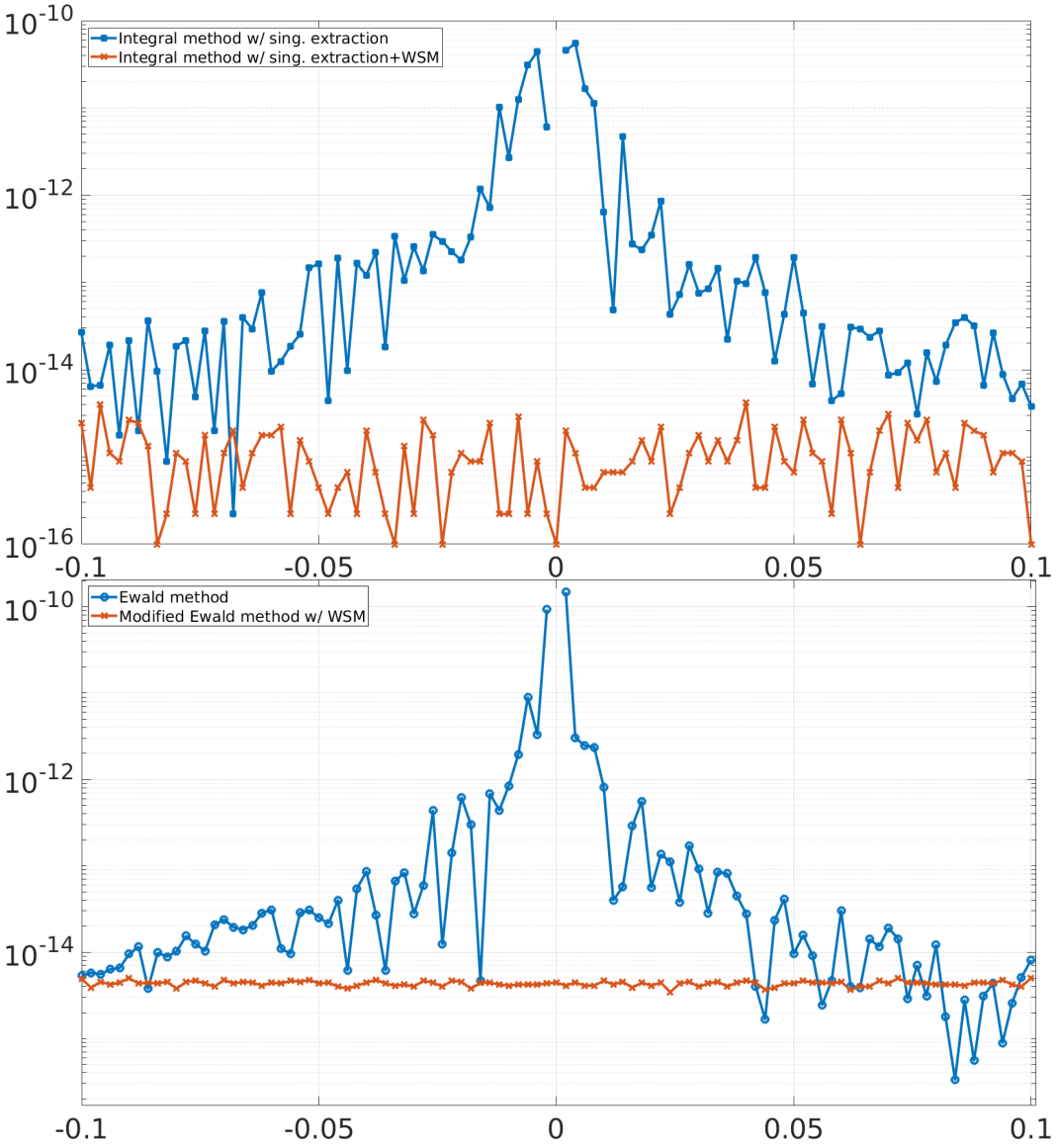

Figure 5.4: Energy balance errors in the solution of the scattering problem depicted in Figure 5.1 on the basis of the Laplace-type integral method with singularity extraction, as proposed in this thesis (top, cf. Figure 5.2), and Ewald methods (bottom), with and without WSM regularization. The angles $\theta = \delta^5$ sample incidence directions which differ from normal incidence in angles of the order of 10^{-5} to 10^{-14}.

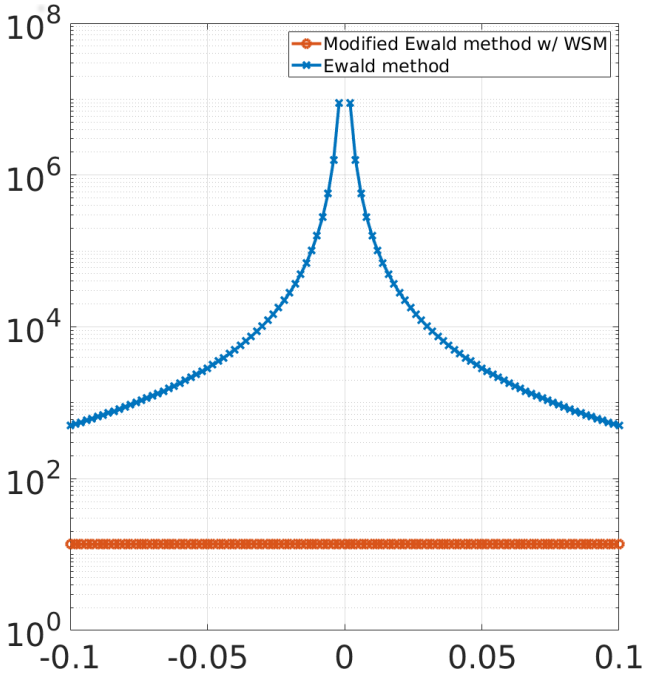

Figure 5.5: Condition number in the simulation of the scattering problem depicted in Figure 5.1 using the Laplace-type integral method (with singularity extraction) and the Ewald representation with and without the WSM regularization. (For this configuration the two Green function methods produce the necessary Green-function values with errors of the order of machine precision). The angles $\theta = \delta^5$ sample incidence directions which differ from normal incidence in angles of the order of 10^{-5} to 10^{-14}.

incidence angles sampling anomalous and non-anomalous configurations. In both cases 64 points are used to discretize each ellipse (Figure 5.8) and each series in the Ewald representation is truncated with $|m| < 40$. As can be clearly appreciated from the errors displayed in Figure 5.7, the overall accuracy of the methodology does not suffer at and around RW-anomalies. Scattering patterns for a particular incidence angle are displayed in Figure 5.8.

5.3 Three-dimensional simulations–Bi-periodic structures

The first numerical example considered in this section is the scattering of an incoming plane wave by a periodic array of impenetrable sound-soft tori (Figure 5.9). The results displayed in Tables 5.2 and 5.3 correspond to a lattice whose periodicity vectors are $\boldsymbol{\nu_1} = L(1, 0, 0)$ and $\boldsymbol{\nu_2} = L(\cos(\pi/3), \sin(\pi/3), 0)$ (a honeycomb structure) where the size of the period equals $L = \lambda$ and $L = 4\lambda$ respectively. The wave impinges on the array with a propagation direction equal to

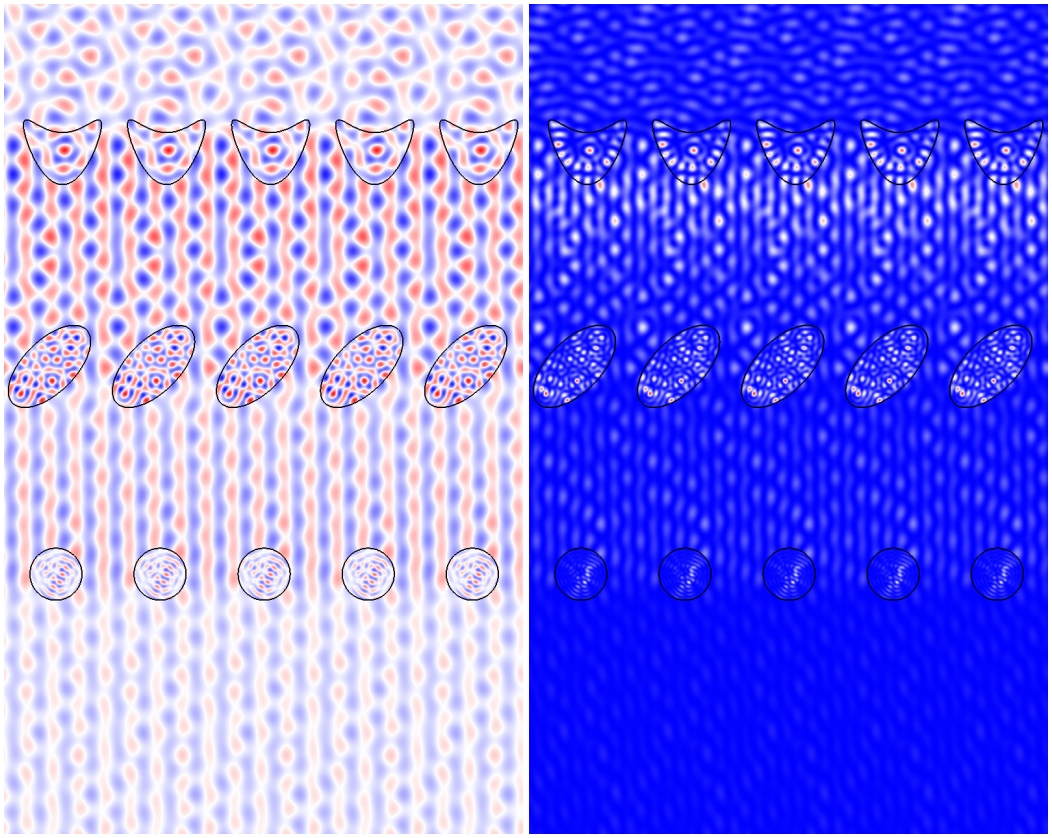

Figure 5.6: Real part (left) and intensity pattern (right) of the total field u scattered under normal incidence by a periodic array containing three types of penetrable obstacles (kite (top), tilted ellipse (center) and circle (bottom)) with refractive indexes of 1.5, 2.5 and 3.5 respectively (the refractive index of the infinite propagation domain equals 1). Each obstacle has an approximate diameter of one exterior wavelength (λ) and the period equals 4λ, yielding an RW-anomalous configuration: for $m = \pm 4$ we have $\beta_m = 0$.

$$(\cos(\phi)\sin(\theta), \sin(\phi)\sin(\theta), -\cos(\theta)) \tag{5.1}$$

with $\phi = \pi/3$ and $\theta = \pi/6$ giving rise to an anomalous configuration in the example with largest period ($L = 4\lambda$). We use a global parametrization of the torus

$$\boldsymbol{x}(s,t) = (\cos(\pi s)(r\cos(\pi t) + R), \sin(\pi s)(r\cos(\pi t) + R), r\sin(\pi t)), \quad (s,t) \in [-1,1]^2$$

setting in both cases $R = L/4$ and $r = L/16$. Non-overlapping patches can be obtained by means of dyadic subdivisions of the square $[-1,1]^2$ and a proper re-scaling. High-order convergence can be appreciated from the displayed errors (Tables 5.2 and 5.3) as the discretization of the surface is refined (where the refinement is controlled with the number of patches and with the number of Chebyshev nodes in the

N_{dis}	N_{tr}	EBC	A_0^+	Time (s)
96	5	0.24E+0	0.10E-02	0.32
	10	0.96E-3	0.76E-04	0.42
	20	0.81E-4	0.34E-04	0.64
	40	0.80E-4	0.34E-04	1.06
128	5	0.24E+0	0.10E-02	0.58
	10	0.93E-3	0.10E-03	0.77
	20	0.74E-6	0.13E-06	1.14
	40	0.44E-8	0.25E-09	1.90
160	5	0.24E+0	0.10E-02	0.94
	10	0.93E-3	0.11E-03	1.24
	20	0.74E-6	0.13E-06	1.82
	40	0.98E-10	Ref	3.00

Table 5.1: Energy balance error and computing times for the simulation of the scattering setup illustrated in Figure 5.6 at an RW anomalous configuration. These results were obtained by means of the framework proposed in this thesis, in this case on the basis of the modified Ewald summation method and the spectral series. Each obstacle is discretized by means of N_{dis} nodes and both series in the Ewald summation method are truncated at $|m| \leq N_{\text{tr}}$; see also Remark 4.

u and v direction) as well as increasing the number of terms in the truncation of the series in the Ewald representation.

The second experiment conducted to test the robustness of the method around RW-anomalies resembles the one performed to produce Figures 5.7. We consider an impenetrable sound-soft crossed grating (that is, a grating for which the lattice directions lie at 90° from each other), whose boundary is parametrized by

$$\boldsymbol{x}(s,t) = \left(\frac{L}{2}s, \frac{L}{2}t, \frac{H}{2}\sin(\pi s)\sin(\pi t)\right), \quad (s,t) \in [-1,1]^2, \tag{5.2}$$

with period and height given by $L = 5\lambda$ and $H = \lambda$, and we compute the energy balance error for a range of 10,000 incidence directions (5.1) where the sample angles are given by $\theta_i = \arccos(i\pi/100)$, $\phi_j = 2\pi j/100$, $i, j = 0 \ldots 99$. The unit-cell of the grating is divided in four non-overlapping patches (obtained from a single dyadic splitting of the parameter square $[-1,1]^2$ and a re-scaling of the parameters) and each is discretized with 16×16 Chebyshev grid points. The evaluation of the quasi-periodic Green function is performed by means of Ewald method truncating each of the required series with $\|\boldsymbol{m}\|_\infty < 20$. It can be clearly appreciated from Figure 5.10 that high-accuracies are obtained irrespectively of the occurrence of RW-anomalies (Figure 2.1).

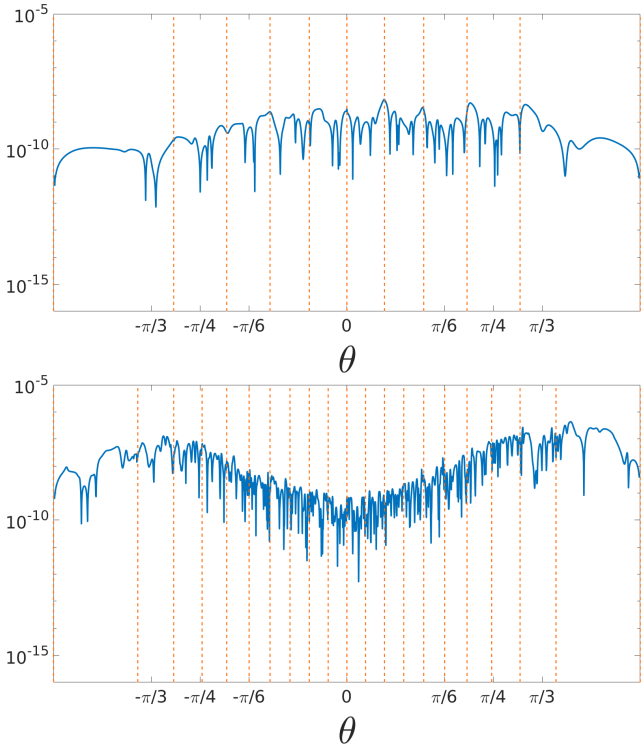

Figure 5.7: Energy balance error as a function of the incidence angle for the scattering configurations depicted in Figure 5.8. The Ewald method with WSM regularization is used in all cases. The top and bottom graphs correspond to the arrays with period equal to 5λ and 10λ respectively.

Finally we consider the convergence properties of the methodology for a transmission grating. In this case, the propagation domain $\Omega = \mathbb{R}^3$ having two subregions with constant refractive indexes $n_0 = 1$ and $n_1 = 1.25$ (Figure 5.11); the boundary between the two is parametrized by the mapping (5.2) where the period $L = 2\lambda_0$ (two wavelengths of the domain with refractive index $n_0 = 1$). Under normal incidence, this configuration gives rise to RW-anomalies in both domains (there are, in each set, 4 indexes $\boldsymbol{m}$ such that $\beta_{\boldsymbol{m}}(n_j k) = 0$, $j = 0, 1$). As can be clearly appreciated in Table 5.4, very high accuracies are obtained for the finest discretization and results with a few number of correct digits can be obtained in a few seconds.

5.4 Linear periodic arrays in three-dimensional space

This section illustrates the applicability of the ideas developed in this thesis to the simulation of three-dimensional periodic structures with a single direction of periodicity. In order to obtain highly-accurate evaluations of G_κ^q we utilize the shifted Green function representation (2.36) which yields highly accurate results in fast

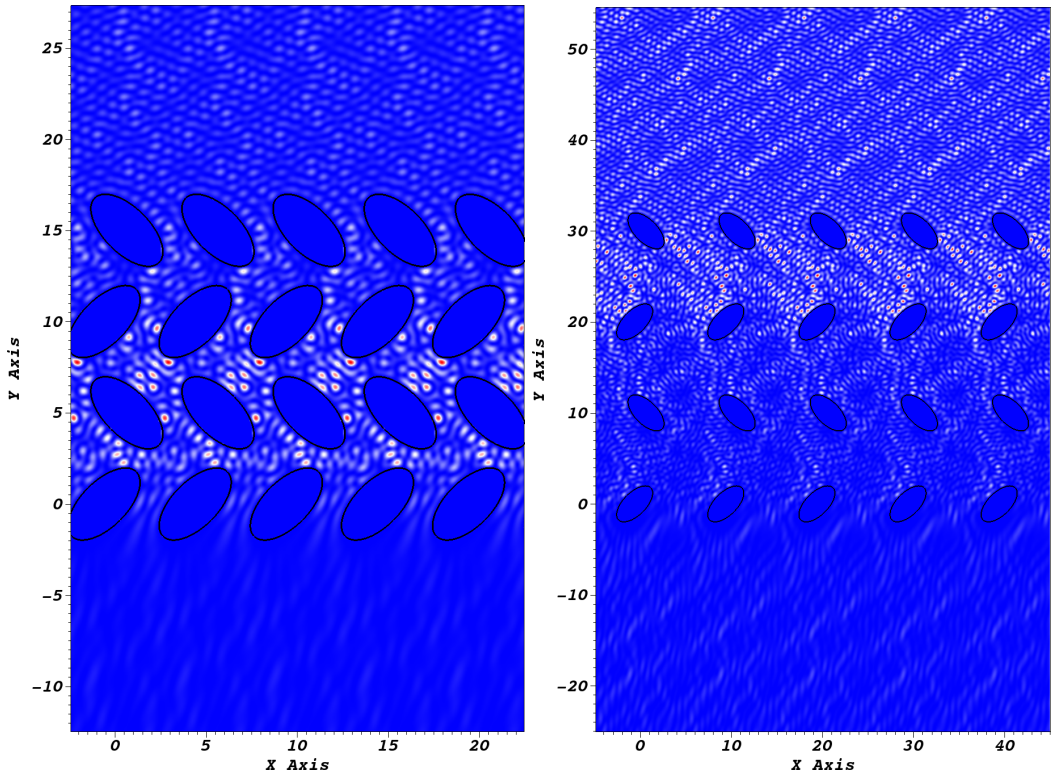

Figure 5.8: Diffraction pattern (total field) that results as a plane wave with an incidence angle of 30° impinges on a four-layer array of impenetrable ellipses with periods equal to 5λ (left) and 10λ (right). In both cases the ellipses have major and minor semi-axes equal to 2.5λ and 1.25λ.

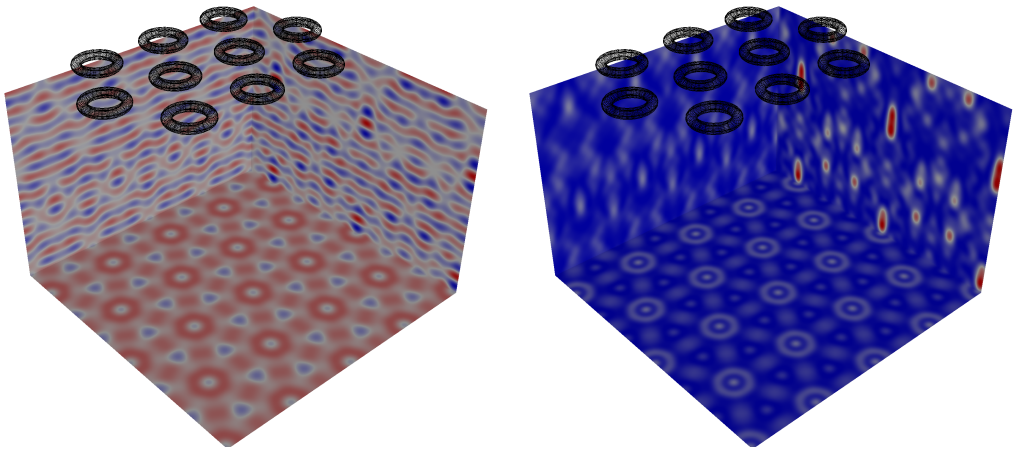

Figure 5.9: Real part (left) and intensity (right) of the total field that results as a plane-wave impinges upon an array of impenetrable tori arranged in a honey-comb lattice structure of period equal to 4λ in each one of the two lattice directions.

Patches	$N_u \times N_v$	N_{dis}	N_{tr}	EBC	A_0^+	Iterations	Time (s)
1	8×8	64	5	0.6309E-02	0.47E-02	18	<1
		64	10	0.6314E-02	0.47E-02	16	<1
		64	20	0.6314E-02	0.47E-02	16	<1
	16×16	128	5	0.8058E-05	0.4405E-05	20	2
		128	10	0.7052E-05	0.4807E-05	18	3
		128	20	0.7052E-05	0.4807E-05	18	3
	32×32	1024	5	0.1863E-05	0.9206E-06	17	9
		1024	10	0.8408E-07	0.4880E-07	16	15
		1024	20	0.8408E-07	0.4880E-07	16	38
4	8×8	256	5	0.1525E-04	0.2038E-04	18	<1
		256	10	0.1376E-04	0.2190E-04	16	<1
		256	20	0.1376E-04	0.2190E-04	16	3
	16×16	1024	5	0.1873E-05	0.9257E-06	15	7
		1024	10	0.7330E-07	0.4720E-07	14	13
		1024	20	0.7330E-07	0.4720E-07	14	36
	32×32	4096	5	0.1946E-05	0.9572E-06	15	103
		4096	10	0.9999E-09	0.0000E+00	14	198
		4096	20	0.9999E-09	Ref	14	568

Table 5.2: Convergence analysis for a periodic array of impenetrable tori arranged in a honeycomb structure with period equal to λ and for an incidence field for which the configuration is away from RW-anomalies. The quasi-periodic Green function is evaluated by means of the Ewald method where each infinite sum in the Ewald representation is truncated with $\|\boldsymbol{m}\|_\infty \leq N_{\text{tr}}$. See also Remark 4.

computing times, in contrast to the Ewald method which has an erratic behavior (Table 3.5) and does not present a major advantage in terms of speed as in the bi-periodic case analyzed in the previous section. The Laplace-type integral method was not used either since it becomes costly due to the evaluation of Bessel functions with complex argument. Perhaps, in part, for these reasons, these type of configurations have received much less attention in the computational physics literature than their well-known bi-periodic relatives. Only approximate models [Nor+15] and finite-differences in time-domain (FDTD) simulations were produced [Wil+09] to compute the eigenmodes of twisted waveguides. The contributions [BM18b; LZT13; TL10] consider linear arrays of spheres but also concentrate on the study of guided modes in the periodic structure rather than the simulation of a wave-scattering process. To the best of our knowledge, the numerical simulations presented in what follows are the very first high-order numerical simulations ever produced for linear arrays in three-dimensional space.

Patches	$N_u \times N_v$	N_{dis}	N_{tr}	EBC	A_0^+	Iterations	Time (s)
1	8×8	64	10	0.2595E+00	6.0971E-02	31	<1
		64	20	0.2545E+00	5.9180E-02	30	<1
		64	40	0.2545E+00	5.9168E-02	29	<1
	16×16	128	10	0.2425E-01	2.6792E-02	36	2
		128	20	0.2488E-01	2.5300E-02	35	3
		128	40	0.2488E-01	2.5299E-02	33	9
	32×32	1024	10	0.4450E-03	7.8421E-04	39	17
		1024	20	0.2128E-04	1.9235E-05	37	40
		1024	40	0.2234E-04	1.9456E-05	35	133
4	8×8	256	10	0.1563E-01	8.7905E-03	32	2
		256	20	0.1792E-01	9.7342E-03	31	3
		256	40	0.1792E-01	9.7348E-03	29	9
	16×16	1024	10	0.5682E-03	1.1452E-03	32	18
		1024	20	0.5851E-04	8.4642E-05	29	42
		1024	40	0.5687E-04	8.5112E-05	28	133
	32×32	4096	10	0.3621E-03	3.7297E-04	29	268
		4096	20	0.1414E-05	7.9210E-07	26	638
		4096	40	0.1806E-07	Ref	24	2105

Table 5.3: Convergence analysis for a periodic array of impenetrable tori arranged in a honeycomb structure with period equal to 4λ and for an incidence field that gives rise to a RW anomaly—which is treated here by means of the WSM method. Truncations of the form $\|\boldsymbol{m}\|_\infty \leq N_{\text{tr}}$ were used for the WSM-modified Ewald summation method to obtain the highly accurate results displayed; see also Remark 4.

We consider first the scattering of an impenetrable, sound-soft, double-helical structure comprised of two "twisted" cylinders (Figure 5.12) and compute the energy balance error for several discretization levels and a number of finite truncations of the shifted Green function representation (2.36).

Each infinite helix is obtained from an appropriate rotation around the x_1-axis of the globally-parametrized surface

$$\boldsymbol{x}(s,t) = C(s) + r\cos(t)\hat{\boldsymbol{e}}_{\boldsymbol{2}}(s) + r\sin(t)\hat{\boldsymbol{e}}_{\boldsymbol{3}}(s), \quad s \in \mathbb{R}, t \in [0, 2\pi], \tag{5.3}$$

where $C(s) = (R\sigma s, R\cos(s), R\sin(s))$ is a parametrization of a helical curve with radius R and slope σ, where r is the inner-radius of the twisted cylinder and $\hat{\boldsymbol{e}}_{\boldsymbol{2}}$ and $\hat{\boldsymbol{e}}_{\boldsymbol{3}}$ are the normal and bi-normal unit vectors of the Frenet reference frame of C. The subdivision into patches required by the rectangular integration methodology can be obtained by means of dyadic subdivisions of $[-1, 1]^2$ and proper rescalings. For the

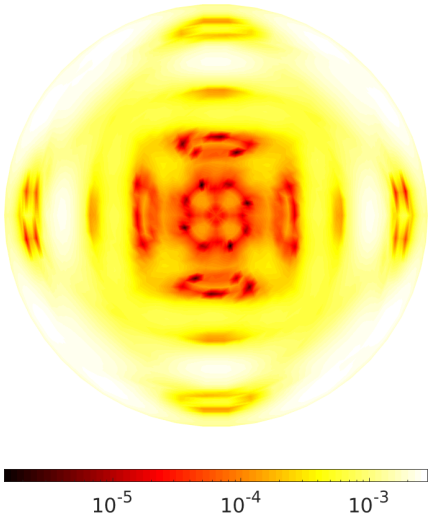

Figure 5.10: Energy balance error for a periodic crossed-grating with period equal to 5λ as a function of the incidence direction. The unit-cell of the grating is divided in four non-overlapping patches (obtained from a single dyadic splitting of the parameter square $[-1, 1]^2$ and a re-scaling of the parameters) and each is discretized with 16×16 Chebyshev grid points. The evaluation of the quasi-periodic Green function is performed by means of Ewald method truncating each of the required series with $\|\boldsymbol{m}\|_\infty < 20$; see also Remark 4.

examples considered in Tables 5.5 and 5.6 we have set in equation (5.3) $r = \lambda/2$ and $R = \lambda$. The slope, in turn, is $\sigma = 5\lambda/2\pi R$ yielding a period equal to 5λ. In both cases the incident wave has a propagation direction given by equation (5.1) with $\phi = 0$ and $\theta = \pi/6$ for Table 5.5 (a non-anomalous configuration) and $\theta = 10^{-8}$ (very close to an RW-anomaly) for Table 5.6. The results displayed in those tables demonstrate the excellent convergence properties of the shifted Green function in conjunction with the rectangular integration method away from and around RW-anomalies.

The final numerical experiment considered in this thesis concerns the diffraction of a normally incident plane-wave by a linear array of spheres distributed along two helical curves. The geometrical and acoustical parameters are taken so as to reproduce the results obtained by Rosalind Franklin and Raymond Gosling [FG53] in their famous crystallography experiment (Figure 5.14, right) which lead to the determination of the double-helical structure of DNA molecules. The normally-incident incoming wave has a wavelength equal to $0.154nm$ while each helix has 10 impenetrable spheres of radius $0.195nm$ modelling the phosphorus atom, the largest in the DNA molecule (Figure 5.13). Additionally, both the helical curves where the spheres are centered have diameter and period equal to $2nm$ and $3.4nm$, respectively,

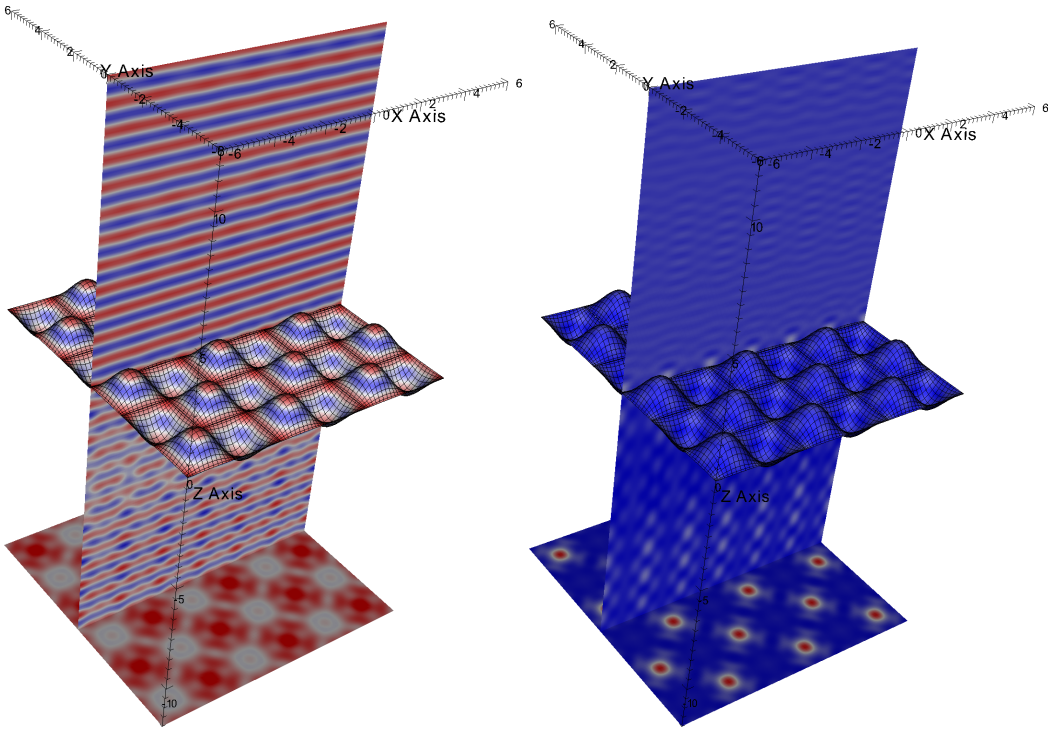

Figure 5.11: Real part (left) and intensity (right) of the total field produced as a plane-wave impinges upon a transmission grating with period equal to 2λ in both x_1 and x_2 directions under normal incidence. The boundary between the two constant refractive index domains is parametrized by $(x_1, x_2, \sin(\pi x_1/2)\sin(\pi x_2/2))$. The upper and lower media have refractive indexes equal to 1 and 1.5, respectively. This setup gives rise to RW-anomalies in both domains.

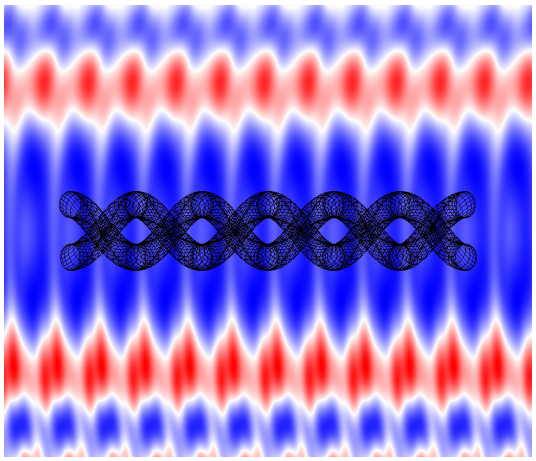

Figure 5.12: Twisted double-helical structure of period 5λ illuminate with a plane wave with incidence direction given by (5.1) where $\phi = 0$ and $\theta = \pi/6$. The intensity pattern of the total field is displayed in a plane parallel to the periodicity direction located behind the double helix, 50 wavelengths away from the structure.

Patches	$N_u \times N_v$	N_{dis}	N_{tr}	EBC	A_0^+	Iterations	Time (s)
1	8×8	64	10	0.8255E+00	9.8145e-02	44	<1
		64	20	0.8322E+00	9.8587e-02	44	<1
		64	40	0.8322E+00	9.8586e-02	44	1
	16×16	128	10	0.1112E-01	0.23947E-02	36	2
		128	20	0.1074E-01	0.23674E-02	36	5
		128	40	0.1074E-01	0.23673E-02	36	16
	32×32	1024	10	0.1839E-04	0.1957E-05	34	26
		1024	20	0.2118E-06	0.9429E-06	34	74
		1024	40	0.2136E-06	0.9426E-06	40	255
4	8×8	256	10	0.3886E-02	0.98145E-03	32	2
		256	20	0.2486E-02	0.98587E-03	35	5
		256	40	0.2486E-02	0.98586E-03	33	9
	16×16	1024	5	0.3220E-04	0.98325E-05	32	32
		1024	10	0.4003E-05	0.14548E-05	32	80
		1024	20	0.3992E-05	0.14554E-05	32	255
	32×32	4096	5	0.2018E-03	0.2018E-03	30	212
		4096	10	0.2783E-09	1.2845E-09	19	720
		4096	20	0.2710E-09	Ref	19	1164

Table 5.4: Convergence analysis for a transmission crossed-grating with period equal to 2λ under normal incidence (an RW anomalous configuration). Truncations of the form $\|\boldsymbol{m}\|_\infty \leq N_{\text{tr}}$ of the modified Ewald summation method are used to obtain highly accurate results; see also Remark 4.

Patches	$N_u \times N_v$	N_{dis}	N_{tr}	EBC	Iterations	Time (s)
1	16×16	256	2	0.2564E+00	42	1.69
		256	4	0.2373E+00	41	1.78
		256	8	0.2372E+00	41	1.84
4	16×16	1024	2	0.1414E-01	44	26.52
		1024	4	0.1348E-03	42	27.31
		1024	8	0.5230E-05	40	28.88
16	16×16	4096	2	0.1416E-01	44	423.36
		4096	4	0.1361E-03	42	442.48
		4096	8	0.3881E-05	40	462.56

Table 5.5: Convergence analysis for a double-helix structure (Figure 5.12) of period 5λ. The incidence direction is given by (5.1) with $\phi = 0$ and $\theta = \pi/6$ (not an RW-anomaly). The quasi-periodic Green function is evaluated by means of truncations of the shifted Green function representation 2.36 with $j = 8$ and $h = \lambda/2$. In this table, the sum over the spatial lattice in (2.36) (G_j^q in Equation (2.34)) is truncated with $|m| \leq N_{\text{tr}}$ terms; see also Remark 4.

Patches	$N_u \times N_v$	N_{dis}	N_{tr}	EBC	Iterations	Time (s)
1	16×16	256	2	0.4397E-01	40	1.70
		256	4	0.4104E-01	40	1.78
		256	8	0.4100E-01	40	1.84
4	16×16	1024	2	0.4366E-02	39	26.17
		1024	4	0.2232E-04	39	27.14
		1024	8	0.1049E-04	39	28.45
16	16×16	4096	2	0.4411E-02	39	424.73
		4096	4	0.1152E-04	39	441.23
		4096	8	0.6991E-06	39	461.32

Table 5.6: Convergence analysis for a double-helix structure (Figure 5.12) of period 5λ. The incidence direction is given by (5.1) where $\phi = 0$ and $\theta = 10^{-8}$, very close to an RW-anomaly (which occurs at $\theta = 0$). The quasi-periodic Green function is evaluated by means of truncations of the shifted Green function representation 2.36 with $j = 8$ and $h = \lambda/2$. In this table, the sum over the spatial lattice in (2.36) (G_j^q, Equation (2.34)) is truncated with $|m| \leq N_{\text{tr}}$ terms; see also Remark 4.

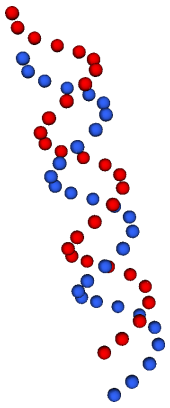

Figure 5.13: Double helix of spherical particles .

and they are mutually displaced by $3/8$ of the period along the periodicity direction. This last parameter was crucial in the original experiment as it allowed to conclude from the absence of the fourth diffraction order that the structure consists of just two displaced helices (in contrast to other models proposed by Linus Pauling which considered the possibility of a third helix). To produce the simulation run to compute the far-field displayed on the left of Figure 5.14, each sphere is splitted into 6 non-overlapping patches each of which is discretized with a Chebyshev grid of 8×8 points and the shifted Green function is truncated with $|m| < 10$. Even though the physical processes that govern acoustical wave-scattering and X-Ray

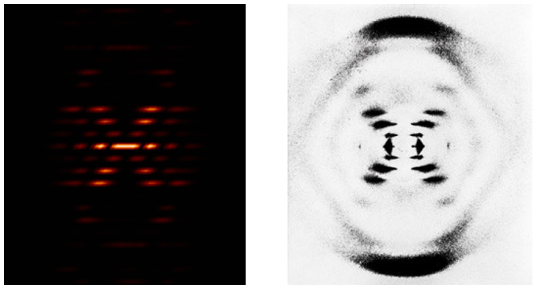

Figure 5.14: Simulated diffraction pattern by a double-helical array of sound-soft impenetrable spheres obtained by means of the shifted Green function method depicted in 5.13 (left) and X-Ray diffraction pattern by DNA in its hydrated B-form (right, well known as the "Photo 51" image, copyright: King's College London). The quasi-periodic Green function is evaluated by means of truncations of the shifted Green function representation (2.36) with $j = 8$ and $h = \lambda/2$. Note the mismatch between theoretical and experimental images at the center of the diffraction pattern: the right-hand experimental data does not contain the bright central line that is clearly visible on the left-hand image. This is a feature of the experimental setup, which used a filter to occlude the intense line to avoid overexposure of the X-Ray photographic film.

diffraction are different, the simulated diffraction pattern resembles remarkably well the one obtained experimentally, including the "missing" fourth-order resulting from the destructive interference caused by the relative displacement of the helices (Figure 5.14).

Chapter 6

CONCLUSIONS

This dissertation has analyzed the major challenges encountered by classical methods based on quasi-periodic Green functions in the simulation of wave-scattering by periodic media around a set of anomalous configurations, the RW-anomalies, which are observed in both two- and three-dimensional problems, and which are pervasive in the most challenging three-dimensional case. Through the concept of hybrid spatial/spectral representations, this contribution introduced a framework, the Woodbury-Sherman-Morrison methodology, to understand and bypass the problems presented by these singularities irrespectively of the underlying geometry of the scattering structure. As a result, fast and robust numerical solvers were obtained and applied to the simulation of acoustic wave-scattering by various two and three-dimensional periodic structures with a variety of boundary conditions. The errors and times presented in this contribution render the software developed for this thesis among the most accurate and fastest available to date.

Limitations and future work

Even though the problem of wave-scattering by periodic media has a rich history with many influential contributions and applications by prominent figures of modern science, many interesting research avenues open up from this dissertation.

Firstly, as can be observed in this work (Tables 5.2–5.6), a major limitation in boundary integral equations (BIE) methods is the non-sparsity of the linear systems they produce. Even though BIE methods require the discretization of surfaces (and not volumes), the slow decay of the free-space Green function demands the consideration of the interaction of *each* pair of discretization points resulting in a quadratic complexity in time and space if no additional acceleration procedures are employed. To address this difficulty, an equivalent-sources acceleration technique [BM18a] has been successfully employed for two-dimensional periodic problems to reduce the quadratic operation count using the shifted quasi-periodic Green function. In this context, its adaptation and application to the general treatment put forth in this contribution represents an exciting opportunity for future work as it will enable the treatment of problems with large periods where the scatterer spans the whole unit-cell, which is the prevailing situation in remote sensing applications where the

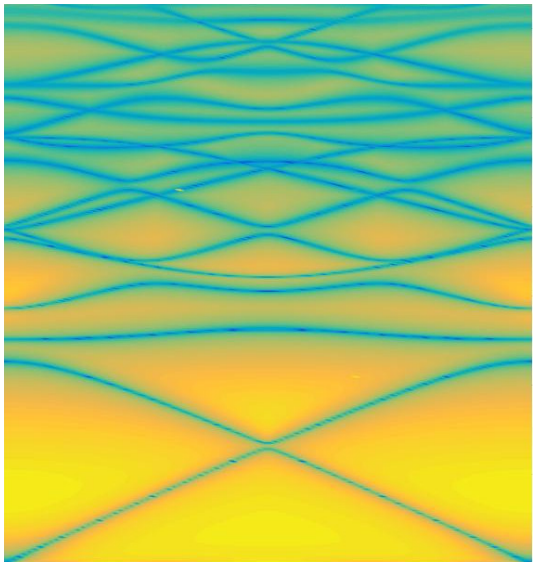

Figure 6.1: Band-structure of a two-dimensional array of circles with transmission boundary conditions. The horizontal axis corresponds to the values of the magnitude of $\boldsymbol{\alpha}$ (which is taken parallel to the x_1-axis). For each pair $(|\boldsymbol{\alpha}|, k)$ we discretize the integral equations for the transmission case (4.8) and compute the smallest singular value (in logarithmic scale) of the resulting matrix. The blue lines indicate the existence of a non-trivial null-space of the integral equation, related to the presence of a resonant mode. The corresponding quasi-periodic Green function is computed by means of the Ewald-method and the WSM methodology is not used (explaining certain defects in the figure where RW-anomalies occur).

surface of the ocean or rough terrains are modeled with a periodizing scheme (in order to eliminate edge effects).

Secondly, a related problem to the ones considered in this thesis is the computation of resonant modes for a periodic structure in which the propagation domain is periodic along each direction of space, i.e., $d_\Lambda = d$. In this case, since the Laplacian is a self-adjoint operator and the PDE problem is posed in a bounded domain (due to the periodicity in all directions of space), for a fixed value of $\boldsymbol{\alpha}$ there will exist a discrete set of parameters k_j (accumulating at infinity) for which there exist a non-trivial solution (an $\boldsymbol{\alpha}$-quasi-periodic eigenmode of the Laplace operator). Varying the value of $\boldsymbol{\alpha}$, a continuous curve of wavenumbers k_j is obtained for which there exist a non-trivial solution of the Helmholtz equation with homogeneous boundary conditions, i.e., a "resonant mode"; computing these lines is known as the problem of determining the band-structure of the crystal (Figure 6.1). While some BIE methods have been applied successfully in related two-dimensional eigenvalue

problems where quasi-periodicity was not considered [A+17], the extension of the ideas put forth in that contribution together with the framework developed in this thesis represents a promising direction for future work. Specifically, since the singularity of the quasi-periodic Green function for the case $d_\Lambda = d$ behaves with an order $O(1/\beta_{\boldsymbol{m}}^2)$ [Lin10, Eq. 2.8], the problem in the conditioning of the linear system around RW-anomalies analyzed in this work becomes more salient than in the cases considered here ($d_\lambda < d$), rendering the WSM methodology a promising tool to tackle this problem.

Lastly, from a theoretical standpoint, the validity of the WSM methodology hinges on the invertibility of the regularized operator A in equation (4.23). While conducting the research that underlies this thesis, it was found that the existence of A^{-1} is closely linked with the establishment of conditions for the uniqueness of solution of the underlying PDE. At this point, this connection is not reflected in the present work as the latter problem constitutes a mathematical challenge that has been scarcely explored in the context of periodic problems and exceeds the scope of this thesis.

Hopefully, this work will enable further progress in the field of optics and computational electromagnetism and, also, in the theory of partial differential equations.

Appendix A

ENERGY BALANCE CRITERION

The principle of conservation of energy provides, under certain circumstances, a valuable indicator of the accuracy of a numerical methods for periodic structures. Even though the exact (or highly-accurate) verification of a conservation principle does not guarantee in general the convergence of the method, it provides a good estimator of the overall accuracy of the algorithm, specially when accompanied by other criteria, such as resolution analysis. In the wave-scattering by periodic (non-absorbing) media the relevant conservation principle follows from Green's second identity [PC90]. Since the corresponding conservation principle varies depending on the geometrical setup of the underlying scattering problem, we derive in what follows the energy balance criterion for the problems considered in Chapter 5.

A.1 Scattering by particles, $d_\Lambda = d - 1$.

In this configuration we assume that a unit period of the complement of the propagation domain Ω_0 which, for definiteness, we call D_0, is formed by the union of finitely many disjoint bounded obstacles, filled with either a penetrable (non-absorbing) or an impenetrable material. If either Dirichlet, Neumann or transmission conditions are prescribed in ∂D_0, the total field u satisfies

$$\int_{\partial D_0} \left(\overline{u} \frac{\partial u}{\partial \nu} - u \frac{\partial \overline{u}}{\partial \nu} \right) dS = 0. \tag{A.1}$$

Let $M > 0$ such that $D_0 \subset \{\boldsymbol{x} \in \mathbb{R}^d : |x_d| < M\}$ and assume, for definiteness, that D_0 is fully contained inside the volume $\Omega_M = \left\{ \sum_{i=1}^{d_\Lambda} s_i \boldsymbol{v}_i + s\hat{\boldsymbol{x}_d} : 0 \le s_i \le 1, |s| < M \right\}$; such assumption can be dropped by joining the top and bottom faces of this volume with one (if $d = 2$) or two (if $d = 3$) pairs of, possibly curved parallel faces which do not intersect D_0 and where each surface in the pair is a translation by $\boldsymbol{v_i}$ of the other (see Figure A.1). A direct application of Green's second identity in the domain $\Omega_M \setminus D_0$ shows that

$$\int_{\partial D_0} \left(\overline{u} \frac{\partial u}{\partial \nu} - u \frac{\partial \overline{u}}{\partial \nu} \right) dS = \int_{\{|x_d| = M\}^\sharp} \left(\overline{u} \frac{\partial u}{\partial \nu} - u \frac{\partial \overline{u}}{\partial \nu} \right) dS. \tag{A.2}$$

Writing $u = u^{\mathrm{s}} + u^{\mathrm{inc}}$ (equations (1.12)–(1.13)), expressing u^{s} by its corresponding Rayleigh series in the regions $x_d > M$ and $x_d < -M$ (equation (1.24)) and using

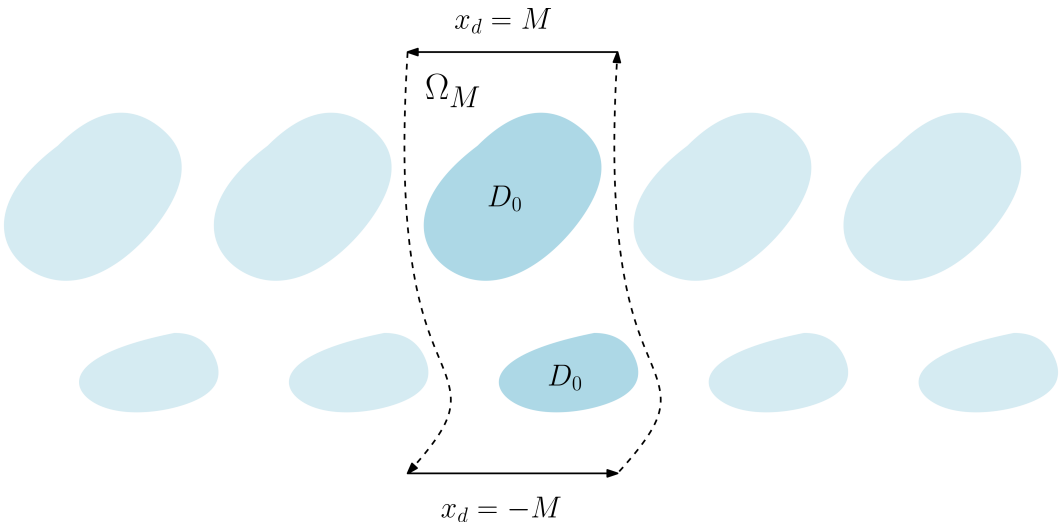

Figure A.1: Unit period of the complement of the propagation domain Ω_0 (D_0) and integration domain Ω_M where Green's second identity is applied. The integrals along the parallel surfaces that joins the top and bottom flat boundaries cancel out due to the periodicity.

the orthogonality of $e^{i\boldsymbol{\alpha_m}\cdot\boldsymbol{x}}$, $\boldsymbol{m} \in \mathbb{Z}^{d_\Lambda}$ with respect to the standard L^2 inner-product, it can be shown that

$$\frac{1}{\mathcal{A}} \int_{\{|x_d|=M\}^\sharp} \overline{u}\frac{\partial u}{\partial \nu} dS = \mathrm{i} \sum_{\boldsymbol{m}\in\mathbb{Z}^{d_\Lambda}} \beta_{\boldsymbol{m}}(n_0 k) \left(|A^+_{\boldsymbol{m}}|^2 + |A^-_{\boldsymbol{m}}|^2\right) e^{-2\mathrm{Im}(\beta_{\boldsymbol{m}}(n_0 k))M} + 2\mathrm{i}\beta \mathrm{Re}(A^-_0) - 2\beta \mathrm{Im}(A^+_0 e^{-2\mathrm{i}\beta M}). \tag{A.3}$$

Taking the imaginary part of this expression and letting $M \to \infty$ we obtain the energy balance criterion

$$\sum_{\boldsymbol{m}\in U_0} \beta_{\boldsymbol{m}}(n_0 k) \left(|A^+_{\boldsymbol{m}}|^2 + |A^-_{\boldsymbol{m}}|^2\right) + 2\beta \mathrm{Re}(A^-_0) = 0, \tag{A.4}$$

where we have set $U_0 = \{\boldsymbol{m} \in \mathbb{Z}^{d_\Lambda} : n_0^2 k^2 - |\boldsymbol{\alpha_m}|^2 > 0\}$.

A.2 Scattering by impenetrable and transmissive gratings, $d_\Lambda = d - 1$.

In this case we assume first that the propagation domain $\Omega = \Omega_0 \cup \Omega_1$ and the common boundary between Ω_0 and Ω_1 is a periodic and connected surface; the impenetrable case (where the propagation domain Ω is formed by a unique domain of constant refractive index, the impenetrable region Ω^{imp} is non-empty and the boundary between these two is also a periodic and connected surface) can be easily

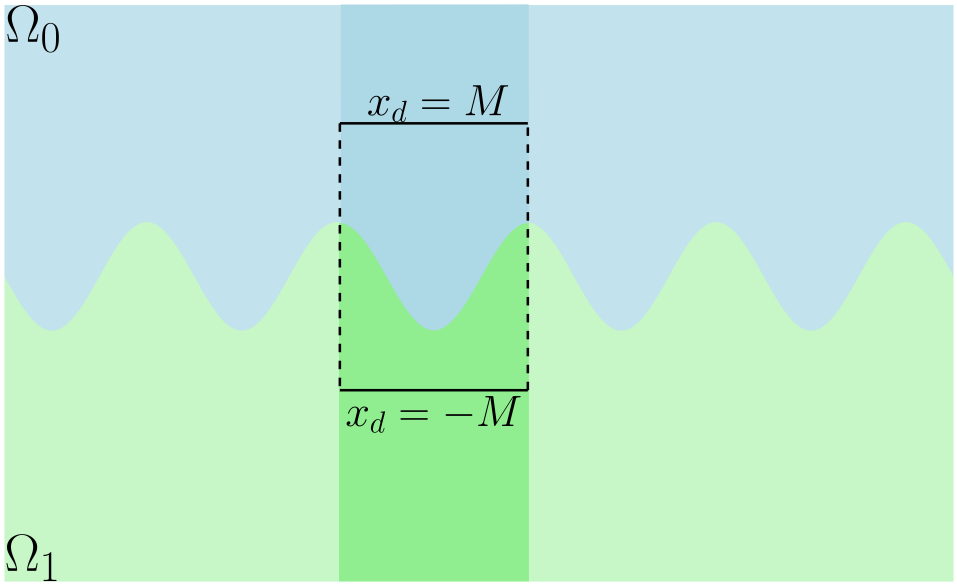

Figure A.2: Unit period of a transmission grating and integration domain Ω_M where Green's second identity is applied. The integrals along the parallel surfaces that joins the top and bottom flat boundaries cancel out due to the periodicity.

obtained from the transmission case (see Figure A.2). Given $M > 0$ and applying Green's second identity in the region Ω_M defined in the previous section we have

$$\int\limits_{\{x_d=M\}^\sharp} \left(\overline{u_0}\frac{\partial u_0}{\partial x_d} - u_0\frac{\partial \overline{u_0}}{\partial x_d}\right) dS = \int\limits_{\{x_d=-M\}^\sharp} \left(\overline{u_1}\frac{\partial u_1}{\partial x_d} - u_1\frac{\partial \overline{u_1}}{\partial x_d}\right) dS \tag{A.5}$$

(the boundary term along the common interface vanishes because of the transmission conditions (1.17)). A similar argument as the one provided in the previous section (using relations (1.12)–(1.13), expanding u_0 and u_1 in terms of their corresponding Rayleigh-series and using the orthogonality of $\mathrm{e}^{\mathrm{i}\boldsymbol{\alpha_m}\cdot\boldsymbol{x}}$, $\boldsymbol{m} \in \mathbb{Z}^{d_\Lambda}$ with respect to the standard L^2 inner-product) shows that

$$\sum_{\boldsymbol{m}\in U_0} \beta_{\boldsymbol{m}}(n_0 k)|A^+_{\boldsymbol{m}}|^2 + \sum_{\boldsymbol{m}\in U_1} \beta_{\boldsymbol{m}}(n_1 k)|A^-_{\boldsymbol{m}}|^2 = \beta, \tag{A.6}$$

where U_0 is given in the previous section and U_1 is defined similarly as $U_1 = \{\boldsymbol{m} \in \mathbb{Z}^{d_\Lambda} : n_1^2 k^2 - |\boldsymbol{\alpha_m}|^2 > 0\}$. The energy balance criterion for the impenetrable case can be obtained in a straightforward manner noting that for such configuration, the total field can be extended to the region Ω^{imp} by zero, which is trivially a solution of the Helmholtz equation; thus, the brief derivation above can also be applied in

this case and since all coefficients of the Rayleigh expansion A_n^- vanish we have

$$\sum_{\boldsymbol{m}\in U_0} \beta_{\boldsymbol{m}}(n_0 k)|A_{\boldsymbol{m}}^+|^2 = \beta. \tag{A.7}$$

A.3 Scattering by linear arrays in three-dimensional space, $d_\Lambda = 1$, $d = 3$

This section derives the energy balance criterion for periodic structures like the ones considered in Section 5.4 consisting of arrays of impenetrable particles or surfaces having periodicity along the x_1 axis (linear arrays). We assume that the infinite set of scatterers are contained inside the cylinder $\Omega_M = \{\boldsymbol{x} \in \mathbb{R}^3 : x_2^2 + x_3^2 < M^2\}$ for some $M > 0$. Letting $\rho > M$ and applying Green's second identity in a similar manner as in Sections A.1 and A.2 we have

$$0 = \int\limits_{\partial B(0,\rho)} \left(\overline{u}\frac{\partial u}{\partial \nu} - u\frac{\partial \overline{u}}{\partial \nu}\right) dS. \tag{A.8}$$

Writing $u = u^{\mathrm{s}} + u^{\mathrm{inc}}$ and replacing u^{s} by its corresponding Rayleigh expansion (1.29) it follows that

$$0 = \sum_{m\in\mathbb{Z}} \int\limits_{|\boldsymbol{x}^\perp|=\rho} \left(\overline{U_m}\frac{\partial U_m}{\partial \nu} - U_m\frac{\partial \overline{U_m}}{\partial \nu}\right) + 2\mathrm{i}\mathrm{Im}\left(\int\limits_{|\boldsymbol{x}^\perp|=\rho} \mathrm{e}^{\mathrm{i}\boldsymbol{\beta}\cdot\boldsymbol{x}^\perp}\frac{\partial U_0}{\partial \nu} - U_0\frac{\partial \mathrm{e}^{\mathrm{i}\boldsymbol{\beta}\cdot\boldsymbol{x}^\perp}}{\partial \nu}\right). \tag{A.9}$$

For those indexes m such that $\beta_m^2 = \kappa^2 - \alpha_m^2 > 0$, the functions U_m are solutions of the Helmholtz equation in two-dimensional space satisfying Sommerfeld's radiation condition and therefore each can be expanded in the form

$$U_m(x_2, x_3) = \sum_{\ell\in\mathbb{Z}} u_\ell^{(m)} H_n^{(1)}(\beta_m|\boldsymbol{x}^\perp|)\mathrm{e}^{\mathrm{i}n\theta}, \tag{A.10}$$

where $H_\ell^{(1)}$ is the Hankel's function of the first kind of order ℓ and θ is such that $x_2 = |\boldsymbol{x}^\perp|\cos\theta$ and $x_3 = |\boldsymbol{x}^\perp|\sin\theta$. A similar expression for the factor $\mathrm{e}^{\mathrm{i}\boldsymbol{\beta}\cdot\boldsymbol{x}^\perp}$ of the incoming wave can be obtained by means of the Jacobi-Anger's expansion [CK12]

$$\mathrm{e}^{\mathrm{i}\boldsymbol{\beta}\cdot\boldsymbol{x}^\perp} = \sum_{\ell\in\mathbb{Z}} \mathrm{i}^\ell \mathrm{e}^{-\mathrm{i}\ell\tilde{\theta}} J_\ell(|\boldsymbol{\beta}||\boldsymbol{x}^\perp|)\mathrm{e}^{\mathrm{i}\ell\theta}, \tag{A.11}$$

where $\tilde{\theta}$ is such that $\boldsymbol{\beta} = |\boldsymbol{\beta}|(\cos\tilde{\theta}, \sin\tilde{\theta})$ and J_ℓ is the Bessel's function of the first kind of order ℓ. Using the orthogonality of the exponentials $\mathrm{e}^{i\ell\theta}$ in $L^2(\partial B(0,\rho))$ and the relations for the Wronskians [DLM17, Eq. 10.5.1-5]

$$W(H_\ell^{(1)}, \overline{H_\ell^{(1)}})(z) = -\frac{4i}{\pi z}, \quad W(H_\ell^{(1)}, J_\ell)(z) = -\frac{2i}{\pi z},$$

we have

$$\int\limits_{|\boldsymbol{x}^{\perp}|=\rho} \left(\overline{U_m} \frac{\partial U_m}{\partial \nu} - U_m \frac{\partial \overline{U_m}}{\partial \nu} \right) = 8\mathrm{i} \sum_{\ell \in \mathbb{Z}} |u_n^{(m)}|^2 \tag{A.12}$$

and

$$\left(\int\limits_{|\boldsymbol{x}^{\perp}|=\rho} \mathrm{e}^{\mathrm{i}\boldsymbol{\beta}\cdot\boldsymbol{x}^{\perp}} \frac{\partial U_0}{\partial \nu} - U_0 \frac{\partial \mathrm{e}^{\mathrm{i}\boldsymbol{\beta}\cdot\boldsymbol{x}^{\perp}}}{\partial \nu} \right) = 4\mathrm{i} \sum_{\ell \in \mathbb{Z}} u_\ell^{(0)} \mathrm{i}^\ell \mathrm{e}^{\mathrm{i}\ell\tilde{\theta}}. \tag{A.13}$$

Note that these expressions are independent ρ. In contrast, for the indexes m such that $\beta_m^2 = \kappa^2 - \alpha_m^2 < 0$, U_m decays exponentially fast as $\rho \to \infty$ and therefore, taking that limit in (A.9), the corresponding integrals involving U_m in that equation will vanish out. Thus, we obtain the energy balance criterion for impenetrable periodic structures with $d_\Lambda = 1$ in three-dimensional space:

$$\sum_{m \in U} \left(\sum_{\ell \in \mathbb{Z}} |u_\ell^{(m)}|^2 \right) = -\mathrm{Im} \left(\sum_{\ell \in \mathbb{Z}} \mathrm{e}^{\mathrm{i}\ell(\tilde{\theta}-\pi/2)} u_\ell^{(0)} \right). \tag{A.14}$$

Appendix B

EWALD SUMMATION METHOD

All cases of Ewald's representation formula (2.27)– (2.30) are derived from the integral expression

$$G_\kappa(\boldsymbol{x}) = \frac{1}{2\pi^{d/2}} \int_C \mathrm{e}^{-|\boldsymbol{x}|t^2} \mathrm{e}^{\kappa^2/4t^2} t^{d-3} dt, \quad d = 2, 3 \tag{B.1}$$

of the corresponding free-space Green function $G_\kappa(\boldsymbol{x})$ (see Equation (2.2)), where C is a contour joining the origin and infinity and which verifies

$$|\arg t| < \frac{\pi}{4} \quad \text{as} \quad t \to \infty \quad \text{and} \quad \arg t \to -\frac{\pi}{4} \quad \text{as} \quad t \to 0.$$

Equation (B.1) is obtained by means of the following Lemma.

Lemma 1. *For $\nu \in \mathbb{R}$, $r > 0$ and $k \in \mathbb{C}$ with $0 < \arg(k) < \pi/2$ it holds*

$$H_\nu^{(1)}(kr) = \frac{2}{\mathrm{i}\pi} \mathrm{e}^{-\mathrm{i}\pi\nu} \left(\frac{k}{2r}\right)^\nu \int_C t^{-2\nu-1} \mathrm{e}^{-r^2t^2 + k^2/4t^2} dt. \tag{B.2}$$

Proof. Consider first the well-known representation of the Hankel function of the first kind of order ν [GR14, Eq.8.422]

$$H_\nu^{(1)}(z) = -\frac{\mathrm{i}}{\pi} \int_{-\infty}^{+\infty+\mathrm{i}\pi} \mathrm{e}^{z\sinh(w) - \nu w} dw, \quad |\arg z| < \frac{\pi}{2}, \tag{B.3}$$

where the path of integration is given by

$$\{-t : 0 < t\} \cup \{\mathrm{i}t : 0 < t < \pi\} \cup \{t : 0 < t\}.$$

Assuming $0 < \arg(z) < \pi/2$, applying Cauchy's theorem in the rectangle with vertices $-R$, 0, $\mathrm{i}\eta$ and $-R + \mathrm{i}\eta$ ($\eta = \pi/2 - \arg z$) to the integrand in (B.3) (a holomorphic function) and then taking the limit $R \to \infty$ it follows that the portion of the integral in (B.3) along the path $\{-t : 0 < t\} \cup \{\mathrm{i}t : 0 < t < \pi\}$ is equal to the integral with same integrand but along the infinite path $\{t + \mathrm{i}(\pi/2 - \arg z)\}$ (in this computation it is necessary to bound the integral along the vertical segment $-R + \mathrm{i}t$,

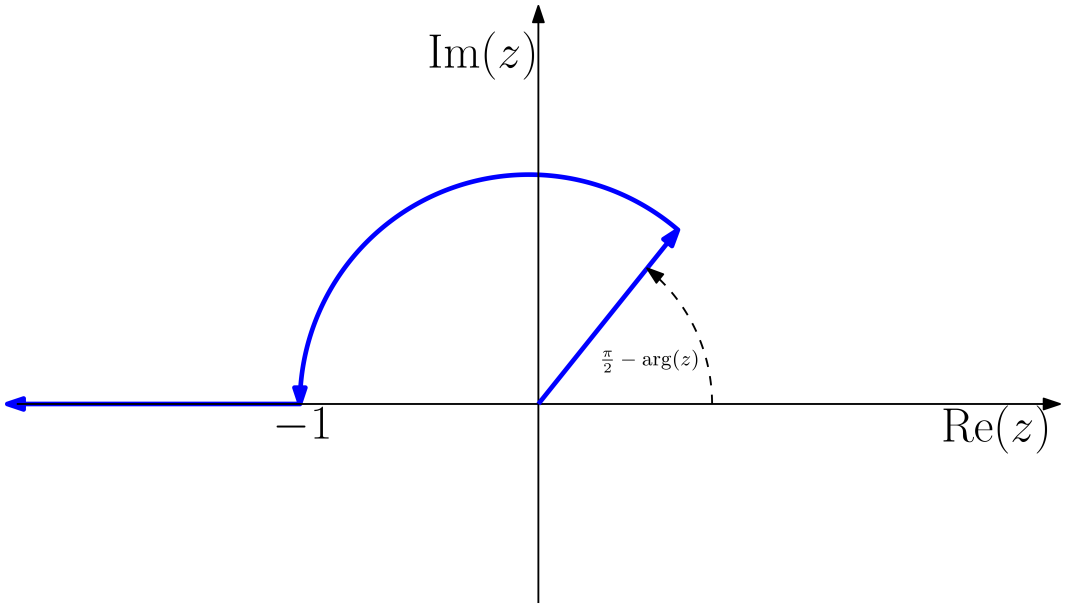

Figure B.1: Integration contour obtained after the change of variables $u = e^w$ in equation (B.5).

$0 < t < \eta$, though it can be easily checked that the integrand decays exponentially fast as $R \to +\infty$). Thus we can re-express $H_\nu^{(1)}(z)$ in the form

$$H_\nu^{(1)}(z) = -\frac{i}{\pi} \int_{-\infty+i(\frac{\pi}{2}-\arg z)}^{+\infty+i\pi} e^{z\sinh(w)-\nu w} dw \tag{B.4}$$

for $0 < \arg z < \pi/2$. Making the substitution $u = e^w$ it follows that

$$H_\nu^{(1)}(z) = -\frac{i}{\pi} \int_{\tilde{C}} u^{-\nu-1} e^{\frac{z}{2}(u-\frac{1}{u})} du, \tag{B.5}$$

where the transformed path $\tilde{C}$ is formed by the segment joining the origin with $e^{i(\pi/2-\arg(z))}$, then the arc of unit radius joining this latter point with -1 and then the infinite line $(-\infty, -1]$ (see Figure B.1). Thus,

$$H_\nu^{(1)}(kr) = -\frac{i}{\pi} \int_{\tilde{C}} u^{-\nu-1} e^{\frac{kr}{2}(u-\frac{1}{u})} du, \tag{B.6}$$

and a second substitution $u = -2rt^2/k$ yields

$$H_\nu^{(1)}(kr) = -\frac{2i}{\pi} e^{-i\pi\nu} \left(\frac{k}{2r}\right)^\nu \int_C t^{-2\nu-1} e^{-r^2t^2+k^2/4t^2} dt, \tag{B.7}$$

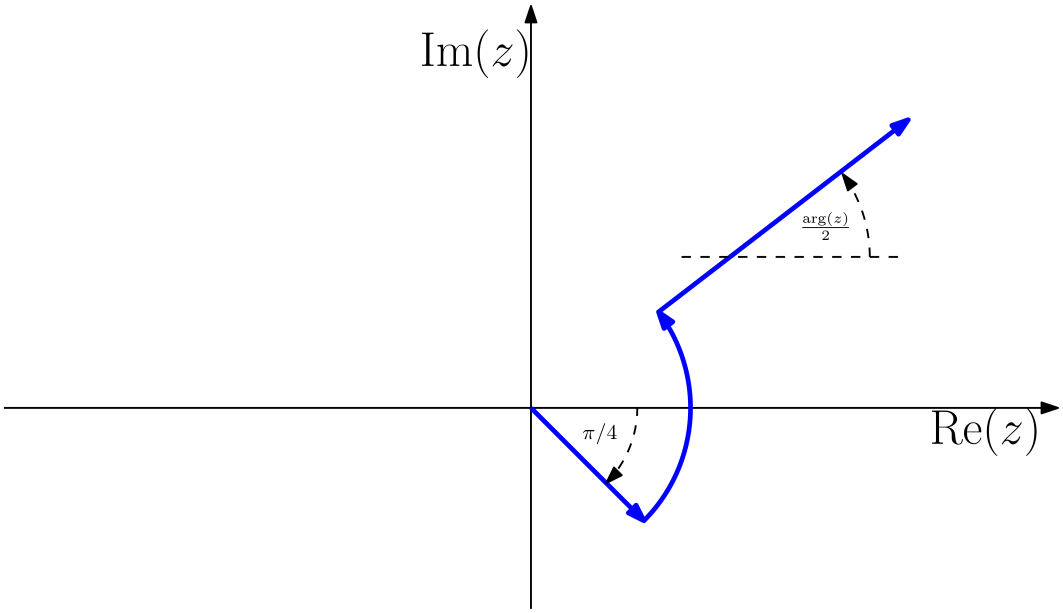

Figure B.2: Integration contour obtained after the change of variables $u = -2rt^2/k$ in equation (B.7).

where the path of integration C is a segment that starts at the origin with direction $e^{-i\pi/4}$, an arc of a circle and then a line that extends to infinity parallel to $e^{i \arg z/2}$ (see Figure B.2). □

Remark 5. *The path of integration in* (B.2) *can be deformed as long as the new contour starts at the origin in the same direction* $e^{-i\pi/4}$ *and the integration variable* t *approaches infinity satisfying* $|\arg(t)| < \pi/4$ *(if this latter condition is satisfied we have* $\mathrm{Re}(t^2) > 0$ *and so the exponential in* (B.2) *decays exponentially fast as* $|t| \to 0$*).*

In the case $d = 2$, the integral representation for the free-space Green function (B.1) is obtained from (B.2) by substitution. For $d = 3$, in turn, we get (B.1) from the relation

$$\frac{1}{4\pi}\frac{e^{ikr}}{r} = \frac{1}{4\sqrt{2\pi}}\sqrt{\frac{k}{r}}H^{(1)}_{-1/2}(kr)$$

together with (B.2) (setting $\nu = -1/2$ in the latter formula).

For simplicity, in what follows we will interchange deliberately infinite summations with integrals over infinite regions without justifying the procedure at each step. A rigorous derivation of Ewald's representation formula would require adding a small imaginary part ε to the real wavenumber $\kappa > 0$ in order that all intervening

infinite sums converge absolutely and uniformly (so that the summation and integral symbols can be interchanged safely) and then, finally, taking the limit $\varepsilon \to 0$ in the resulting expressions.

Letting $\eta > 0$ denote an arbitrary *splitting* parameter, we consider in (B.1) a path $C = C_1 \cup C_2$ where C_1 equals the infinite line $[\eta, \infty)$ while C_2 is a curve contained in the complex plane that starts at the origin in the direction $\mathrm{e}^{-\mathrm{i}\pi/4}$ and ends at the point η. The decomposition (2.25) results from representing each free-space Green function in (2.1) using formula (B.1) and splitting the integral along the contour C into two integrals along C_1 and C_2. The first of the resulting expressions is the infinite sum

$$G^q_\Lambda(\boldsymbol{x}) = \sum_{\boldsymbol{R_m}\in\Lambda} \mathrm{e}^{\mathrm{i}\boldsymbol{\alpha}\cdot\boldsymbol{R_m}} \frac{1}{\pi^{d/2}} \int_\eta^\infty e^{-|\boldsymbol{x}-\boldsymbol{R_m}|^2t^2} \mathrm{e}^{\kappa^2/4t^2} t^{d-3} dt \tag{B.8}$$

which equals (2.27) when $d = 2$ and (2.28) when $d = 3$; these two equations can be obtained by setting $\rho_{\boldsymbol{m}} = |\boldsymbol{x} - \boldsymbol{R_m}|$, and using the relations

$$\begin{aligned} \int_\eta^\infty \mathrm{e}^{-|\boldsymbol{x}-\boldsymbol{R_m}|^2t^2} e^{\kappa^2/4t^2} \frac{1}{t} dt &= \frac{1}{2} \sum_{j=0}^\infty \frac{1}{j!} \left(\frac{k}{2}\right)^{2j} \int_{\eta^2}^\infty \frac{\mathrm{e}^{-\rho_n^2 u}}{u^{j+1}} du \\ &= \frac{1}{2} \sum_{j=0}^\infty \frac{1}{j!} \left(\frac{k}{2}\right)^{2j} E_{j+1}(\eta^2\rho_{\boldsymbol{m}}^2) \end{aligned} \tag{B.9}$$

and

$$\int \mathrm{e}^{-a^2t^2+b^2/t^2} dt = -\frac{\sqrt{\pi}}{4a} \mathrm{e}^{-a^2t^2+b^2/t^2} \left[w\left(\frac{b}{t} + \mathrm{i}at\right) + w\left(-\frac{b}{t} + \mathrm{i}at\right)\right] + \text{const}, \quad a \neq 0. \tag{B.10}$$

In (B.9), E_j denotes the exponential integral defined in (2.26) while in (B.10), w is the Faadeeva function given by

$$w(z) = e^{-z^2} \mathrm{erfc}(-\mathrm{i}z), \, z \in \mathbb{C} \tag{B.11}$$

and where erfc denotes the analytic continuation of the complementary error function.

To obtain the corresponding expressions for $G^q_{\Lambda^*}$ in (2.25), we use the decomposition $\boldsymbol{x} = \boldsymbol{x}^{\parallel} + \boldsymbol{x}^{\perp}$ (see Remark 1) and note that the d_Λ-dimensional Fourier transform (which we denote by $\mathcal{F}_{d_\Lambda}$) of the function

$$f(\boldsymbol{x}^{\parallel}) = \int_{C_1} \mathrm{e}^{-|\boldsymbol{x}^{\parallel}|^2t^2} \mathrm{e}^{-|\boldsymbol{x}^{\perp}|^2t^2} \mathrm{e}^{\kappa^2/4t^2} t^{d-3} dt \tag{B.12}$$

equals

$$\mathcal{F}_{d_\Lambda}(f)(\boldsymbol{\xi}) = \pi^{d_\Lambda/2} \int_{C_1} \mathrm{e}^{-|\boldsymbol{x}^\perp|^2 t^2} \mathrm{e}^{(\kappa^2-|\boldsymbol{\xi}|^2)/4t^2} \frac{1}{t^{3-(d-d_\Lambda)}} dt. \tag{B.13}$$

Thus, if $d - d_\Lambda = 1$, we can use (B.10) together with the change of variables $t = 1/s$ and obtain

$$\begin{aligned}\mathcal{F}_{d_\Lambda}(f)(\boldsymbol{\xi}) = \mathrm{i}\frac{\pi^{(d_\Lambda+1)/2}}{2\sqrt{\kappa^2-|\boldsymbol{\xi}|^2}} \mathrm{e}^{-|\boldsymbol{x}^\perp|^2\eta^2} \mathrm{e}^{(\kappa^2-|\boldsymbol{\xi}|^2)/4\eta^2} \\ \left[w\left(-|\boldsymbol{x}^\perp|\eta + \mathrm{i}\frac{\sqrt{\kappa^2-|\boldsymbol{\xi}|^2}}{2\eta}\right) + w\left(-|\boldsymbol{x}^\perp|\eta - \mathrm{i}\frac{\sqrt{\kappa^2-|\boldsymbol{\xi}|^2}}{2\eta}\right)\right].\end{aligned} \tag{B.14}$$

If $d = 3$ and $d_\Lambda = 1$, in turn, performing the change of variables $t = 1/s^2$ we have

$$\mathcal{F}_{d_\Lambda}(f)(\xi) = \pi^{1/2} \int_{1/\eta^2}^{\infty(\mathrm{e}^{\mathrm{i}\pi/8})} \mathrm{e}^{-|\boldsymbol{x}^\perp|^2/s} \mathrm{e}^{s(\kappa^2-\xi^2)/4} \frac{1}{s} ds, \tag{B.15}$$

where the upper limit $\infty(\mathrm{e}^{\mathrm{i}\pi/8})$ indicates that infinity is approached along the direction $\mathrm{e}^{\mathrm{i}\pi/8}$. Expanding $\mathrm{e}^{-|\boldsymbol{x}^\perp|^2/s}$ by a Laurent series (with respect to s) we have

$$\mathcal{F}_{d_\Lambda}(f)(\xi) = \pi^{1/2} \sum_{j=0}^{\infty} \frac{(-1)^j}{j!} |\boldsymbol{x}^\perp|^{2j} \int_{1/\eta^2}^{\infty(\mathrm{e}^{\mathrm{i}\pi/8})} \mathrm{e}^{s(\kappa^2-\xi^2)/4} \frac{1}{s^{j+1}} ds \tag{B.16}$$

and noting that

$$\int_{1/\eta^2}^{\infty(\mathrm{e}^{\mathrm{i}\pi/8})} \mathrm{e}^{s(\kappa^2-\xi^2)/4} \frac{1}{s^{j+1}} ds = \eta^{2j} E_{j+1}\left(-\frac{\kappa^2-|\xi|^2}{4\eta^2}\right) \tag{B.17}$$

we get

$$\mathcal{F}_{d_\Lambda}(f)(\xi) = \pi^{1/2} \sum_{j=0}^{\infty} \frac{(-1)^j}{j!} |\boldsymbol{\eta}\boldsymbol{x}^\perp|^{2j} E_{j+1}\left(-\frac{\kappa^2-|\xi|^2}{4\eta^2}\right). \tag{B.18}$$

Equations (2.29) and (2.30) are obtained applying the Poisson summation formula to

$$G^q_{\Lambda^*}(\boldsymbol{x}) = \sum_{\boldsymbol{R_m}\in\Lambda} \mathrm{e}^{\mathrm{i}\alpha\cdot\boldsymbol{R_m}} \frac{1}{\pi^{d/2}} \int_{C_2} \mathrm{e}^{-|\boldsymbol{x}-\boldsymbol{R_m}|^2 t^2} \mathrm{e}^{\kappa^2/4t^2} t^{d-3} dt$$

with the corresponding computed Fourier transforms (B.14) and (B.18).

REFERENCES

[AQ11] Sanjar M Abrarov and Brendan M Quine. "Efficient algorithmic implementation of the Voigt/complex error function based on exponential series approximation". In: *Applied Mathematics and Computation* 218.5 (2011), pp. 1894–1902.

[Air38] George Airy. "On the Intensity of Light in the neighbourhood of a Caustic". In: *Transactions of the Cambridge Philosophical Society* 6 (1838).

[A+17] Eldar Akhmetgaliyev, Oscar P Bruno, et al. "Regularized integral formulation of mixed Dirichlet-Neumann problems". In: *Journal of Integral Equations and Applications* 29.4 (2017), pp. 493–529.

[Amp26] André-Marie Ampère. *Théorie des phénomènes électro-dynamiques, uniquement déduite de l'expérience*. Méquignon-Marvis, 1826.

[Ara19] François Arago. "Rapport fait par M". In: *Arago à l'Académie des Sciences, au nom de la Commission qui avait été chargée d'examiner les mémoires envoyés au concours pour le prix de la diffraction. Annales de Chimie et de Physique, XI* (1819), pp. 1866–70.

[Are+13] Tilo Arens et al. "Analysing Ewald's method for the evaluation of Green's functions for periodic media". In: *IMA Journal of Applied Mathematics* 78.3 (2013), pp. 405–431.

[Bat54] Harry Bateman. "Tables of integral transforms". In: (1954).

[Blo29] F. Bloch. "Über die Quantenmechanik der Elektronen in Kristallgittern". In: *Zeitschrift fur Physik* 52 (July 1929), pp. 555–600. DOI: 10.1007/BF01339455.

[BJ38] Robert Boyle and John Jones. *Philosophical works*. Innys, 1738.

[Bra09] KARL Ferdinand Braun. "Electrical oscillations and wireless telegraphy". In: *Nobel Lecture, December* 11.1909 (1909), pp. 226–245.

[BD14] Oscar P Bruno and Berangere Delourme. "Rapidly convergent two-dimensional quasi-periodic Green function throughout the spectrum–including Wood anomalies". In: *Journal of Computational Physics* 262 (2014), pp. 262–290.

[BF17] Oscar P Bruno and Agustin G Fernandez-Lado. "Rapidly convergent quasi-periodic Green functions for scattering by arrays of cylinders—including Wood anomalies". In: *Proc. R. Soc. A* 473.2199 (2017), p. 20160802. DOI: 10.1098/rspa.2016.0802. URL: https://doi.org/10.1098/rspa.2016.0802.

[BG18] Oscar P Bruno and Emmanuel Garza. "A Chebyshev-based rectangular-polar integral solver for scattering by general geometries described by non-overlapping patches". In: *arXiv preprint arXiv:1807.01813* (2018).

[BH09] Oscar P Bruno and Michael C Haslam. "Efficient high-order evaluation of scattering by periodic surfaces: deep gratings, high frequencies, and glancing incidences". In: *JOSA A* 26.3 (2009), pp. 658–668.

[BH10] Oscar P Bruno and Michael C Haslam. "Efficient high-order evaluation of scattering by periodic surfaces: vector-parametric gratings and geometric singularities". In: *Waves in Random and Complex Media* 20.4 (2010), pp. 530–550.

[BM18a] Oscar P Bruno and Martin Maas. "Shifted equivalent sources and FFT acceleration for periodic scattering problems, including Wood anomalies". In: *Journal of Computational Physics* (2018).

[Bru+16] Oscar P Bruno et al. "Superalgebraically convergent smoothly windowed lattice sums for doubly periodic Green functions in three-dimensional space". In: *Proc. R. Soc. A* 472.2191 (2016), p. 20160255.

[Bru+17] Oscar P Bruno et al. "Three-dimensional quasi-periodic shifted Green function throughout the spectrum, including Wood anomalies". In: *Proc. R. Soc. A* 473.2207 (2017), p. 20170242.

[BM18b] Evgeny N Bulgakov and Dmitrii N Maksimov. "Optical response induced by bound states in the continuum in arrays of dielectric spheres". In: *JOSA B* 35.10 (2018), pp. 2443–2452.

[CWJ07] F. Capolino, D.R. Wilton, and W.A. Johnson. "Efficient computation of the 3D Green's function for the Helmholtz operator for a linear array of point sources using the Ewald method". In: *Journal of Computational Physics* 223.1 (2007), pp. 250–261. ISSN: 0021-9991. DOI: http://dx.doi.org/10.1016/j.jcp.2006.09.013. URL: http://www.sciencedirect.com/science/article/pii/S0021999106004359.

[Chi+12] Hank Childs et al. "VisIt: An End-User Tool For Visualizing and Analyzing Very Large Data". In: *High Performance Visualization–Enabling Extreme-Scale Scientific Insight*. Oct. 2012, pp. 357–372.

[Cho18] Min Hyung Cho. "Spectrally-accurate numerical method for acoustic scattering from doubly-periodic 3D multilayered media". In: *arXiv preprint arXiv:1806.03813* (2018).

[Cod93] William J Cody. "Algorithm 715: SPECFUN–a portable FORTRAN package of special function routines and test drivers". In: *ACM Transactions on Mathematical Software (TOMS)* 19.1 (1993), pp. 22–30.

[CK13] David Colton and Rainer Kress. *Integral equation methods in scattering theory*. Vol. 72. SIAM, 2013.

[CK12] David Colton and Rainer Kress. *Inverse acoustic and electromagnetic scattering theory*. Vol. 93. Springer Science & Business Media, 2012.

[Dar+18] Ahmad Darweesh et al. "The role of Rayleigh-Wood anomalies and surface plasmons in optical enhancement for nano-gratings". In: *Nanomaterials* 8.10 (2018), p. 809.

[Den+17a] Ryan Denlinger et al. "A fast summation method for oscillatory lattice sums". In: *Journal of Mathematical Physics* 58.2 (2017), p. 023511.

[Den+17b] Ryan Denlinger et al. "A fast summation method for oscillatory lattice sums". In: *Journal of Mathematical Physics* 58.2 (2017), p. 023511.

[DLM17] NIST DLMF. "Digital Library of Mathematical Functions". In: *WJ Olver, AB Olde Daalhuis, DW Lozier, BI Schneider, RF Boisvert, CW Clark, BR Miller and BV Saunders, eds* (2017).

[EK87] Sylvan Elhay and Jaroslav Kautsky. "Algorithm 655: IQPACK: FORTRAN subroutines for the weights of interpolatory quadratures". In: *ACM Transactions on Mathematical Software (TOMS)* 13.4 (1987), pp. 399–415.

[Erd+54] Arthur Erdelyi et al. *Tables of Integral Transforms: Vol.: 2*. McGraw-Hill Book Company, Incorporated, 1954.

[Ewa21] Paul P Ewald. "Die Berechnung optischer und elektrostatischer Gitterpotentiale". In: *Annalen der physik* 369.3 (1921), pp. 253–287.

[Fan41] Ugo Fano. "The theory of anomalous diffraction gratings and of quasi-stationary waves on metallic surfaces (Sommerfeld's waves)". In: *JOSA* 31.3 (1941), pp. 213–222.

[Far39] Michael Faraday. "Experimental researches in electricity (3 volumes)". In: *London: Richard and John Edward Taylor* (1839), pp. 122–124.

[FB50] A Fizeau and Louis Breguet. "Sur l'experience relative à la vitesse comparative de la lumière dans l'air et dans l'eau". In: *Compte Rendue des Séances de l'Académie des Sciences (Paris)* 30 (1850), pp. 771–774.

[Fou50] Léon Foucault. "Méthode générale pour mesurer la vitesse de la lumière dans l'air et les milieux transparents. Vitesses relatives de la lumière dans l'air et dans l'eau. Projet d'expérience sur la vitesse de propagation du calorique rayonnant". In: *Compte Rendue des Séances de l'Académie des Sciences (Paris)* 30 (1850), pp. 551–560.

[FG53] Rosalind E Franklin and Raymond G Gosling. "Molecular configuration in sodium thymonucleate". In: *Nature* 171.4356 (1953), p. 740.

[Fra24] Joseph von Fraunhofer. *Neue Modificationen des Lichtes durch gegenseitige Einwirkung und Beugung der Strahlen, und Gesetze derselben*. Vol. 2. 1824.

[Fra+97] Valérie Frayssé et al. "A set of GMRES routines for real and complex arithmetics". In: *Tech. Rep. TR/PA/97/49, CERFACS, France* (1997).

[Fre68] Augustin Fresnel. *Oeuvres complètes d'augustin Fresnel*. Imprimerie impériale, 1868.

[FKL13] Walter Friedrich, Paul Knipping, and Max Laue. "Interferenzerscheinungen bei roentgenstrahlen". In: *Annalen der Physik* 346.10 (1913), pp. 971–988.

[GV96] Gene H. Golub and Charles F. Van Loan. *Matrix Computations (3rd Ed.)* Baltimore, MD, USA: Johns Hopkins University Press, 1996. ISBN: 0-8018-5414-8.

[GR14] Izrail Solomonovich Gradshteyn and Iosif Moiseevich Ryzhik. *Table of integrals, series, and products*. Academic press, 2014.

[Gre38] G. Green. "On the Reflection and Refraction of Sound". In: *Transactions of the Cambridge Philosophical Society* 6 (1838), p. 403.

[Gri65] Francesco Maria Grimaldi. "Physico-mathesis de lumine, coloribus, et iride". In: *Reviewed in Philosophical Transactions of the Royal Society of London* (1665).

[Har49] George R. Harrison. "The Production of Diffraction GratingsI. Development of the Ruling Art∗". In: *J. Opt. Soc. Am.* 39.6 (June 1949), pp. 413–426. DOI: 10.1364/JOSA.39.000413. URL: http://www.osapublishing.org/abstract.cfm?URI=josa-39-6-413.

[Her88] H. Hertz. "Ueber die Ausbreitungsgeschwindigkeit der electrodynamischen Wirkungen". In: *Annalen der Physik* 270.7 (1888), pp. 551–569.

[Hoo65] Robert Hooke. *Micrographia, or, Some physiological descriptions of minute bodies made by magnifying glasses: With observations and inquiries thereupon*. J. Martyn and J. Allestry., 1665.

[Huy90] Christian Huygens. *Traité de la lumière*. Pieter van der Aa, 1690.

[Kim+15] Kyoung-Youm Kim et al. "Slow-light effect via Rayleigh anomaly and the effect of finite gratings". In: *Optics letters* 40.22 (2015), pp. 5339–5342.

[Kir83] Gustav Kirchhoff. "Zur theorie der lichtstrahlen". In: *Annalen der Physik* 254.4 (1883), pp. 663–695.

[Kod11] Masao Kodama. "Algorithm 912: a module for calculating cylindrical functions of complex order and complex argument". In: *ACM Transactions on Mathematical Software (TOMS)* 37.4 (2011), p. 47.

[KW93] Rudolf Kohlrausch and Wilhelm Weber. “Elektrodynamische Maassbestimmungen insbesondere Zurückführung der Stromintensitäts-Messungen auf mechanisches Maass”. In: (1893), pp. 609–669.

[Kre14] Rainer Kress. *Linear integral equations*. Vol. 82. Springer, 2014.

[KNR11] Harun Kurkcu, Nilima Nigam, and Fernando Reitich. “An integral representation of the Green function for a linear array of acoustic point sources”. In: *Journal of Computational Physics* 230.8 (2011), pp. 2838–2856.

[KR09] Harun Kurkcu and Fernando Reitich. “Stable and efficient evaluation of periodized Green’s functions for the Helmholtz equation at high frequencies”. In: *Journal of Computational Physics* 228.1 (2009), pp. 75–95.

[KM00] A. Kustepeli and A. Q. Martin. “On the splitting parameter in the Ewald method”. In: *IEEE Microwave and Guided Wave Letters* 10.5 (May 2000), pp. 168–170. ISSN: 1051-8207. DOI: 10.1109/75.850366.

[LKB15] Jun Lai, Motoki Kobayashi, and Alex Barnett. “A fast and robust solver for the scattering from a layered periodic structure containing multi-particle inclusions”. In: *Journal of Computational Physics* 298 (2015), pp. 194–208.

[Lin10] Chris M Linton. “Lattice sums for the Helmholtz equation”. In: *SIAM review* 52.4 (2010), pp. 630–674.

[Lin98] C.M. Linton. “The Green’s Function for the Two-Dimensional Helmholtz Equation in Periodic Domains”. In: *Journal of Engineering Mathematics* 33.4 (May 1998), pp. 377–401. DOI: 10.1023/A:1004377501747. URL: https://doi.org/10.1023/A:1004377501747.

[LZT13] CM Linton, V Zalipaev, and Ian Thompson. “Electromagnetic guided waves on linear arrays of spheres”. In: *Wave Motion* 50.1 (2013), pp. 29–40.

[LB16] Yuxiang Liu and Alex H Barnett. “Efficient numerical solution of acoustic scattering from doubly-periodic arrays of axisymmetric objects”. In: *Journal of Computational Physics* 324 (2016), pp. 226–245.

[LBA08] Giampiero Lovat, Paolo Burghignoli, and Rodolfo Araneo. “Efficient evaluation of the 3-D periodic Green’s function through the Ewald method”. In: *IEEE Transactions on Microwave Theory and Techniques* 56.9 (2008), pp. 2069–2075.

[Mar+16] AA Maradudin et al. “Rayleigh and Wood anomalies in the diffraction of light from a perfectly conducting reflection grating”. In: *Journal of Optics* 18.2 (2016), p. 024004.

[MS16] Alexei A Maradudin and Ingve Simonsen. "Rayleigh and Wood anomalies in the diffraction of acoustic waves from the periodically corrugated surface of an elastic medium". In: *Low Temperature Physics* 42.5 (2016), pp. 354–360.

[Mar09] Guglielmo Marconi. "Wireless telegraphic communication". In: *Nobel Lecture* 11 (1909), pp. 198–222.

[Mau+14] Agnès Maurel et al. "Wood's anomalies for arrays of dielectric scatterers". In: *Journal of the European Optical Society-Rapid publications* 9 (2014).

[Max81] James Clerk Maxwell. *A treatise on electricity and magnetism*. Vol. 1. Clarendon press, 1881.

[May12] Daniel Maystre. "Theory of Wood's anomalies". In: *Plasmonics*. Springer, 2012, pp. 39–83.

[MM00] William McLean and William Charles Hector McLean. *Strongly elliptic systems and boundary integral equations*. Cambridge university press, 2000.

[Mon08] John Anderson Monro. "A super-algebraically convergent, windowing-based approach to the evaluation of scattering from periodic rough surfaces". PhD thesis. California Institute of Technology, 2008.

[Neu38] Franz Neumann. "Theoretische Untersuchung der Gesetze, nach welchen das Licht and der Grenze zweier vollkommen durchsichtigen Medien reflectirt und gebrochen wird". In: *Abhandlungen der Königlichen Akademie der Wissenschaften zu Berlin* (1838).

[New72] Isaac Newton. "New theory of light and colors". In: *Philosophical Transactions* 6.80 (1672).

[NPT18] David Nicholls, Carlos Pérez-Arancibia, and Catalin Turc. "Sweeping preconditioners for the iterative solution of quasiperiodic Helmholtz transmission problems in layered media". In: *arXiv preprint arXiv:1809.05634* (2018).

[ND57] BRA Nijboer and FW De Wette. "On the calculation of lattice sums". In: *Physica* 23.1-5 (1957), pp. 309–321.

[Nor+15] Sven Nordebo et al. "On the natural modes of helical structures". In: *arXiv preprint arXiv:1502.00496* (2015).

[Per+18] Carlos Perez-Arancibia et al. "Domain decomposition for quasi-periodic scattering by layered media via robust boundary-integral equations at all frequencies". In: *arXiv preprint arXiv:1801.09094* (2018).

[PC90] R. Petit and M. Cadilhac. "Electromagnetic theory of gratings: some advances and some comments on the use of the operator formalism". In: *J. Opt. Soc. Am. A* 7.9 (Sept. 1990), pp. 1666–1674. DOI: 10.1364/JOSAA.7.001666. URL: http://josaa.osa.org/abstract.cfm?URI=josaa-7-9-1666.

[Pre+07] William H Press et al. *Numerical recipes 3rd edition: The art of scientific computing*. Cambridge university press, 2007.

[Ray96] John William Strutt Baron Rayleigh. *The theory of sound*. Vol. 2. Macmillan, 1896.

[Ray93] L Rayleigh. "Note on the remarkable case of diffraction spectra described by Prof. Wood (from Philosophical Magazine 1907)". In: *SPIE MILESTONE SERIES MS* 83 (1993), pp. 291–291.

[Ray07] Lord Rayleigh. "XXX. On the light dispersed from fine lines ruled upon reflecting surfaces or transmitted by very narrow slits". In: *The London, Edinburgh, and Dublin Philosophical Magazine and Journal of Science* 14.81 (1907), pp. 350–359.

[Rit86] D. Rittenhouse. "Explanation of an Optical Deception". In: *Transactions of the American Philosophical Society* 2 (1786), pp. 37–42. ISSN: 00659746. URL: http://www.jstor.org/stable/1005164.

[Sav+13] Silvio Savoia et al. "Surface sensitivity of Rayleigh anomalies in metallic nanogratings". In: *Optics express* 21.20 (2013), pp. 23531–23542.

[Sim15] Barry Simon. *A comprehensive course in analysis*. American Mathematical Society Providence, Rhode Island, 2015.

[Som09] Arnold Sommerfeld. "Über die Ausbreitung der Wellen in der drahtlosen Telegraphie". In: *Annalen der Physik* 333.4 (1909), pp. 665–736.

[SM07] Ivica Stevanoviæ and Juan R Mosig. "Periodic Green's function for skewed 3-D lattices using the Ewald transformation". In: *Microwave and Optical Technology Letters* 49.6 (2007), pp. 1353–1357.

[Ste+06] Ivica Stevanovic et al. "Integral-equation analysis of 3-D metallic objects arranged in 2-D lattices using the Ewald transformation". In: *IEEE Transactions on Microwave Theory and Techniques* 54.10 (2006), pp. 3688–3697.

[Sto49] George Gabriel Stokes. "On the dynamical theory of diffraction". In: *Transactions of the Cambridge Philosophical Society* 9 (1849), pp. 1–48.

[TJE19] Mehdi Tavakoli, Yousef Seyed Jalili, and Seyed Mohammad Elahi. "Rayleigh-Wood anomaly approximation with FDTD simulation of plasmonic gold nanohole array for determination of optimum extraordinary optical transmission characteristics". In: *Superlattices and Microstructures* 130 (2019), pp. 454–471.

[TL10] Ian Thompson and Chris M Linton. "Guided surface waves on one- and two-dimensional arrays of spheres". In: *SIAM Journal on Applied Mathematics* 70.8 (2010), pp. 2975–2995.

[Vey+91] Murat E Veysoglu et al. "Polarimetric passive remote sensing of periodic surfaces". In: *Journal of Electromagnetic Waves and Applications* 5.3 (1991), pp. 267–280.

[Wei94] J Andre C Weideman. "Computation of the complex error function". In: *SIAM Journal on Numerical Analysis* 31.5 (1994), pp. 1497–1518.

[Wil+09] Joshua L Wilson et al. "Analysis of rapidly twisted hollow waveguides". In: *IEEE Transactions on Microwave Theory and Techniques* 57.1 (2009), p. 130.

[Woo02] Robert Williams Wood. "On a remarkable case of uneven distribution of light in a diffraction grating spectrum". In: *Proceedings of the Physical Society of London* 18.1 (1902), p. 269.

[You02] Thomas Young. "II. The Bakerian Lecture. On the theory of light and colours". In: *Philosophical transactions of the Royal Society of London* 92 (1802), pp. 12–48.

[ZA11] Mofreh R Zaghloul and Ahmed N Ali. "Algorithm 916: computing the Faddeyeva and Voigt functions". In: *ACM Transactions on Mathematical Software (TOMS)* 38.2 (2011), p. 15.